USING PICOSECOND HEAT PULSES TO MEASURE MAGNETIZATION

A Dissertation

Presented to the Faculty of the Graduate School

of Cornell University

in Partial Fulfillment of the Requirements for the Degree of

Doctor of Philosophy

by

Darryl Harlan Ngai

February 2016

USING PICOSECOND HEAT PULSES TO MEASURE MAGNETIZATION

Darryl Harlan Ngai, Ph.D.

Cornell University 2016

Recent advances in nanoscale magnetism have demonstrated the potential for spin-based technology. Future engineering advances and new scientific discoveries will require research tools capable of examining local magnetization dynamics at length and time scales fundamental to magnetic systems, which is typically 10-200 nm and 5-50 ps. A key problem is that current table-top magnetic microscopy cannot access both of these scales simultaneously. In this thesis, we introduce a spatiotemporal magnetic microscopy technique which uses magneto-thermoelectric interactions to measure local magnetization via the time-resolved anomalous Nernst effect (TRANE). By generating a short-lived, local temperature gradient, the magnetic moment is transduced into an electrical signal. Experimentally, we show that TRANE microscopy has time resolution below 30 ps and spatial resolution limited by the thermal excitation area. Furthermore, we present numerical simulations to show that the thermal spot size sets the limits of the spatial resolution down to 50 nm. The thermal effects used for TRANE microscopy have no fundamental limit on their spatial resolution, therefore a future TRANE microscope employing a scanning plasmon antenna could enable measurements of nanoscale magnetic dynamics.

BIOGRAPHICAL SKETCH

Darryl Harlan Ngai was born on September 2, 1986 in Toronto, Canada to parents, Ming and Dorcas Ngai. At an early age, Darryl showed great interest in science and engineering. He recalls fond times as a child playing with science sets with his father and reading science books with his mother. Darryl went to elementary school at Charlton Public School. At early age, Darryl's parents put high emphasis on his education, especially encouraging him to learn math concepts outside of his standard school work. Darryl went to high school at Vaughan Secondary School. His high school chemistry teacher Staveros Naxakis saw that Darryl had a talent for science and encouraged him to enter many science competitions. Using these science competitions, Staveros was able to build Darryl's confidence and sparked his interest to pursue a career in science research.

For his undergraduate studies, Darryl enrolled at the University of Toronto in the program of Engineering Science. The program exposed him to many areas of science and engineering which has greatly helped his growth as a scientist. This was reflected in his various research projects as an undergrad, where his projects have included pulp and paper research with Ramin Farnood, statistical physics with Rashmi Desai and chemical physics with Gregory Scholes. Darryl was inspired to focus his studies in physics after taking a physics class with Allan Griffin and a summer research project with Rashmi Desai. In his fourth year at the University of Toronto, Darryl was introduced to the sport of Olympic weightlifting, which has become both a hobby and a form of mental therapy. The coaching of Hami Kanama and Tom Dilliplane has taught him to approach not only lifting but all aspects of life in a calm and controlled manner.

Darryl went to Cornell University to pursue his graduate studies in physics. Early in his graduate career, Darryl worked with Eun-Ah Kim studying theoretical condensed matter physics. His research was focused on one-dimensional correlated electron systems, with applications to carbon nanotubes. After his forth year, Darryl decided to work with Gregory Fuchs in the field of experimental condensed matter physics. With the Fuchs group, his research has been focused on developing a new technique for magnetic microscopy. The diverse research background at Cornell has allowed him to develop a unique perspective on physics.

After Cornell, Darryl will move to Maryland to launch a start-up company Z-senz with his good friend Christopher Brown. At Z-senz, they look to commercialize a small sized, high performance LIDAR system.

Dedicated to my family and friends.

ACKNOWLEDGEMENTS

I would like to begin by thanking Gregory Fuchs. Greg accepted me into his research group midway through my PhD career at Cornell, and from my first day joining the group he made me feel well accepted. He created an atmosphere in the research group that was very open and fostered great research along with great friendships. He is always excited to discuss research ideas and work alongside to fix problems in the laboratory. Most of all, he has greatly influenced my approach to experimental work.

I would like to thank Eun-Ah Kim for supervising me first four years at Cornell. I have learned much from her teachings, but most of all, she helped to develop my attention to details in my approaching physics. I would also like to thank Dan Ralph for being on my committee. He is always insightful and always available for discussion and helpful with new ideas.

This work would not have been possible without the help of Jason Bartell. The development of the TRANE technique was done with him alongside the entire time. He has been a great friend and lab partner over the past three years. Working closely with him over the many years has been a great experience.

I would also like to thank everyone else in the Fuchs group for their help in research and great friendships. Evan and Nick have been great office mates and I have enjoyed our many discussions in the office. Austin was great to talk to especially during the random nights and weekends when the building was empty. Isaiah has been helpful by continuing the measurements during the past couple of months of my thesis writing. Feng and Emrah have been of great resources discussing research ideas. Pai and Albert, along with all the undergrads have brought a level of enthusiasm that helps brighten up the day.

Many thanks to everyone in the Ralph and Buhrman group who have pro-

vided great assistance to the development of our lab and my research. I would also like to thank all the staff in the CNF. You have provided great insight into the development of the fabrication process. I would like to thank Steve Kriske at the CCMR for his help with all the CCMR equipment.

At Cornell, I have suffered through many physical injuries and would not have made it through without the help of my physical therapists Eva Stilwell and Karen Brigham and everyone else at Cornell Physical Therapy. You have helped me through two major surgeries, and a host of minor ailments. Your care and dedication has allowed me to leave Ithaca in good health.

Many thanks Ted Gudmundsen for being a great friend from the first day we both arrived in Ithaca. You have been there through homework assignments, running hills, lifting weights, and playing basketball. You were especially helpful in the recovery of my knee surgery and multiple emergency room visits for my shoulder. Even as you have left Ithaca, you have been a constant source of support from afar.

Thank you Taylor Woods. Over the past three years, you have been the best training partner I could ever wish for and have pushed me to better myself more than anyone. I am most grateful for your continual encouragement and motivation inside and outside the gym. I would not have made it through my shoulder surgery and recovery afterward without your help. You were always able to keep my spirits up these past few month when I was stressed with thesis writing and launching Z-Senz. And finally, you always find a way to put a smile on my face.

Thanks to Tom Dilliplane for his coaching and providing a great training haven. I thank Kimberly Hamilton and Jared Maxson for all the fun and motivation through all the grueling training sessions. I thank Eugenia Tam, Kayleigh

Muller, Chris Brown and Mohammad Hammidian for the many exciting, while sometimes ill-advised adventures. To all of the members of the intramural basketball team through the many years; you provided great comradery over the many winters. And thanks to all my friends, too many to list here.

Finally it goes without saying that owe everything to the love and support of my parents.

TABLE OF CONTENTS

LIST OF TABLES

LIST OF FIGURES

CHAPTER 1

INTRODUCTION

Magnetic materials have been known to people for thousands of years, but the origin of their properties could not be fully explained until the 1920's with the discovery of the electron spin [1]. Over the past several decades, interest in magnetic materials has grown with the development of the field of spintronics where electrical currents are used to control the magnetization of room temperature ferromagnets [2, 3, 4]. Spintronics has offered a promising route to replacing conventional electronics with higher density and speeds, and with lower power consumption. Research has suggested possible technological applications of spintronics to include magnetic random access memory (MRAM) [5, 6], nanoscale microwave sources [7, 8], and ultra-low power signal transfer [9]. Recently, MRAM technology has been applied to commercially available electronic systems [10]. The growth of spintronics has coincided with the development of real-space imaging with magnetic microscopy techniques [11], yet there currently does not exist a widely accessible micrscopy technique that can probe the fundamental length and time scales that determine the change in magnetization.

A microscopy technique capable of resolving the fundamental spatial and temporal scales of the magnetic phenomena would increase our understanding of these magnetic properties. The study of spatial variation in the magnetization has been driven by its application to magnetic storage [12], where each unit of storage corresponds to a magnetic domain. Therefore, the fundamental length scale of magnetic materials is set by the domain wall width, where the domain wall is the transition region between magnetization of opposite po-

larities. The length scale of the domain wall is set by the interaction strength between the spin exchange energy and the magnetic anisotropy, leading to domain wall widths ranging from 10-200 nm due to the stiffness of the magnetic material. Recently, a new class of materials has been discovered with Skyrmion spin textures, which have been proposed for memory devices [13, 14]. Coincidentally, the Skyrmion size ranges from 10-200 nm, which is set by the competition between the exchange and the Dzyaloshinskii-Moriya interaction [15]. The oscillation of the magnetization sets the fundamental time scale of the magnetic materials. Magnetic oscillations can occur in various forms such as ferromagnetic resonance (FMR) [16], spin waves [17, 18], and spin pumping [19, 20]. The time scale of these oscillations are determined by the gyromagnetic ratio, the magnetic moment of the sample, and the applied magnetic field, which can lead to oscillations as fast as 5-50 ps.

Currently, there does not exist a widely accessible microscopy technique that can resolve magnetic moments in the regime of 10-200 nm and 5-50 ps. There are several techniques to image real-space magnetization, each with their advantages and disadvantages; these include magnetic force microscopy (MFM), Lorentz tunneling electron microscopy (TEM), spin-polarized scanning tunneling microscopy (SP-STM) and magneto-optical techniques. The majority of these techniques are not capable of temporally resolving magnetic dynamics. MFM can measure magnetic dynamics in the frequency domain with using ferromagnetic resonance force microscopy (FRFM) [21], but cannot measure dynamics in the time-domain. Lorentz TEM has temporal resolution of approximately 1 s [22] and STM has temporal resolution limited to 100 kHz [23], therefore these techniques cannot achieve the temporal resolution necessary to study magnetic dynamics. Currently, magneto-optical techniques are the only capable

method of measuring magnetic dynamics in the time domain with GHz resolution.

Magneto-optical techniques measure the magnetic moment by analyzing how the light polarization is influenced by the magnetic material [24, 25, 26, 27]. Using laser pulses as short as femptoseconds, magneto-optical techniques have been highly successful in measuring magnetic dynamics with sub-picosecond temporal resolution [28]. The spatial resolution of magneto-optical techniques is limited by the diffraction limit that scales as $\lambda/2NA$ where λ is the wavelength of light and NA is the numerical aperture [29]. With table-top techniques can reach down to approximately 400 nm to produce spatial resolutions of approximately 200 nm. This is still far above the feature size of magnetic textures.

To improve the spatial resolution, one option is to reduce the wavelength by using x-rays to measure magnetism with x-ray magnetic circular dichroism (XMCD) [30, 31]. With current technology, XMCD is capable achieving spatial resolution down to 15 nm [32, 33] and temporal resolution less than 100 ps [34, 35]. The main drawback of XMCD is that it requires a synchrotron facility to generate the x-rays, therefore the size and cost involved makes the technique difficult for widespread adoption.

To circumvent the diffraction limited spatial resolution with optical microscopy, near-field techniques have been developed to obtain optical spot sizes of that are less than sub-diffraction limited spatial resolution [36, 37]. Techniques involve confining light with tapered optical fiber and coated with a metal aperture, with a sub-diffraction sized opening. Magneto-optical studies using near-field microscopy have been performed [38, 39, 40, 41], where the later was able to obtain spatial resolution down to 10 nm. The poor collection efficiency

of the near field technique leads to a low signal to noise ratio when compared to conventional far field techniques. The low signal to noise makes stroboscopic time-resolved measurements are very difficult, therefore it has only been applied to limited systems [42].

Ultimately, the spatial resolution of magneto-optical measurements are fundamentally limited by the diffraction limit of light. This has lead to techniques with x-ray or near field microscopy, but due to the complexities involved with such measurements, widespread use of these techniques cannot be achieved. Ideally, we would like a table-top microscopy technique that provides the necessary spatial and temporal resolution to study magnetic dynamics. In this thesis, we look to use heat instead of light to probe the magnetization since it does not have such a fundamental limit to its spatial confinement.

The concept of using thermal effects to study magnetic materials has become a growing field in recent years. Thermoelectric effects in magnetic materials have been shown to interact with spin currents [43, 44, 45]. The recent interest in the field of spin caloritronics arose due to the discovery of the spin Seebeck effect [46]. The spin Seebeck effect allows spin currents to be driven without applying an electric field. This has lead to the study of spin caloritronics for magnetic insulators [47, 48] and magnetic semiconductors [49]. Many of the current studies of spin caloritronics find the anomalous Nernst coefficient to be large relative to the spin Seebeck effect [50, 51, 52].

Previous studies have demonstrated that by confining the temperature gradient to a micron-scale region in a thin-film ferromagnetic metal, an anomalous Nernst voltage is generated proportional to the local magnetic moment [53, 54, 55, 56]. Currently, there have been no studies on how the temperature gradi-

ent confinement relates to the thermal heat spot, or the time evolution of the temperature gradient to measure magnetic dynamics. In this thesis, we are able to set an experimental upper bound of 30 ps for the temperature gradient in ferromagnetic metals, which is supported by numerical simulations suggesting a width of 10 ps. For the spatial resolution, we experimentally show that the temperature gradient is confined to the same size as the thermal source when using a laser spot with a Gaussian width of 310 nm. This experimental result is confirmed with numerical simulations, and further we show that this holds true down to heat sources of 50 nm in width. These results suggests that using a heat confining plasmon antenna would provide a route for a high resolution spatiotemporal magnetic microscope on a table-top.

CHAPTER 2

TRANE THEORY

2.1 Anomalous Hall Effect

In 1879, Edwin H. Hall discovered that conducting electrons are deflected in the presence of a magnetic field, leading to an overall electric potential [57]. This discovery is what we now know as the Hall effect. Shortly after, Hall reported a much larger electric potential when measuring the Hall effect with ferromagnetic metals [58]. This large effect would later be known as the anomalous Hall effect. Approximately 40 years after Hall's discovery, Smith and Pugh investigated the anomalous Hall effect in various ferromagnetic metals [59, 60, 61]. By doing so, they empirically determined the relationship between the overall Hall resistivity and the magnetization of the ferromagnetic metal to be

$$\rho_H = \rho_0 H + \rho_1 M(T, H), \tag{2.1}$$

where ρ_0 and ρ_1 are the ordinary and anomalous Hall coefficients respectively, H is the applied magnetic field, and M is the average magnetization over the sample. ρ_1 is material dependent and depends on other factors such as the electrical resistivity and crystal growth. Eq. 2.1 shows a linear relationship between the magnetization and the Hall resistivity. This linear relation in conjunction with thermal effects forms the basis of the TRANE technique.

The theory of the anomalous Hall effect is still an ongoing topic of research, where the mechanism depends on the specific magnetic material. The possible mechanism for the anomalous Hall effect include an intrinsic band structure effect [62, 63, 64], skew scattering [65, 66] and side jump [67]. We will not go into

the details of the mechanisms, since our technique does not distinguish between the different mechanisms. An overview of the mechanisms are discussed in the review paper by Nagaosa *et al.* [68].

2.2 Thermoelectric Effects

Temperature gradients create a difference in the electron chemical potential, therefore leading to the motion of electrons. The Seebeck effect is the electric field generated by a temperature gradient, which is described by [69]

$$\vec{E} = S\vec{\nabla}T, \tag{2.2}$$

where S is the Seebeck coefficient. The Seebeck effect leads to thermoelectric transport measurements that are analogous to traditional electrical transport measurements, where instead of applying an electric field, we apply a temperature gradient. We show these electrical and the analogous thermoelectrical transport measurements in Fig. 2.1. The Nernst effect is the thermoelectric equivalent to the Hall effect, where an applied temperature gradient replaces an applied electric field. Similarly, the anomalous Hall effect is the thermoelectric equivalent of the anomalous Hall effect. The anomalous Nernst effect produces an electric field given by

$$E_{ANE} = -N\vec{M} \times \vec{\nabla}T, \tag{2.3}$$

where N is the anomalous Nernst coefficient [70, 71, 72]. Since the anomalous Nernst effect is a combination of the anomalous Hall effect and Seebeck effect, the anomalous Nernst coefficient can be expressed in terms of

$$N = \frac{\rho_{xy}^{AHE}}{\rho_{xx}} S = \frac{\rho_1 M(T,H)}{\rho_{xx}} S, \tag{2.4}$$

where ρ_{xx} and ρ_{xy} are the diagonal and off diagonal resistivity of the ferromagnetic metal [73, 74].

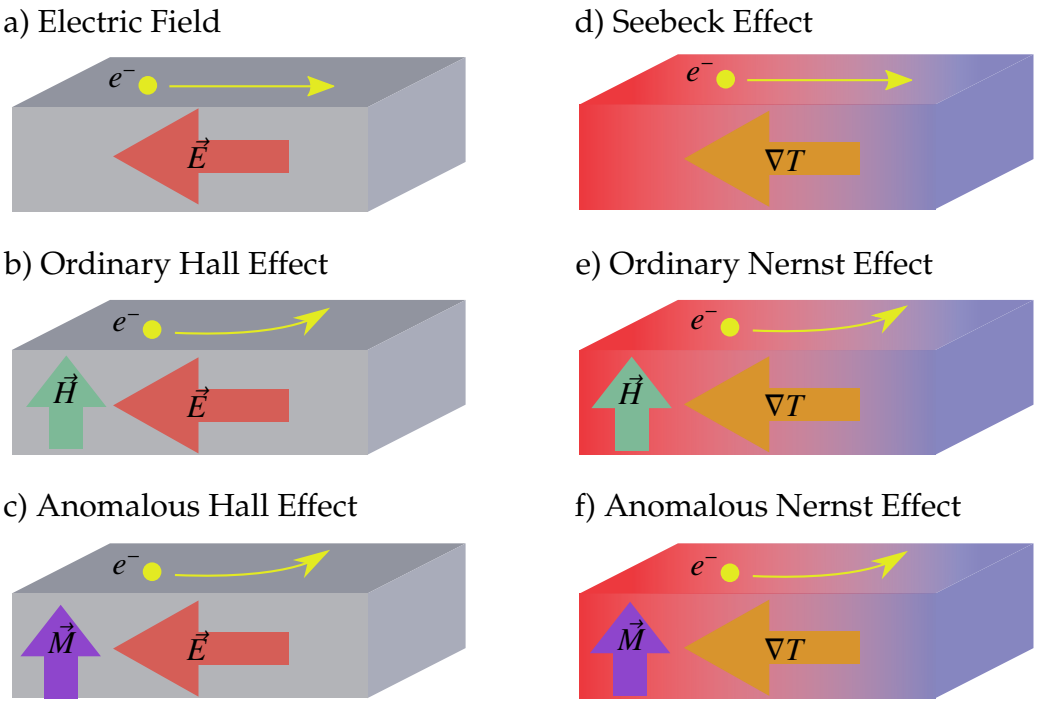

Figure 2.1: Electrical transport measurements and their corresponding thermoelectric transport measurements

2.3 Measuring Magnetic Moment with the Anomalous Nernst Effect

The basis of our microscopy technique is to utilize the anomalous Nernst effect to measure local magnetic moments. In a ferromagnetic metal, a spatially localized and short time lived temperature gradient, through the anomalous Nernst effect, will create an electric field that is also spatially localized and short time lived. This electric field is proportional and mutually perpendicular to the tem-

perature gradient and the magnetic moment. Therefore, by measuring the total voltage, we can determine the spatially local magnetic moment over a short time period. The TRANE microscopy technique generates this temperature gradient and measures the electrical voltage to spatiotemproally resolve the magnetic moment.

TRANE is designed to measure in-plane magnetic moments of thin film ferromagnetic samples, fabricated on an insulating substrate, with electrical contacts. The necessary geometry to operate TRANE is depicted in Fig. 2.2. By generating an out-of-plane temperature gradient, the anomlous Nernst effect creates an in-plane electric field, which is perpendicular to the in-plane magnetic moment. This electric field produces the anomalous Nernst voltage, which we measure with the electrical contacts. From the geometry depicted in Fig. 2.2, we measure the y-component of the magnetic moment. The experimental capabilities to generate a localized temperature gradient in space and time the following spatial and temporal resolution of TRANE.

In this thesis, we use a focused laser to create a focused heat spot, which generates the temperature gradient for TRANE microscopy. There are several advantages of using the laser to generate a temperature gradient versus other heat generation techniques. First, experimental technique to generate a focused laser spot is well established. Secondly, spatial scans with the focused laser spot across the device under study can be done with high speed and accuracy over a large field of view. Finally, we can create very short laser pulses, which will result in very short temperature gradients in the sample.

The disadvantage of using the laser to create the heat spot is that the heat spot confinement is limited by the diffraction limit. Alternatively, we can

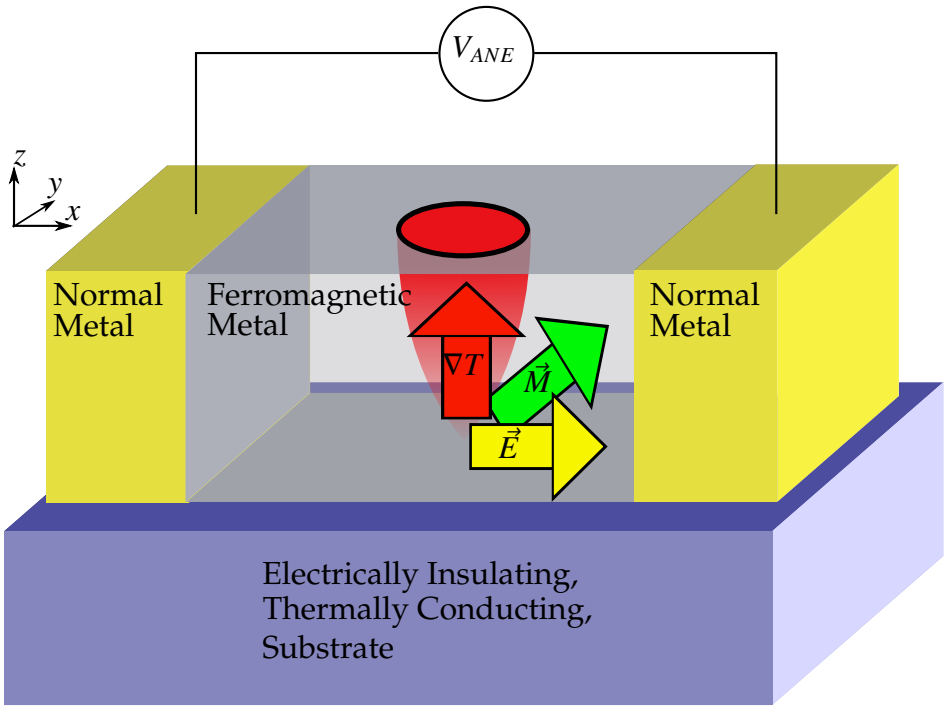

Figure 2.2: The geometry of the TRANE setup

use a plasmonic antenna to focus the heat spot, which has been previously demonstrated with heat-assisted magnetic recording to create a thermal spot of 50 nm [75, 76]. To use plasmonic antennas in a fully functional scanning TRANE microscope will require further engineering, which is currently work in progress, but will not be discussed in this thesis. We will show in this thesis that if 50 nm thermal spot can be created with TRANE, it will have spatial resolution of 50 nm, equaling the thermal spot size.

2.4 TRANE Signal

We use a resistor model to predict the total time-dependent voltage induced by the anomalous Nernst effect, V_{ANE}, which TRANE measures across the electrical contacts. The signal V_{ANE} can be calculated by subdividing the sample into blocks as shown in Fig. 2.3, where the resistivity, temperature gradient, and magnetic moment are uniform within each block, and each block has dimensions of δx, δy and δz. The current generated by the anomalous Nernst effect for each of these blocks is given by

$$I(\vec{x},t) = J(\vec{x},t)\delta y\delta z = \frac{-N\delta y\delta z}{\rho(\vec{x},t)}\vec{M}(\vec{x},t)\times\vec{\nabla}T(\vec{x},t), \tag{2.5}$$

where J is the current density and ρ is the local resistivity.

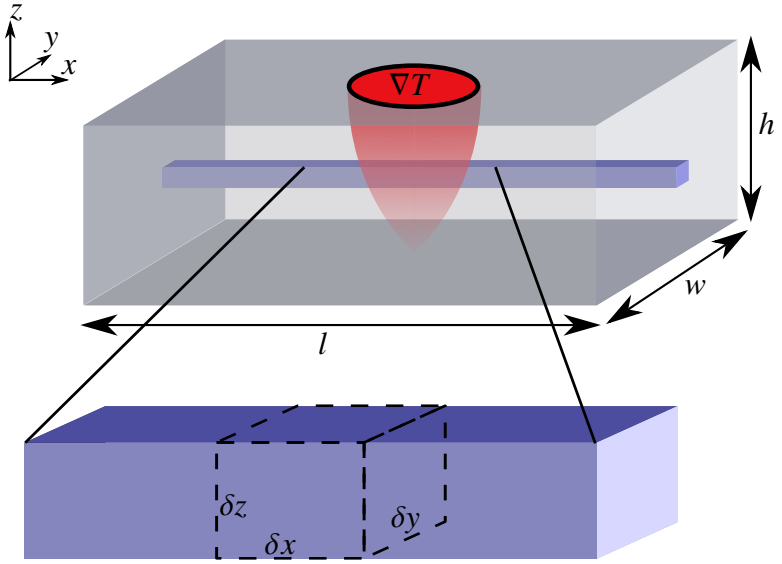

Figure 2.3: The geometry to describe the resistor model.

By subdividing the sample into uniform blocks, the system can be modeled as a 3-dimensional resistor lattice model with current sources introduced to account for the current generated by the anomalous Nernst effect. A depiction of

this model is shown in Fig. 2.4, where each lattice point corresponds to a block in the subdivision of Fig. 2.3. Such multi-dimensional resistor networks have been widely studied with various approaches [77, 78, 79, 80]. For the added complexity of the non-uniform current source from the anomalous Nernst effect, finite element method numerical simulations would be most suitable to estimate V_{ANE}. The full calculations of such a model is work in progress but is beyond the scope of this thesis.

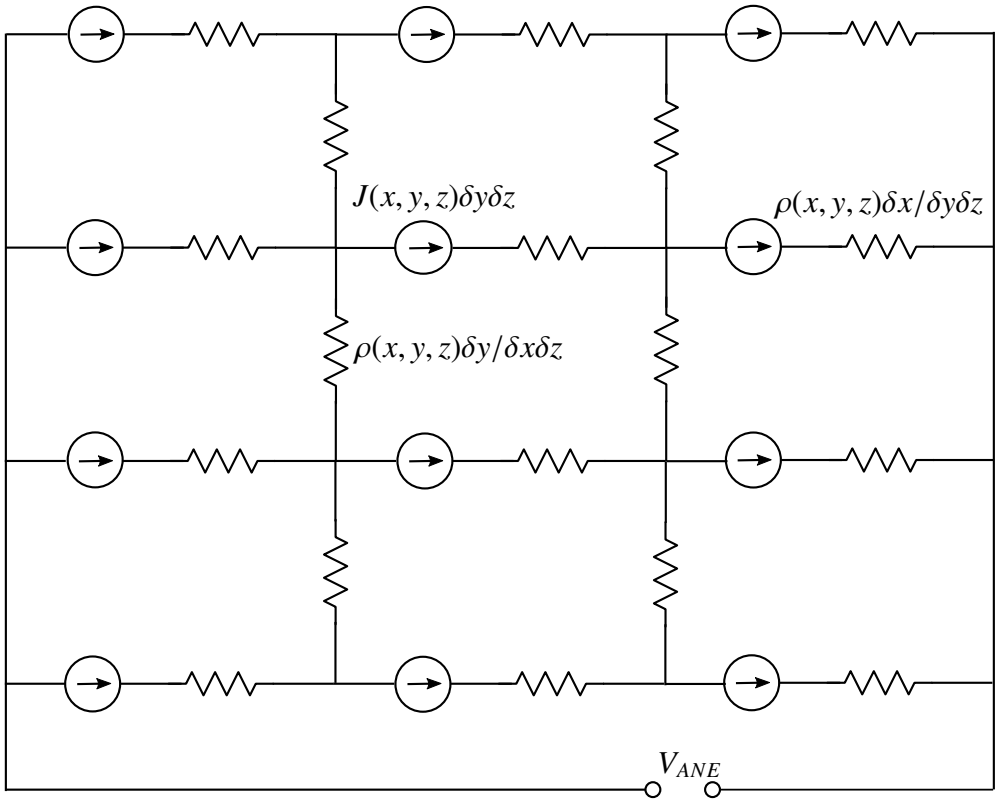

Figure 2.4: The x-y cross section of the 3-d resistor model to calculate the total signal.

2.4.1 Simplified Resistor Model

To understand the signal V_{ANE} in relation to the sample geometry and thermal spot size, we use a simplified version of a resistor model where we assume that the current is uniform along the length of the sample, which is not true of the physical sample due to transverse currents. The circuit representation of the simplified resistor model is shown in Fig. 2.5. This simplified model is only valid in the thin film limit, with uniform resistivity, and linear response.

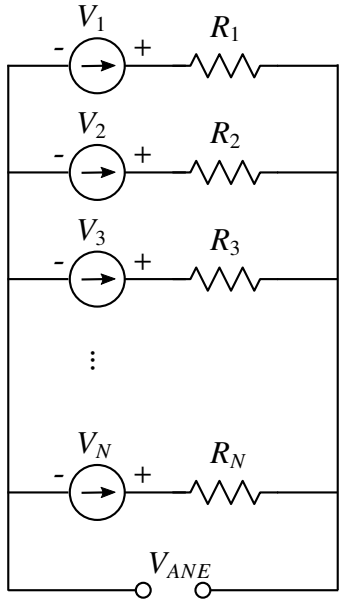

Figure 2.5: The simplified resistor model to predict the total signal.

Using this simplified resistor model, we determine the electric potential across a small cross-sectional area of $\delta y\, \delta z$ along the length of the wire, l, at the position $y = y_k$, $z = z_k$, with

$$V_k = \int_0^l -\vec{E}(x, y = y_k, z = z_k)\, dx. \tag{2.6}$$

Each of the cross-sectional areas act as parallel circuit components connected to the electrical contacts of the sample.

Using the simplified resistor model, we can calculate V_{ANE} from Kirchhoff's laws to be

$$V_{\mathrm{ANE}} = V_k + i_k R_k, \ \forall k, \tag{2.7}$$

where V_k, i_k and R_k correspond to the voltage, current and resistance along the total length of the wire in the infinitesimal cross-section. The current is conserved such that

$$\sum_k i_k = 0. \tag{2.8}$$

One can solve for the anomalous Nernst voltage to show

$$V_{\mathrm{ANE}} = \left(\sum_k \frac{1}{R_k} \right)^{-1} \left(\sum_k \frac{V_k}{R_k} \right), \tag{2.9}$$

where the resistance R_k is given by

$$R_k = \frac{1}{\delta y \, \delta z} \int_{-L/2}^{L/2} dx \, \rho(T(\vec{x})), \tag{2.10}$$

with the resistivity, ρ, is a function of the spatially dependent temperature, T. The voltage V_k due to the anomalous Nernst effect is given by

$$V_k = \int_{-L/2}^{L/2} dx \, N \vec{\nabla}_z T(\vec{x}) \times M(\vec{x}), \tag{2.11}$$

where N is the anomalous Nernst coefficient and M is the magnetic moment.

For further simplification, we assume the laser spot size to be uniform and circular with radius r, generating a uniform temperature gradient throughout the thickness of the sample. We also assume that the resistance change due to the temperature increase is minimal in its contribution to the anomalous Nernst voltage. For a uniform magnetic moment at the laser spot, the signal is

$$V_{\mathrm{ANE}} = \left[N(\vec{M} \cdot \hat{y}) \nabla_z T \right] \frac{\pi r^2}{w}. \tag{2.12}$$

Therefore, the signal scales with the geometry of the sample and the laser spot by r^2/w. One should note that because of the picosecond time duration of the

voltage pulse, the measured signal has a maximum occurring when the sample impedance matches the 50 Ω impedance of the measurement circuit.

CHAPTER 3

TRANE EXPERIMENTAL SETUP

3.1 Optical Setup

Our current TRANE microscopy apparatus measures the magnetic moment with a localized temperature gradient generated by a focused pulsed laser onto the surface of the sample. The optical setup to generated the focused laser spot is shown in the photograph of Fig. 3.1, where all the optical elements are placed on a 5'×10' optical table. We show the schematics of the optical setup for TRANE in Fig. 3.2. Using this optical setup, we focus our pulsed laser with a high numerical aperture (NA) objective, where the proper position is determined from the combination of a camera and photodiode detectors.

The pulsed laser used for our setup is a Coherent MIRA Ti:Sapphire laser tuned to output at a wavelength of 794 nm. The Ti:Sapphire crystal in the MIRA is pumped with a Coherent Verdi laser which outputs a wavelength of 532 nm and has a total output power of 10 W. The Ti:Sapphire laser is operated in the picosecond mode, where passive Kerr lens modelocking generates laser pulses of approximately 3 ps with a repetition rate of 76 MHz. To keep the laser system in equilibrium, we chill the Verdi pump laser and the Ti:Sapphire crystal with a water chiller and purge the MIRA laser cavity with N_2. With optimal alignment, the maximal average power at the output of MIRA is approximately 1.8 W.

The optical polarizer and pulse picker allow us to reduce the overall laser repetition rate by picking which pulses to transmit and block all others. The pulse picker model is a ConOptics 350-160, which uses a Pockels cell consisting

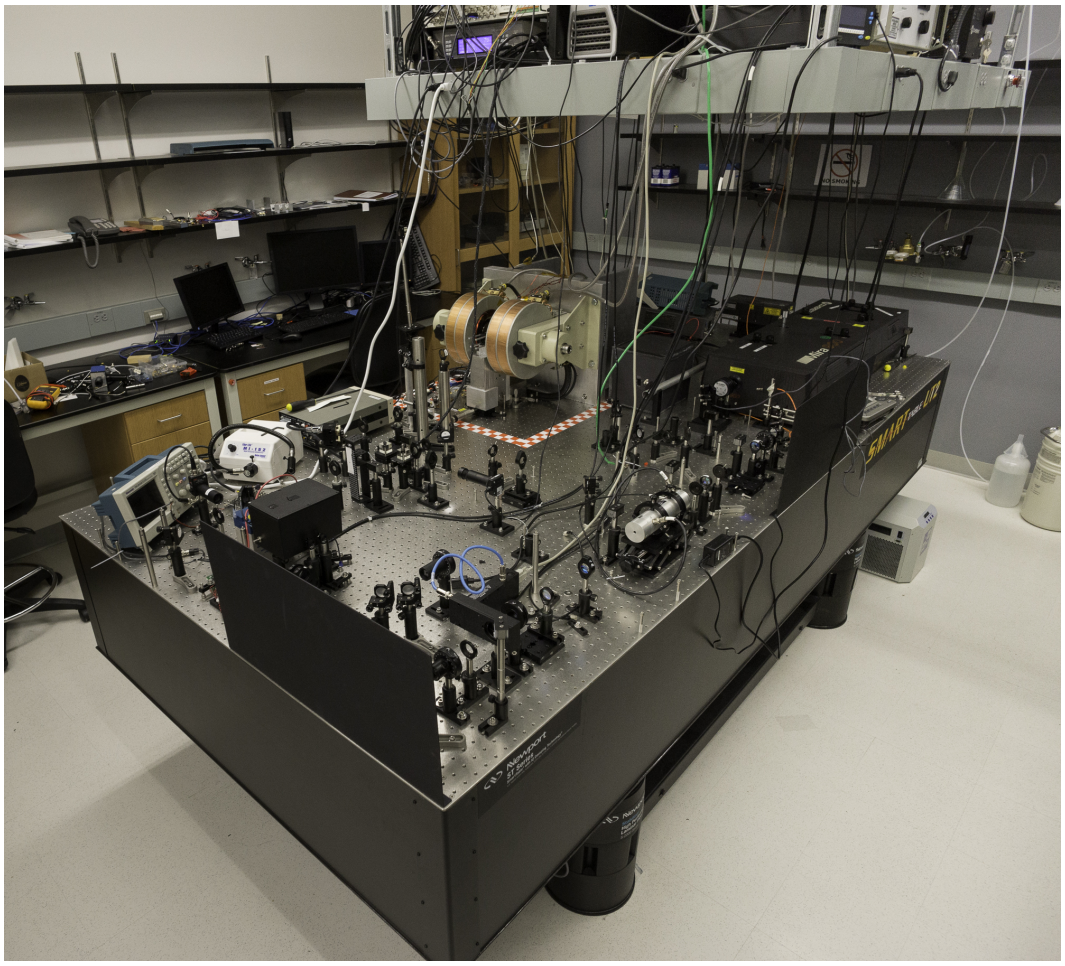

Figure 3.1: Photograph of the entire TRANE setup.

of an electro-optic modulator to create an electric voltage dependent wave retardance [81]. This rotates the overall polarization of the light depending on the controller defined electric voltage. The light then passes through a polarizing beam splitter which will pick off the desired laser pulses. With this pulse picker, we measure with a fast photodiode an extinction ration of approximately 100:1. In this thesis, the measurements of the static magnetic moments do not use the pulse picker to reduce the repetition rate, thus it is measured with a repetition rate of 76 MHz. For the measurements of magnetic dynamics, we use the pulse picker to block two pulses and let every third pulse pass through, resulting in

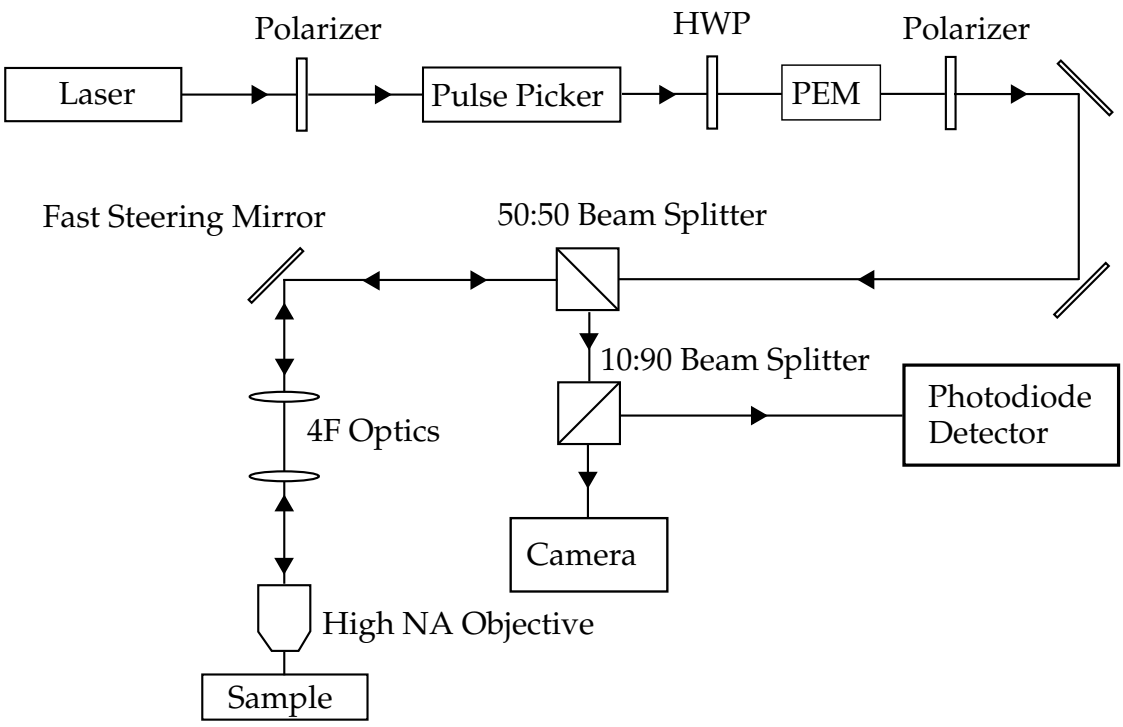

Figure 3.2: The basic optical setup to measure TRANE.

a repetition rate of 25.3 Mhz. We choose a lower repetition rate for measuring magnetic dynamics to ensure the sample returns to thermal equilibrium before the following laser pulse.

3.1.1 Laser Modulation

The optical elements of the half wave plate (HWP), photoelastic modulator (PEM) and polarizer combined allow us to modulate the power of the laser, which we reference with the lock-in amplifier. The HWP is set to 22.5^o from the fast axis to rotate the polarization by 45^o, aligning the polarization to the fast axis of the PEM. The PEM effectively operates as a HWP rotating at a frequency of 50 kHz. Therefore, after the polarizer, the total power modulates at

100 kHz. Previous versions of our TRANE setup used an optical chopper wheel to modulate the laser power. The optical chopper wheel was replaced with the photoelastic modulator due to the mechanical instability of the optical chopper wheel, which results in poor frequency and phase stability. With the optical chopper, at 10 kHz, the frequency stability is approximately 1 Hz. In comparison, the PEM modulating the laser power at 100 kHz, has a frequency stability of less than 0.5 Hz.

3.1.2 Spatial Scanning

The device we measure with TRANE is wax mounted to a brass sample holder and wire bonded to gold waveguides that are soldered to SMA ports. The sample holder is fastened to a 3-axis micrometer stage, which provides coarse positional control with independent motion in all three directions. The micrometer controlled stage has translational precision of approximately 1 μm. When performing TRANE measurements, we tighten the locking nuts to reduce any motion due to thermal fluctuations and interactions with the applied magnetic field. We can determine the laser position relative to the sample from the camera with the addition of a white light source along the optical path.

For the fine positional controls, we use a fast steering mirror (FSM) with a 4F lens system shown in Fig. 3.3 [82]. The fast steering mirror is actuated by small voice coils, where an applied voltage controls the angle of the light reflected off the mirror. Our 4F lens system consists of two 8" focal length lenses, such that we place the FSM and back aperture at 4 times the focal length apart and the two lenses are placed at the focal length from the FSM and back aperture re-

spectively as shown in Fig. 3.4. As depicted in Fig. 3.4, the 4F lens system keeps the laser position constant at the FSM and the back aperture of the objective, while also setting the angle from the FSM to equal the angle entering the back aperture. By changing the angle of the light entering the back aperture, we can scan the position of the focused light at the sample. The position of the laser spot as a function of the applied FSM voltage is calibrated with a known sized TEM grid.

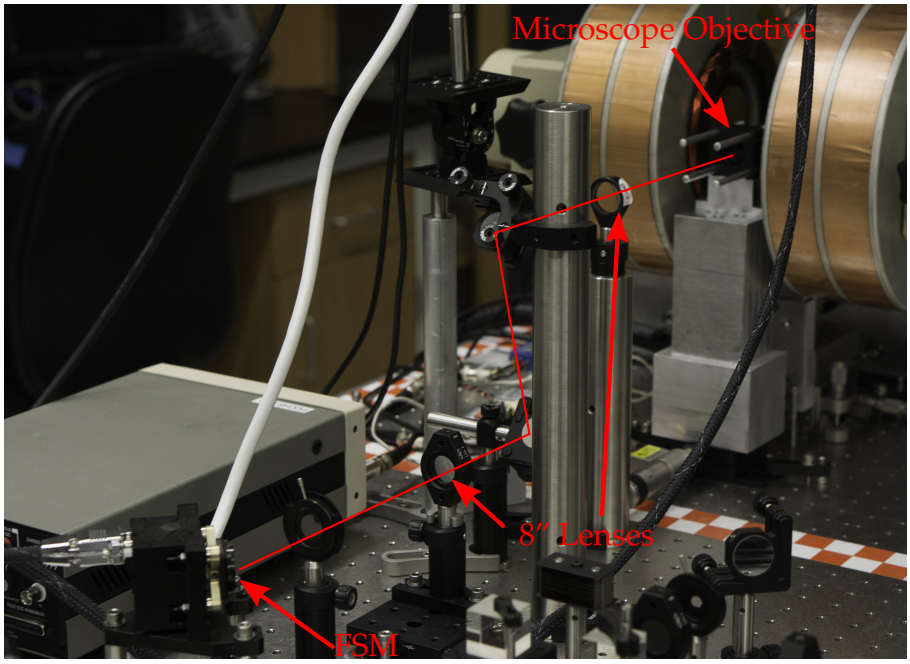

Figure 3.3: A photograph of the fast steering mirror and 4F lens system for fine position control.

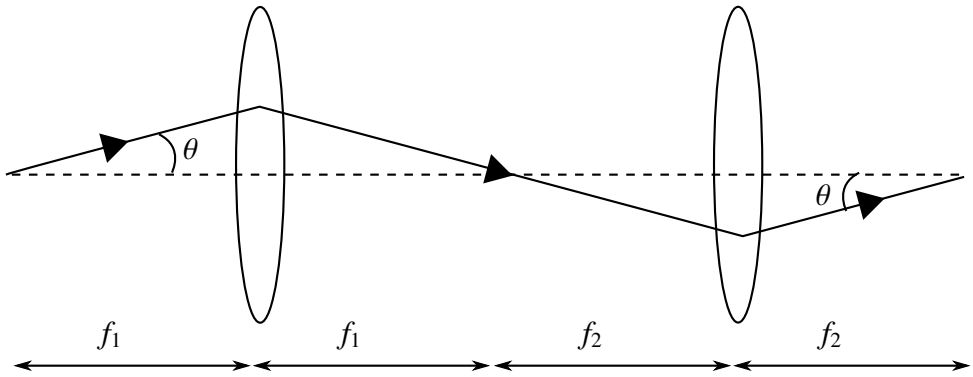

Figure 3.4: A depiction of the 4F lens system.

3.1.3 Microscope Objective and Focus

To focus the laser onto the sample, we use a Nikon microscope objective with a 0.9 numerical aperture (NA). The point spread function of the optical power, I, in the lateral direction can be treated as a Airy disk such that [83]

$$I(\rho) = 2\frac{J_1\left(\pi\rho/(\lambda/2\mathrm{NA})\right)}{\pi\rho/(\lambda/2\mathrm{NA})}, \tag{3.1}$$

where $\rho = \sqrt{x^2 + y^2}$. The diffraction limited lateral resolution of the objective, r, is set by the Rayleigh criterion, given by [84]

$$r = \frac{1.22\lambda}{2\,\mathrm{NA}}, \tag{3.2}$$

where λ is the wavelength of the light used and NA is the numerical aperture. The Rayleigh criterion states the focused optical spot can be modelled with an Airy disk, where the resolution is set by the distance from the peak to the first node. For our 794 nm light, we have diffraction limited resolution of 538 nm. It is more practical to approximate the point spread function as a Guassian such that

$$I(\rho) \approx A\exp\left(-\frac{\rho^2}{2\sigma^2}\right), \tag{3.3}$$

where A is the normalized amplitude and $\sigma = \frac{0.42\lambda}{2NA}$ [85]. Therefore, from the Rayleigh criterion, the theoretical diffraction limit results in a point spread function with an approximate Gaussian width of $\sigma = 185$ nm.

We experimentally determine the lateral resolution of the laser spot by measuring the reflectance when scanning across an e-beam lithography defined 2 μm wire. We plot the reflectance as a function of position in when scanning across the wire in Fig. 3.5. To determine the resolution, we fit the reflectance scan with a convolution of two step functions spaced 2 μm apart and Gaussian function, $Ae^{-[(x-x_0)/(2\sigma)]^2}$, where A is the amplitude, x_0 is the central position, and σ is the Gaussian width. We fit the convolution with the method of least squares, by using the width, amplitude and central position as free varaibles and show the result in Fig. 3.5. From this fit, we find that our apparatus can create a focused spot with a Guassian width of $\sigma = 310 \pm 15$ nm, which is larger than the theoretical minimum, suggesting that we are not measuring at the diffraction limit.

The focal depth of the microscope object, Δz, is given by the following equation [86]

$$\Delta z = \frac{\lambda}{4n\left(1 - \sqrt{1 - \left(\frac{NA}{n}\right)^2}\right)}, \tag{3.4}$$

where n is the index of refraction. For our 0.9 NA microscope objective with 794 nm light, the focal depth is 350 nm. Therefore, to properly focus the laser spot on the sample surface, we must have precise linear positioning of the microscope objective relative to the sample. We place the objective upon a linear translation stage controlled by a piezo driven micrometer to control the linear position of the objective. This piezo driven micrometer has coarse control that is set by hand, and fine control set by a voltage controller. The linear position of the

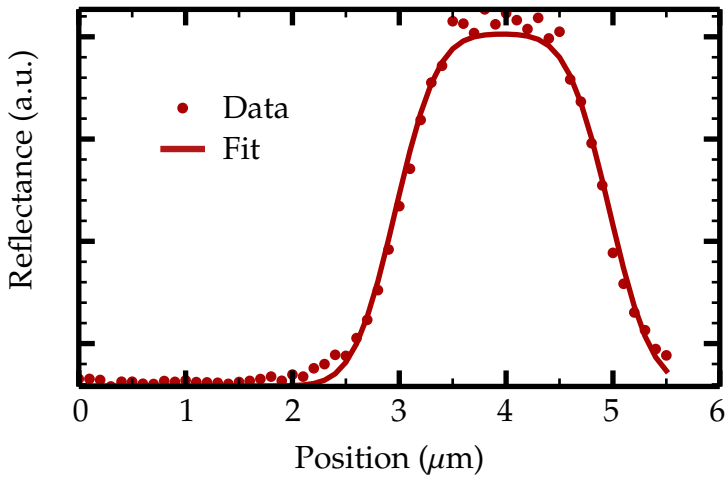

Figure 3.5: Scanning across a sharp edge to measure the resolution of the microscope objective.

piezo micrometer cannot be directly set by the applied voltage due to hysteresis in the position due to backlash. Instead, a feedback strain gauge determines the micrometer position.

The high magnification objective with its small depth of field is highly influenced by an applied magnetic field. For our objective, all ferrous parts have been removed, yet it is still influenced by the field possibly due to eddy currents. Fig. 3.6 plots the reflected light measured in the photodiode as a function of the applied magnetic field, which shows a change of approximately 5% in the photodiode measurement of the reflected light over a change in magnetic field of 750 Oe. Since the measured reflectance is highly dependent on the position of the objective due to the focus, Fig. 3.6 shows how the objective position is highly influenced by the applied field. Our TRANE setup can measure the magnetic moment at high fields, but has difficulty when we require a large change in the applied mangetic field.

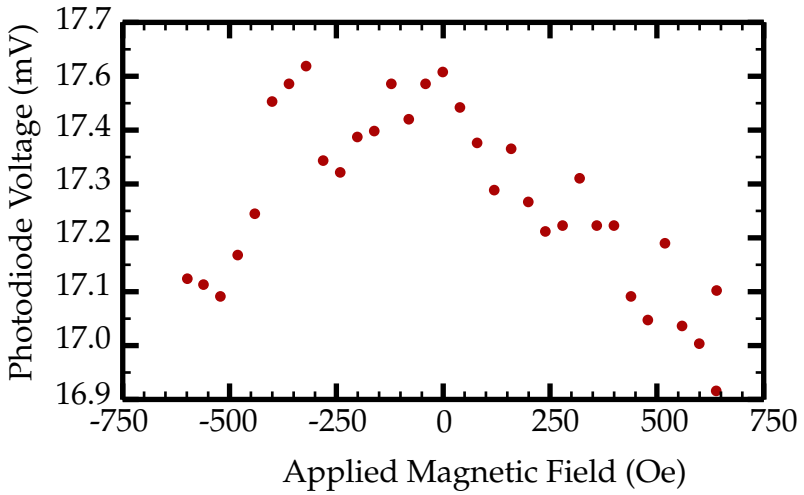

Figure 3.6: The measure of reflected light in the photodiode voltage as a function of the applied magnetic field.

The optimal focus is determined by finding the highest optical reflectance measured in the CMOS camera as a function of the lateral position. To improve the reproducibility of results, we use an automated autofocus program by measuring with the camera and setting the position with the piezo control. High accuracy and reproducibility of the focus is needed for experiments requiring long time averaging or large changes in the applied magnetic field. It is also necessary for measurements devices of small feature sizes or measuring near the electrical contact pads. If the objective is not focused, the laser spot may not be properly placed on the device or may partially lay over the contact which introduces large artifacts. It is important to note that for devices with feature sizes of approximately 1 μm or below, the focus cannot be determined by measuring the reflectance of the device due to edge artifacts. To measure such small devices, we fabricate a large focusing pad of the same height near the device. The optimal position is determined by focusing on the pad then translating the proper displacement to measure the device.

3.2 Applied Magnetic Field

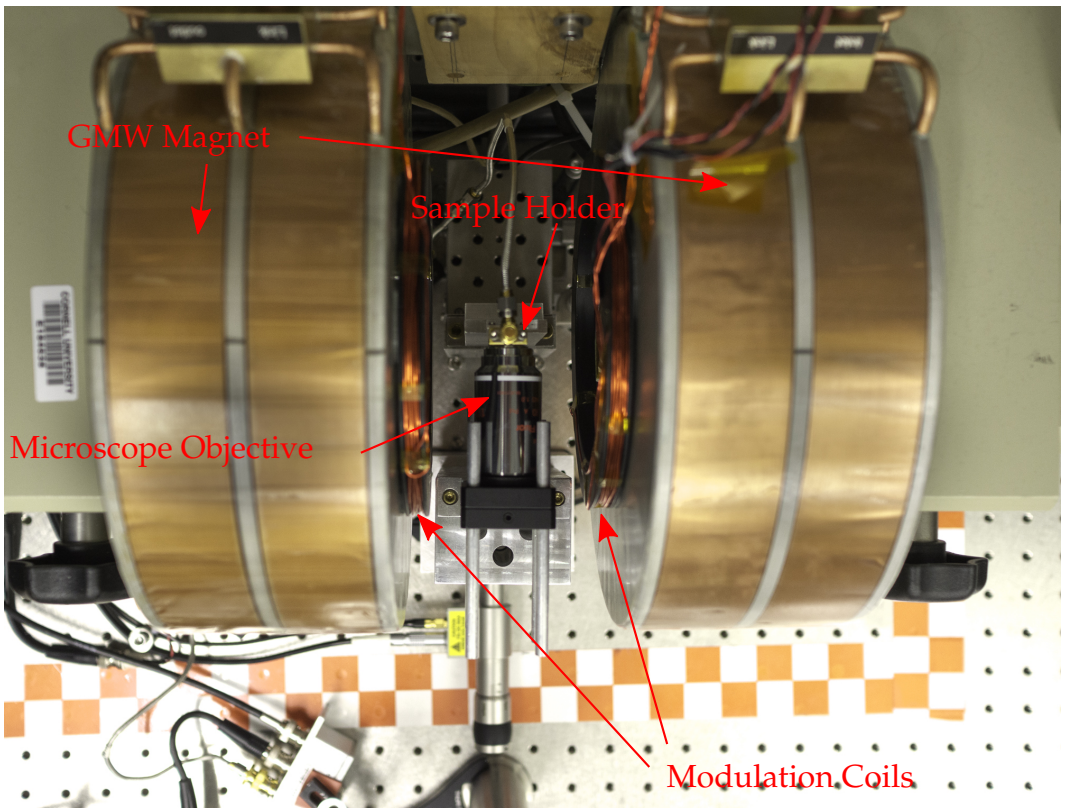

Figure 3.7: Photograph of the electromagnet and modulation coils used to generate the in-plane magnetic field at the sample.

Figure 3.7 shows the photograph of the GMW electromagnet and modulation coils used to apply a magnetic field at the sample. We use a GMW electromagnet to a apply a static magnetic field at the sample. The magnetic field is generated by applying a DC electric current from a bipolar BOP power supply. The static magnetic field generated by the electromagnet is measured with a Hall probe, which is calibrated with a commercial Gaussmeter. The electromagnetic can produce fields up to 1 T.

We use two different methods to modulate the field in our measurements. The first method is to modulate the total current passed into the electromagnet.

We accomplish this by controlling the BOP output current with an analog -10 to 10 V signal. The modulated current is created by an analog input signal, which is the voltage sum from a sinusoidal voltage and a DC offset, created by a LabView program with the DAQ output. Due to the inductance of the electromagnet, the highest frequency that can be reached with this method is approximately 30 Hz.

To create modulating AC magnetic field of higher frequencies, we use two hand made coils attached to the inside of the magnet as shown in Fig. 3.7. These coils are powered with an audio amplifier whose frequency is set by the lock-in amplifier oscillator output. The coils can generate a modulating magnetic fields with frequencies above 1 kHz. Due to the inductive coupling between the modulation coils and the GMW magnet, for a set reference signal and amplification, the modulation field varies as a function of the frequency, with higher fields at lower frequencies.

3.3 Electrical Circuit for TRANE Detection

To measure the anomalous Nernst voltage created by the laser induced temperature gradient, we use the collection circuit depicted in Fig. 3.8. The use of the mixer allows us to create a homodyne like measurement by converting the time-varying anomalous Nernst voltage, $V_{ANE}(t)$ into a DC voltage, which we label as V_{TRANE}. For a set reference mixer pulse, we will show in Sec. 3.3.3 that $V_{TRANE} \propto V_{ANE}^{peak}$, where V_{ANE}^{peak} is the peak voltage in time of V_{ANE}. We note that the bandwidth of the amplifiers and mixer do not influence the temporal resolution of TRANE for the measurement of magnetic moment dynamics.

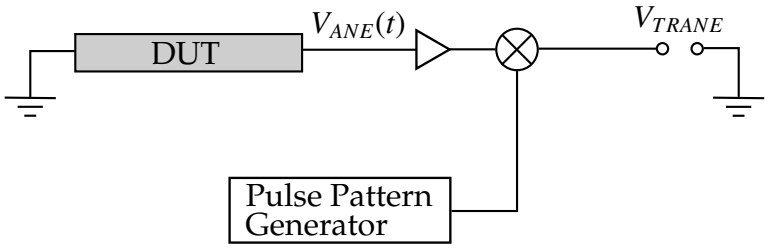

Figure 3.8: The collection circuit to measure the anomalous Nernst voltage.

3.3.1 Pulse Delay Timing

To properly measure V_{TRANE}, the reference pulse from the pulse pattern generator needs to be correctly timed to match the voltage pulse $V_{ANE}(t)$. The two voltage pulse inputs into the mixer, $V_{ANE}(t)$ and V_{ref} both have triggers originating from the laser. The time delay for V_{ANE} is the sum of the time from the optical path of the laser pulse from the laser source to the sample, the generation of the temperature gradient in the sample, and the electrical wires and circuit components. The time delay for V_{ref} is caused caused by the electrical wires and circuitry plus the controlled delay in the pulse pattern generator. Therefore, by properly setting the controlled delay in the pulse pattern generator, we match the overall time delays such that the voltage pulses of V_{ANE} and V_{ref} are matched at the mixer. Fig. 3.9 shows the mixer output of a typical sample as a function of the pulse delay from the pulse pattern generator. As we vary the pulse delay set by the pulse pattern generator, we can clearly see a delay where the mixer output voltage is at a maximum (5.2 ns for Fig. 3.9). This time corresponds to the proper pulse delay from the pulse pattern generator to correctly measure V_{TRANE}.

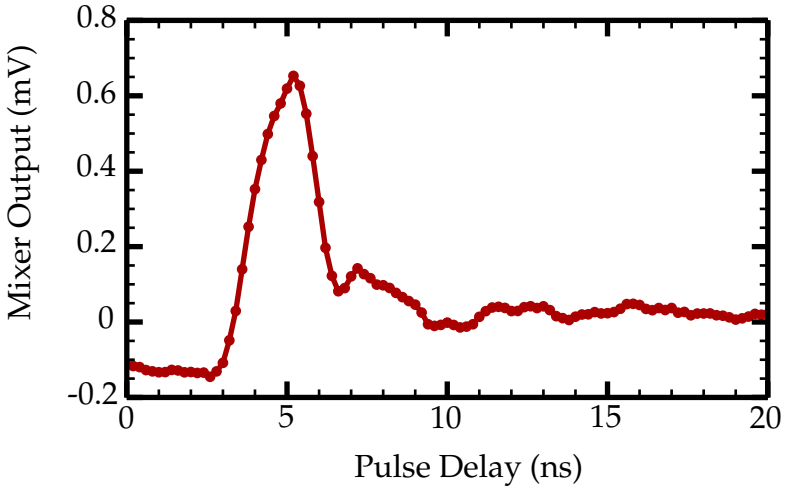

Figure 3.9: The mixer output voltage as a function of the pulse delay set in the pulse pattern generator.

3.3.2 Bandwidth of Frequency Mixer

This section shows how the temporal resolution of TRANE is only dependent on the time scale of the thermal gradient decay and not dependent on the bandwidth of the collection circuit. We discuss how the mixer is used to detect the pulsed signal and the intricacies involved with the bandwidth limitation. An ideal frequency mixer outputs the voltage multiplication between two input ports. Here, we label one input as the sample voltage and the second input as the reference or local oscillator. If we set the local oscillator to a fixed frequency sine wave, then the mixer acts as a homodyne detector at the local oscillator frequency when measuring the DC component of the output. We will show that the mixer can be used for a homodyne-like detection of a pulse train signal.

To show the mixer output with a pulse train reference, we express the voltage multiplication in terms of a Fourier series expansion. Here, we define our

Fourier expansion as

$$V(t) = \sum_{k=-\infty}^{\infty} c_n \, e^{i\frac{2\pi kt}{T}}, \tag{3.5}$$

where T is the period and c_n are the Fourier coefficients defined as

$$c_n = \frac{1}{T} \int_0^T V(t) \, e^{-i\frac{2\pi kt}{T}} \, dt. \tag{3.6}$$

By applying the Fourier series expansion, the DC component of the mixer output is

$$V_m = \frac{1}{V_0} \sum_{k=-K}^{K} c_k^s \, c_{-k}^r, \tag{3.7}$$

where c_k^s and c_{-k}^s are the Fourier components of the sample voltage and reference voltage respectively. We have a multiplicative factor V_0 which accounts for the amplifier circuit gain and total insertion loss and $K = f_{max}/f_0$ is the cutoff frequency set by the bandwidth of the electrical components f_{max} with f_0 as the laser repetition rate. We can see from Eq. 3.7 that we can maximize the output signal by setting the reference to have the same Fourier components as the pulsed signal. As expected, with a pulse train as the input signal, it is best to mix with a pulse train as a reference.

When measuring magnetic dynamics with TRANE, a time-varying magnetic or electrical field is applied across the ferromagnet. This induces an electrical current in the ferromagnetic wire, which creates a large background voltage across the wire. This background voltage needs to be removed because it reduces the dynamic range of our amplifiers and greatly reduces the signal to noise ratio. To remove this background voltage, we add a low-pass filter below the frequency of stimulation to remove this background voltage.

The bandwidth of the collection circuit does not affect the temporal resolution of TRANE. To show this, we assume without loss of generality the temperature gradient is constant at the laser spot and 0 everywhere else. With this

assumption, the time dependent ANE voltage V_{ANE} from the resistor model is given by

$$V_{ANE}(t) = \frac{\pi r^2}{w}(NM_s)\vec{\nabla}_z T(t)\, m_y(t). \tag{3.8}$$

Applying this Eq. 3.7, the measured voltage from the collection circuit can be expressed as

$$V_m = \frac{1}{V_0}\frac{\pi r^2}{w}(NM_s)\sum_{k=-K}^{K} c^r_{-k}\int_{-T/2}^{T/2} dt\left(e^{i2\pi kt/T}\right)\vec{\nabla}_z T(t)\, m_y(t), \tag{3.9}$$

The temperature gradient is non-zero only for a short time $\tau_{TRANE} \approx 10$ ps. Using the fact that $\tau_{TRANE} \ll 1/f_{max}$, which is true for the 1 GHz bandwidth circuit components, we can approximate the measured signal as

$$V_m \approx \left[\frac{1}{V_0}\frac{\pi r^2}{w}(NM_s)\sum_{k=-K}^{K} c^r_{-k}\right]\int_0^{\tau_{TRANE}} dt\,\vec{\nabla}_z T(t)\, m_y(t). \tag{3.10}$$

This shows that TRANE measures the magnetic moment over the time period of τ_{TRANE}. Therefore, the time resolution of TRANE is determined by the time decay of the temperature gradient τ_{TRANE} and it is not limited by the frequency bandwidth of the collection circuit.

3.3.3 Collection Circuit Transfer Coefficient

To determine the transfer coefficient of the collection circuit depicted in Fig. 1b and Fig. 3a in the main text, we measure the collection voltage from a calibration pulse. Numerical simulations suggests the voltage pulse from TRANE has a width of 10 ps. With the electronics available, we cannot create a 10 ps pulse to directly measure the transfer coefficient. Instead, we extrapolate it through measuring the gain of square pulses of wider widths. Fig. S6 shows the total gain in the collection circuit as a function of the square pulse width and the fit with our model.

We use Eq. 3.7 to model the gain where V_0 is the free parameter to fit the model. The pulse pattern generator signal into the mixer is treated as a periodic triangular function such that

$$V_{\mathrm{PPG}}(t) = \sum_n V^0_{\mathrm{PPG}}\,\mathrm{Tri}\left(\frac{t+nT}{\delta}\right), \tag{3.11}$$

where V^0_{PPG} is the peak voltage, δ is the rise and fall time, $f_0 = 1/T$ is the laser repetition rate and Tri is a triangular function given by

$$\mathrm{Tri}(x) = \begin{cases} 1-|x|, & \text{if } |x|<1 \\ 0, & \text{else} \end{cases}. \tag{3.12}$$

For all measurements, we set the pulse pattern generator to have a peak voltage of 800 mV and a rise and fall time of 800 ps. We can express this in terms of a Fourier series as

$$V_{\mathrm{PPG}}(t) = \sum_k V^0_{\mathrm{PPG}}\,(\delta\, f_0)\,\mathrm{sinc}^2\,(\pi\, f_0\, k\, \delta)\, e^{i(2\pi f_0 k t)}. \tag{3.13}$$

Similarly, we can express the calibrating square pulse train generated by the AWG as

$$V_{\mathrm{sq}}(t) = \sum_n V^0_{\mathrm{sq}}\,\mathrm{Sq}\left(\frac{t+nT}{\tau}\right), \tag{3.14}$$

where V^0_{sq} is the peak voltage, τ is the square wave width and Sq is a square pulse function given by

$$\mathrm{Sq}(x) = \begin{cases} 1, & \text{if } |x|<1/2 \\ 0, & \text{else} \end{cases}. \tag{3.15}$$

The square pulse train can be expressed in terms of the Fourier series as

$$V_{\mathrm{sq}}(t) = \sum_k V^0_{\mathrm{sq}}\,\,(f_0\,\tau)\,\mathrm{sinc}\,(\pi\, f_0\, k\, \tau)\, e^{i(2\pi f_0 k t)}. \tag{3.16}$$

The square pulse voltage is measured with a sampling oscilloscope to be 2.22 mV and the pulse width is varied from 150 ps to 1.5 ns.

With the two input signals, the DC component of the mixer output voltage is

$$V_m^{DC} = \left(\frac{V_{\text{sq}}^0 V_{\text{PPG}}^0}{V_0}\right)\left(f_0^2 \tau \delta\right) \sum_{k=-K}^{K} \text{sinc}\left(\pi f_0 k \tau\right) \text{sinc}^2\left(\pi f_0 k \delta\right). \tag{3.17}$$

The bandwidth of the amplifiers and mixer set the maximum frequency of the sum to $K = f_0/f_{\text{max}}$ where f_{max} is the maximum frequency bandwidth. For the measurements, the collection circuit bandwidth is limited to a maximum of $f_{\text{max}} = 1$ GHz and the laser repetition rate is $f_0 = 25.3$ MHz. By fitting Eq. 3.17 to the calibration measurement with V_0 as the only free parameter, we obtain a best fit of $V_0 = 0.41 \pm 0.04$ mV.

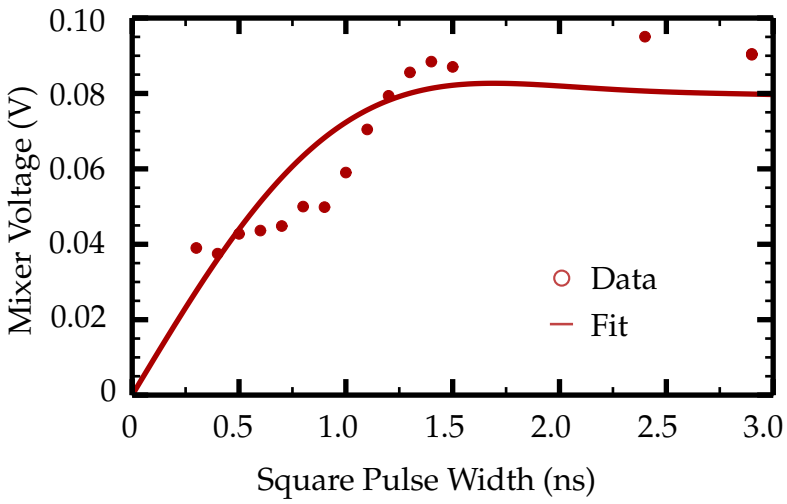

Figure 3.10: The mixer voltage as a function of the calibrating square pulse train width.

It is desirable to describe the total measured voltage in terms of the peak anomlaous Nernst voltage in terms of a collection circuit transfer coefficient. We define the transfer coefficient γ as

$$V_m^{DC} = \gamma \text{Max}\left[V_{ANE}(t)\right], \tag{3.18}$$

where γ is determined byby using the numerically simulated anomalous Nernst

voltage in section 8.6 and applying it to the calibration fit. Using the voltage multiplier coefficient from the fit in Fig. 3.10, our model estimates a transfer coefficient of 0.47 ± 0.04 for the numerically simulated pulse of approximately 10 ps in width.

3.4 MOKE

Our TRANE setup measures the heat transduced voltage by the laser and does not measure the reflected light at the sample. Therefore, when measuring magnetic moments with TRANE, it is possible to measure the time-resolved magneto-optical Kerr effect (TR-MOKE) simultaneously with TRANE. MOKE measures the change in the polarization of the reflected light, which is caused by the non-zero off-diagonal terms in the dielectric tensor inducing an asymmetry left and right circularly polarized light. The change in polarization is proportional to $\vec{k} \cdot \vec{M}$, where $\vec{k}$ is the propagation direction of the light and $\vec{M}$ is the magnetic moment [27]. Therefore, depending on the angle of incidence, MOKE can measure the magnetic moment projection in different directions. The two different types of MOKE we discuss are polar MOKE, which measures the out-of-plane magnetic moment with an incident light perpendicular to the surface, and longitudinal MOKE, which measures the in-plane magnetic moment with an incident light at an angle to the surface.

3.4.1 Polar MOKE

Time-resolved polar-MOKE with a microscope objective has been shown to be capable of measuring out-of-plane magnetic moments with sub-micron resolution [87, 88, 89]. To measure transverse MOKE simultaneously with TRANE, we need to measure the change in polarization due to the sample. The optical setup to measure both polar MOKE and TRANE is depicted in Fig. 3.11. Adding a half-wave plate and polarizing beam splitter allows us to measure the change in polarization. The half-wave plate and the polarizing beam splitter are aligned such that for a non-magnetic metal sample, the two beams out of the polarizing beam splitter have equal intensity. Therefore, using two photodiodes to measure the intensity of both beams, the difference in current provides a measure of the polarization change.

We use our setup to measure polar MOKE, where Fig. 3.12 shows the results the hysteresis and a 2D scan of a perpendicular magnetic anisotropy (PMA) Co/Ni multilayer structure grown on a 120 nm of Au seed layer [90]. This film was sputter deposited with the 3-gun sputter chamber from the Cornell Center of Materials Research (CCMR). The multilayer of Co/Ni was grown with Co layer of 0.2 nm thickness and the Ni layer of 0.6 nm thickness and repeated for 5 total multilayers. These results show that our setup is capable of measure polar MOKE, and with the 2D scan we can clearly image magnetic domains.

3.4.2 Longitudinal MOKE

Due to the direction of the light wavevector needed for longitudinal MOKE, it is more difficult to measure high resolution longitudinal MOKE compared to

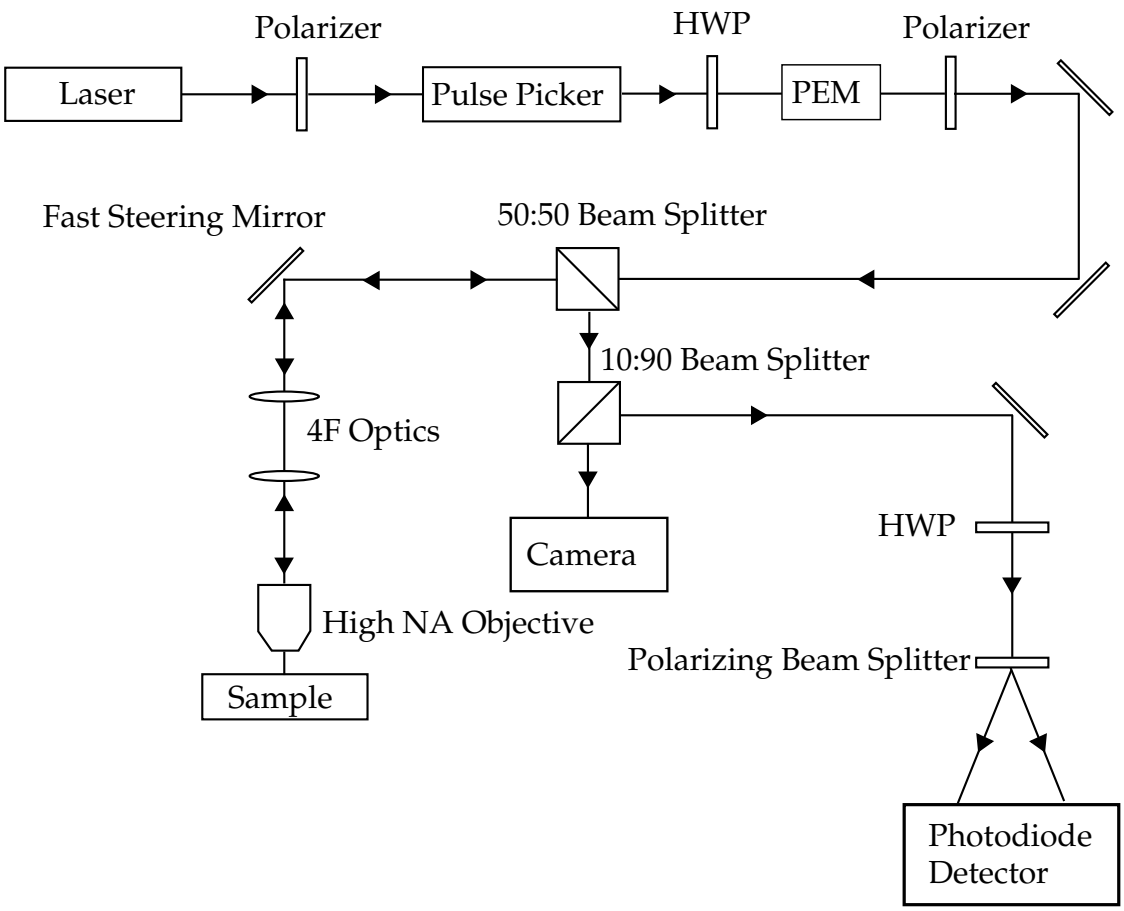

Figure 3.11: The optical setup to measure both polar MOKE and TRANE.

polar MOKE. Since a microscope objective to focus the light must be aligned normal to the smaple surface, portions of the laser beam profile must be analyzed to measure longitudinal MOKE [91]. To measure longitudinal MOKE with high spatial resolution, we begin with the same setup as the transverse MOKE as previously described and introduce a slit to measure a portion of the reflected light as depicted in Fig. 3.13. Fig. 3.13 shows that the slit removes a portion of the beam profile, thus the light that is detected has an overall non-zero k_x component at the interface with the sample. This overall k_x component will measure the x-component of the magnetic moment. It is also possible to measure longitudinal MOKE by asymmetrically filling the back aperture of the

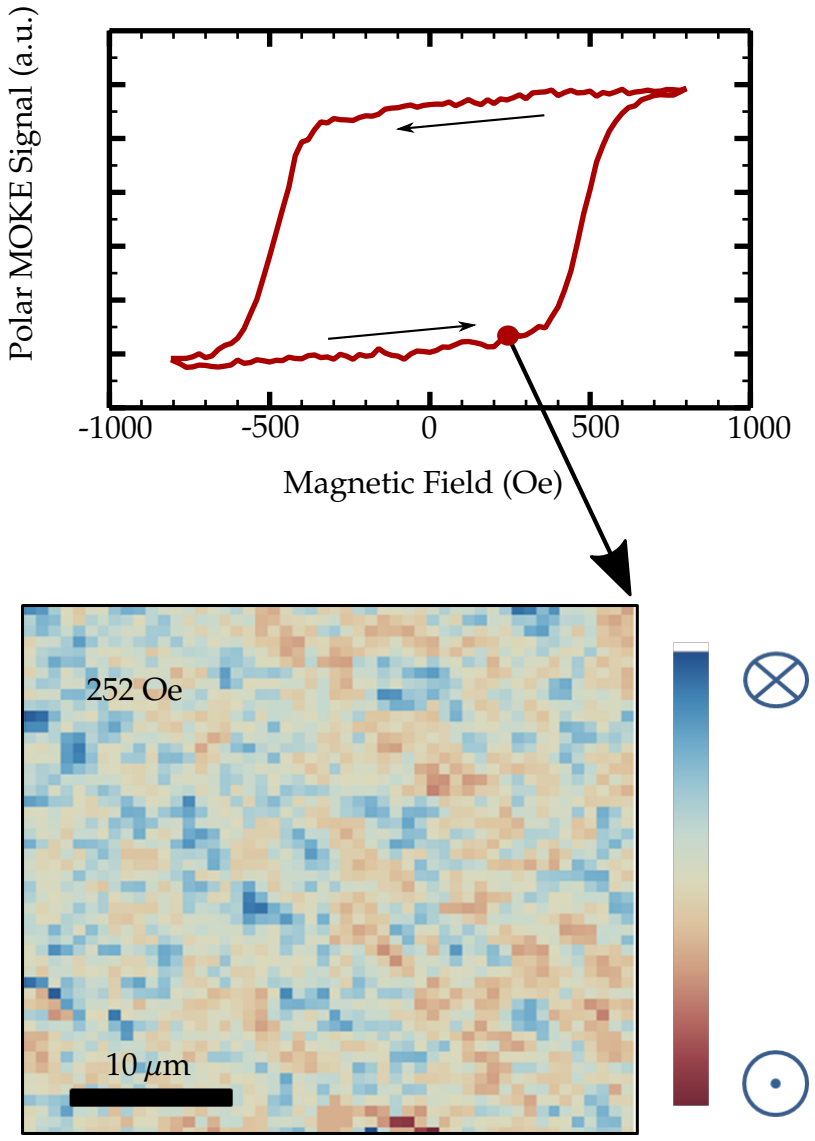

Figure 3.12: The hysteresis measurement and 2D scan with polar MOKE of a PMA Co/Ni bilayer structure.

objective, but this reduces the spatial resolution. The slit method for measuring longitudinal MOKE has poor signal to noise relative to asymmetrically filling the back aperture but produces the best spatial resolution.

Figure 3.14 shows the results of cutting the beam to measure high resolution longitudinal MOKE of a 70 nm cobalt hourglass pattern. Using the setup, we

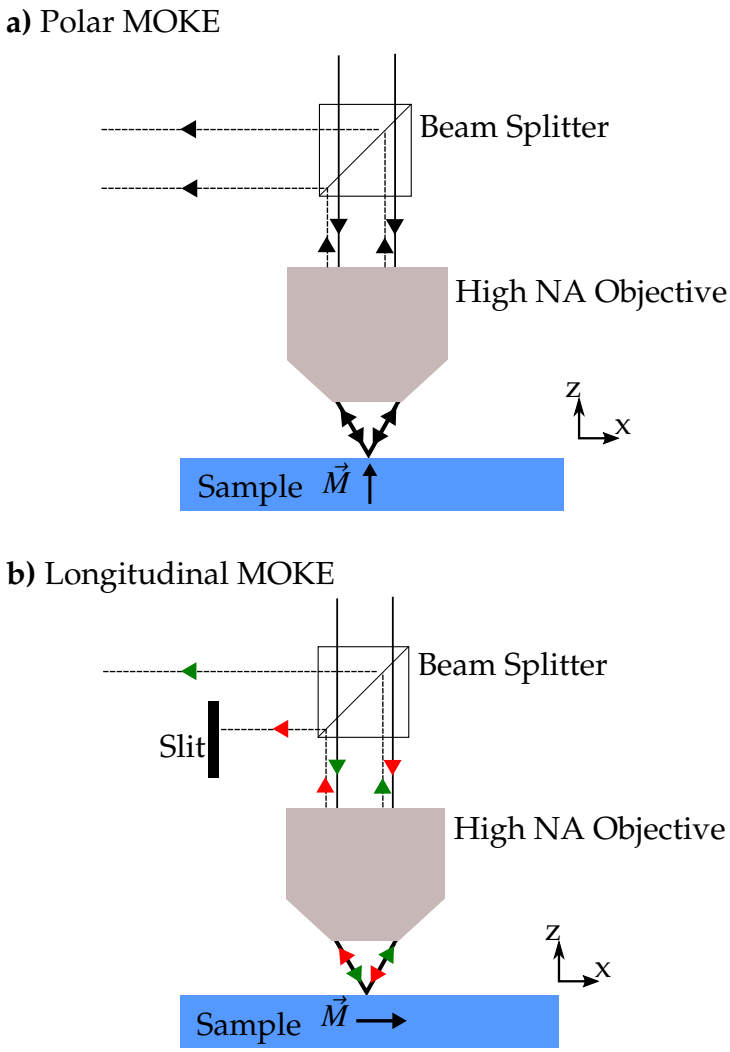

Figure 3.13: The experimental setup to measure high spatial resolution MOKE with a high NA objective.

measure the magnetic hysteresis and with a 2D scan show magnetic domains. A major disadvantage with MOKE are measurement artifacts at the edge, as shown in Fig. 3.14c, which is caused by the reflected light at the patterned edge returning at unpredictable angles. This issue is exacerbated when measuring features that are approximately the same size as the focused laser spot size. We will show that these edge artifacts are not present with TRANE since TRANE measures the induced electric signal and not the reflected light. Fig. 3.14d shows

that longitudinal MOKE is highly dependent on the focus by measuring the multiple hysteresis loops, where after each loop we run the autofocus program. There is a varying offset which is due to the small variation in the autofocus causing a different portion of the beam profile to be cut. Therefore, this longitudinal MOKE technique is much more dependent on the focus compared to the TRANE.

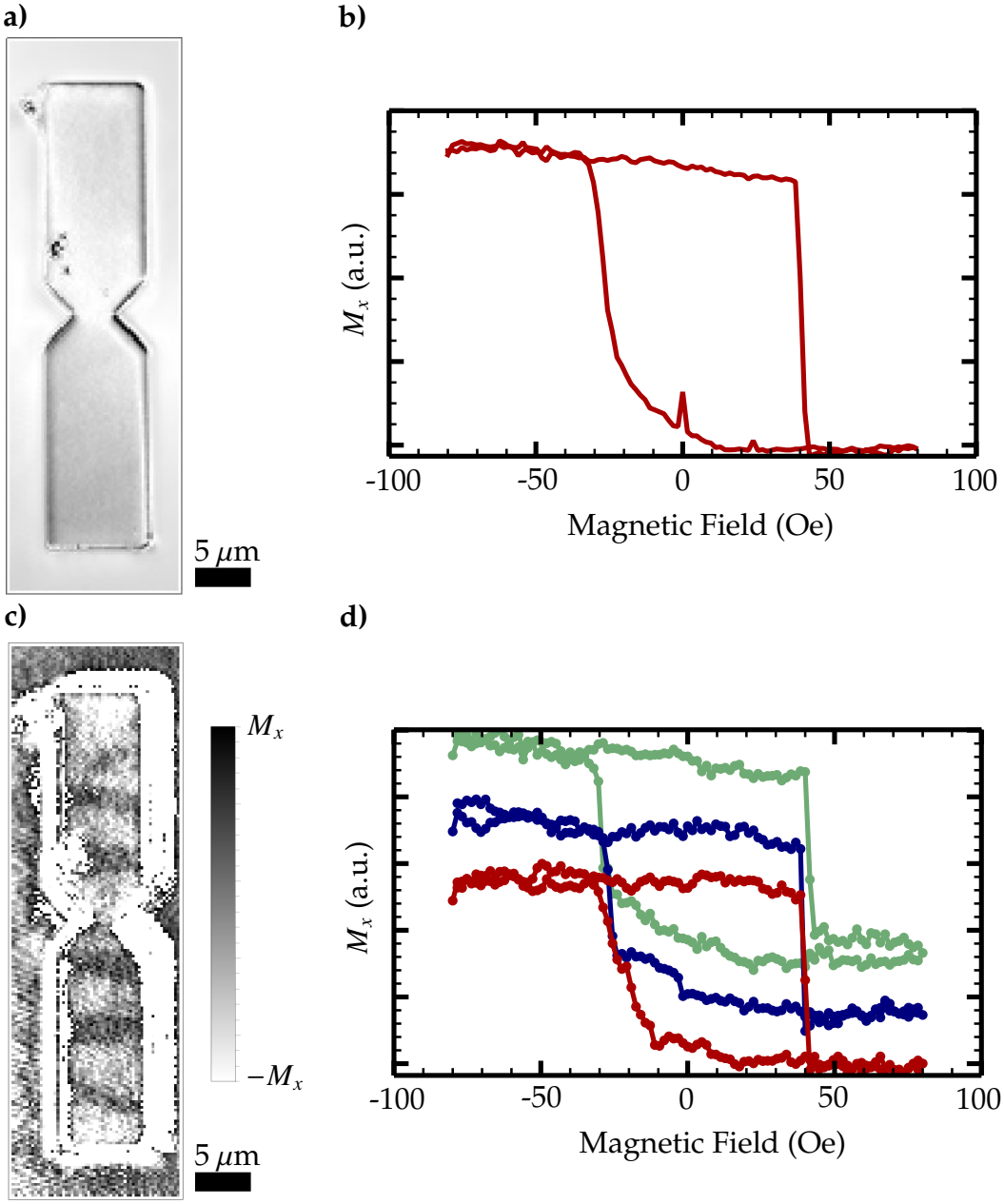

Figure 3.14: Using longitudinal MOKE to measure the in-plane magnetic moment of a 70 nm cobalt hourglass pattern. a) the micrograph of the Co hourglass pattern. b) Longitudinal MOKE measurement of the in-plane magnetic moment at an interior point of the hourglass pattern. c) Longitudinal MOKE 2D spatial scan at 12 G. d) Multiple field scans after running the autofocus program.

CHAPTER 4

FABRICATION

For this chapter, we will discuss the fabrication process to create the devices that are measured with TRANE. The sample must meet two requirements to be measurable with TRANE. First, the magnetic material under study must be accessible to create a temperature gradient. Secondly, there must be electrical contacts to measure the anomalous Nernst voltage. Due to the nature of the TRANE measurement, to fabricate our devices, we can separate the process into two sections: the magnetic pattern and the electrical contacts. We illustrate the fabrication process in Fig. 4.1. The entire fabrication process was performed in the Cornell NanoScale Science and Technology Facility (CNF) with the exception of the sputtered Permalloy (Py) films which were deposited with the LESKER sputter system from CCMR, which is managed by the Ralph group, and etching the magnetic films with the AJA ion mill from the Buhrman group. This fabrication procedure was originally designed for single layer ferromagnet devices, but it is applicable for multilayer systems.

For all the measurements presented, the samples were fabricated on sapphire substrates. There are two main properties that makes sapphire the ideal substrate for TRANE measurements. First, it is electrically insulating with a large bandgap of 8.7 eV [92]. Therefore, the voltage measured is only due to the electric fields generated in the magnetic material. The large bandgap also results in high transmittance of the laser, since the laser at 800 nm has a much lower photon energy at 1.55 eV. A high transmittance is important because it will not heat the substrate, which results in a larger thermal gradient in the magnetic material. Secondly, it has good thermal conductivity at 27 $\mathrm{W/m\,K}$,

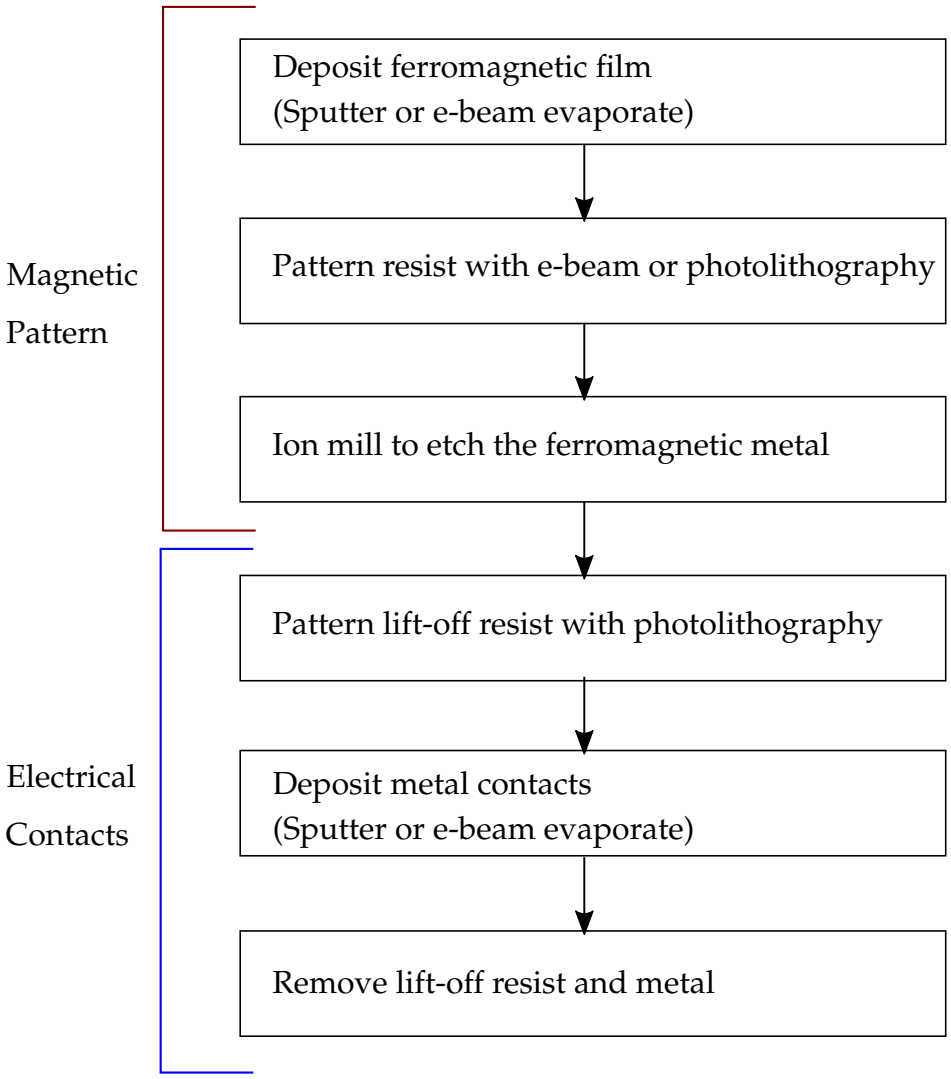

Figure 4.1: An overview of the fabrication process used to create samples to measure in with TRANE.

comparable with relatively resistive metals such as lead at 34 W/m K and much higher than typical insulators, therefore it acts as a good heat bath [93].

4.1 Magnetic Pattern

4.1.1 Film Deposition

We employ two different methods to deposit magnetic films, each with their advantages. To deposit the permalloy (Py) films, we use magnetron sputter deposition. The cobalt (Co) films are deposited with e-beam evaporation. For either magnetic film we also deposit a 3 nm layer of aluminum as a capping layer, without breaking the vacuum. The aluminum capping layer prevents the oxidation of the magnetic film. When exposed to the oxygen in the atmosphere, the aluminum forms a native oxide layer approximately 2 nm thick [94], which we consider as negligible when measuring TRANE.

Cobalt was deposited with an e-beam evaporator in the CNF. The e-beam evaporator deposits the film in a vacuum using an electron beam to heat the source material above the boiling point, which causes the cobalt to collect on the substrate creating the deposited film. During the process, the cobalt will spit, resulting in large number of defects present in the film. Though defects are typically not preferable in the fabrication process, these defects act as magnetic nucleation sites and results in a magnetic field required for switching at approximately 30 Oe, which is greatly reduced compared to the switching field for sputtered cobalt films of approximately 300 Oe. This reduction in switching field results in a lower magnetic field required to study the magnetization which is helpful when measuring high spatial resolution TRANE due to the interaction of the high resolution objective with the magnetic field as discussed in Sec. 3.1.3. Permalloy thin films are deposited with a LESKER magnetron sputter system. In the magnetron sputtering process, an Argon plasma is con-

fined at the source, which sputters off and deposits on the substrate. Sputtering depots films of higher quality with better film smoothness and grain structure compared to evaporator grown films.

4.1.2 Patterning Magnetic Devices

Electron Beam Lithography

The Py devices that we measure with TRANE were patterned with electron beam (e-beam) lithography with the JEOL 9500 in the CNF. E-beam lithography uses high energy electrons to interact with the resist to change its solubility in the developer. The high energy electrons allow for higher resolution than photolithography, as set by the diffraction limit, thus allowing us to pattern features down to 20 nm.

For e-beam, we use a tri-layer resist developed by the Buhrman group [95]. The tri-layer resist consists of Omnicoat, PMMA (495PMMA A4) and 6% HSQ. The first layer consisting of Omnicoat was spin coated at 1500 rpm for 30 s and baked at 170°C for 1 minute. This spin coating process for Omnicoat was repeated to obtain the optimal thickness. The second layer is PMMA, which is spin coated at 4000 rpm for 60 s and baked at 170°C for 1 minute. The third layer is HSQ, also spin coated at 4000 rpm for 60 s and baked at 170°C for 1 minute.

This tri-layer resist was designed for etching in the ion-mill. With the ion mill, the top HSQ layer reacts with the plasma, which hardens and has a slow etch rate, making it a good etch mask. By using the Omnicoat as the underlayer,

the entire resist stack can be removed easily with acetone after the ion-mill etch despite HSQ hardening. The PMMA layer acts as an adhesion layer between the HSQ and the omnicoat.

With the sapphire substrate, there can be issues with e-beam lithography involving charge build-up. For the samples currently fabricated, the presence of the metal ferromagnetic film has alleviated issues with charge build-up. This has been true for films of 5 nm in thickness and above. Issues with charging may arise when trying to pattern smaller feature sizes or when patterning thinner films. To alleviate this possible problem, a conducting polymer such as PSSA may be used.

After the resist pattern is exposed, the HSQ layer is developed in MIF726 for 2 minutes. Note that the PMMA and Omnicoat layers are not removed by the developer. To remove the underlying PMMA and Omnicoat layers, we plasma etch with O_2 in the Oxford etcher with conditions of 100 W, 50 mTorr and 20 sccm for 90 seconds. To determine if the resist was correctly patterned, we use optical microscopes and scanning electron microscopes (SEM). Due to the insulating sapphire substrate, high resolution images cannot be obtained with SEM due to charge build-up.

Photolithography

To pattern large magnetic devices (for the Co sample), we used a GCA 5x g-line (436 nm) stepper. We use a positive photoresist (Shipley 1813), which reacts with the g-line light to make it soluble to the photoresist developer. To increase adhesion of the photoresist, we coat the wafer with a pre-wetting agent, p20

primer, and wait for 10 seconds, followed by spin drying for 30 seconds at 3000 rpm. Following the pre-wetting, we apply the S1813 photoresist by spin coating at 3000 rpm for 30 seconds and baking at 90°C for 1 minute. After exposing the photoresist with the 5x stepper, we develop it in MIF726 for 1 minute, followed by a DI water rinse. The optimal photolithography exposure can be determined by observing the various exposure times in an optical microscope.

4.1.3 Ion Milling Etching

We etch the ferromagnetic film with an AJA ion mill. Similar to sputter deposition, an argon plasma is used to etch the target material. The ion-mill includes an end-point detection, where a mass spectrometer measures the etched atoms to determine when the magnetic film is removed. For these samples, we ion mill at a 45° incident angle and set a discharge voltage of 40 V and current of 0.5 A. After etching, the remaining resist is removed with acetone.

4.2 Electrical Contacts

4.2.1 Resist for Lift-off

To pattern the leads for electrical connection to the ferromagnetic wire, we use a lift-off process since etching will damage the ferromagnetic material. The electrical contacts are patterned with optical lithography with a sacrificial layer of LOR to provide the desired undercut profile. Before applying the LOR, we first bake the wafer at 180°C to remove any solvents. The LOR has a very high vis-

cosity relative to typical photoresists, therefore to uniformly coat the wafer we dispensed the LOR resist onto the wafer while it is spinning. We dispense the LOR is set at 500 rpm with a ramp rate of 75 rpm/s for 10 s, followed by increasing the spin rate to 5000 rpm with a ramp rate of 4000 rpm/s for 30 s to properly coat the wafer. After spinning the resist, we bake the LOR at 180^oC for a minimum of 5 minutes. The pre-exposure bake time for LOR is important for controlling the solubility of LOR and thus controlling the undercut profile, where increasing the bake time decreases the solubility of LOR in developer. When patterning small features, we need to reduce the LOR solubility or the entire undercut profile may fully dissolve and remove the pattern. On top of the LOR, we apply S1813, which is statically dispensed and is spin coated at 3000 rpm with a ramp rate of 1000 rpm/s for 30 s. This is followed with a pre-exposure bake at 90°C for 1 minute.

4.2.2 Photolithography Exposure

Due to the different reflection coefficient between the ferromagnetic metal and sapphire substrate, the optimal exposure time is different for the two regions. This causes the patterned features to be smaller where it overlays on the ferromagnetic metal as shown in Fig. 4.2. Since the leads were 1 um apart at the closest, we could not optimally expose for the region over the ferromagnet since it would increase the size of the contacts and may lead to shorting in the region over the sapphire. This difference in exposure time could possibly be alleviated by using an anti-reflective coating.

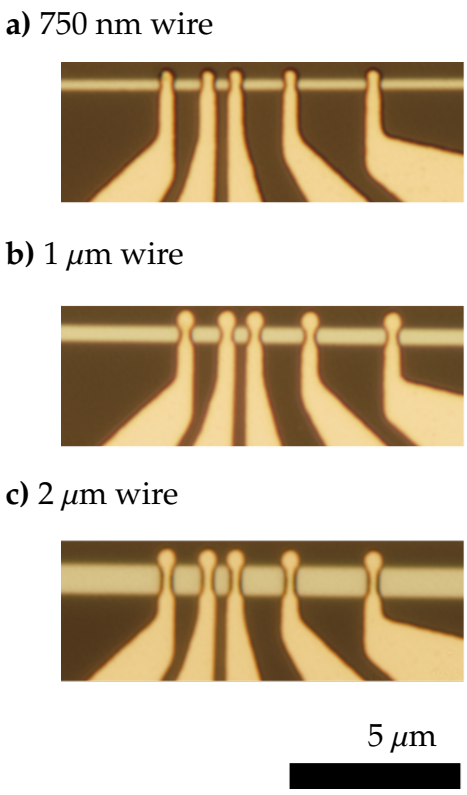

Figure 4.2: The photoresist pattern difference due to the different reflectivity between the magnetic material and the sapphire causes the regions to be exposed differently.

4.2.3 Contact Pad Deposition

We deposit the contact pads consisting of Ti(20 nm)/Cu(80 nm). The titanium layer acts as an adhesion layer because it forms an oxide at the boundary with the sapphire. The 20 nm thickness of titanium is required for optimum adhesion [96]. Previous iterations of the process with 5 nm thick titanium adhesion layers resulted contact pads peeling off during the wire bonding process. Other common adhesion layers such as chromium were avoided due to its antiferromagnetic behavior. The thickness of the copper layer was chosen to create a 50 Ω impedance with the stimulation wire. Copper was chosen due to its high

conductivity and negligible spin Hall effect. As an initial proof of concept, a negligible spin Hall effect was desired to remove other possible variables. Currently in progress, we are able to measure TRANE with gold and platinum contact pads without any issues. Gold is an ideal material for the contact pads due to its inertness and softness which is ideal for wire bonding. Platinum due to its stiffness along with the sapphire wafer produces a very stiff surface at the contact pads, which requires high ultrasonic power for wire bonding.

Evaporators are typically ideal for depositing thin films for lift-off due to the highly directional deposition. The issue with depositing the film with the evaporator in our process is that it does not allow us to descum the resist before deposition. A descum process is typically performed with an oxygen plasma to remove residual resist. For the current process, we cannot descum with an oxygen plasma because it oxidizes the ferromagnet. For several test samples, the contact resistance between the contact pads and the magnetic material was unusually high, possibly caused by the residual resist.

To work around the issue with residual resist, we use sputter deposition instead of an evaporator. The CVC sputter deposition system in the CNF has an ion mill that allows us to ion mill and deposit the film without breaking the vacuum. This has the added benefit of the opportunity to remove the native oxide layer of the aluminum capping layer for better electrical contact. We calibrate the ion mill to etch the native oxide layer, by measuring the profile height of an aluminum layer deposited on thermally oxidized silicon wafer after specific etch times. The silicon oxide, aluminum oxide and aluminum all have different etch rates with the ion mill. It is expected that the etch rates in increasing order to be aluminum oxide, silicon oxide and aluminum [97]. Therefore, the

etch time corresponding to the maximum height will be the optimal etch time for removing the native oxide layer. Fig. 4.3 shows the height of the profile as a function of the ion mill etch time, showing a 3 minute optimal etch time.

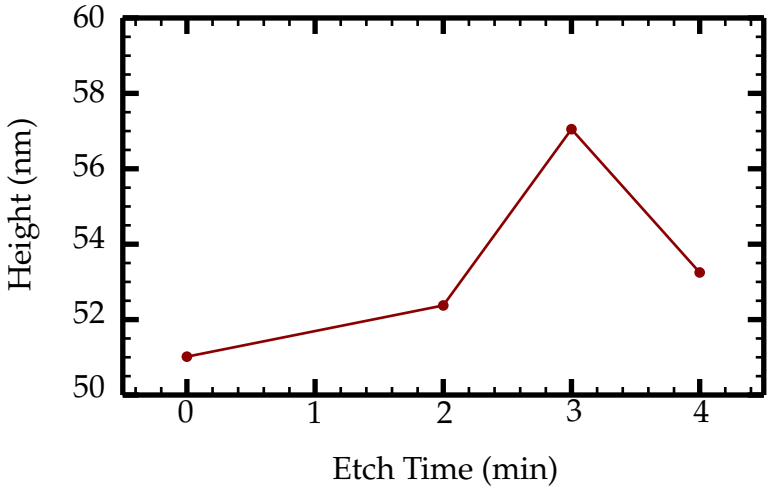

Figure 4.3: Ion mill calibration measuring the sample height of aluminum grown on thermally oxidized silicon wafer as a function of etch time. The maximum height corresponds to the optimal time to remove the native aluminum oxide.

Finally, with the film deposited, we remove the liftoff resist with 1165 remover at 70°C. The final devices of the Co crosses with 18 μm wide arms and Py wires of 2 μm wide are shown in Fig. 4.4.

4.3 SEM Imaging

We use an SEM for detailed characterization of the final device. Due to the insulating sapphire substrate, we deposit a conducting layer of gold/palladium of approximately 10 nm to prevent charge build-up. The gold/palladium layer is deposited in a sputter chamber that is evacuated with a roughing pump down

to approximately 10^{-3} Torr. Fig. 4.5 shows the SEM image of the 2 μm wide Py wire which we measure with TRANE.

a) 18 μm Co Cross

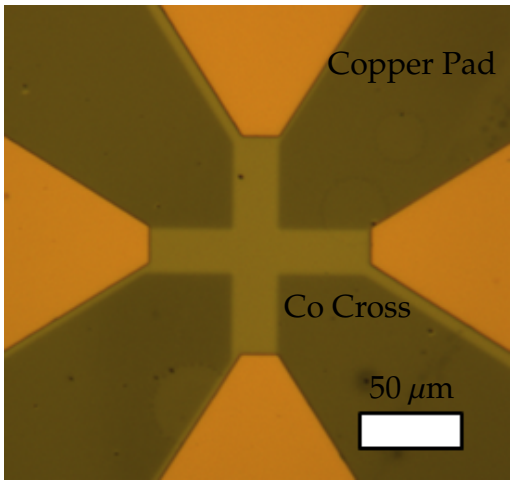

b) 2 μm Py Wire

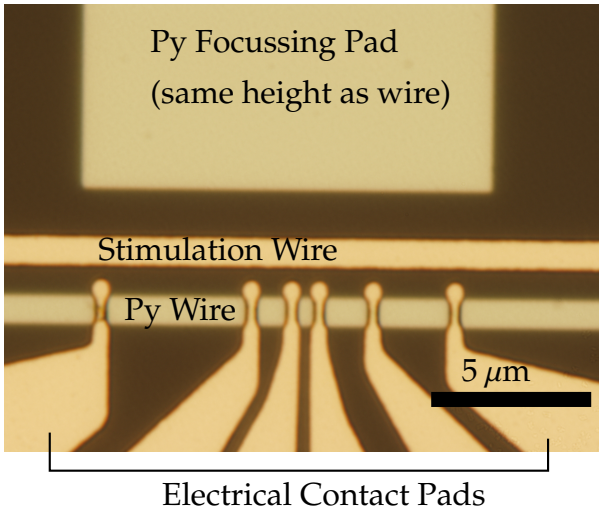

Figure 4.4: Optical microscope images of the 18 μm Co cross device and 2 μm Py wire device.

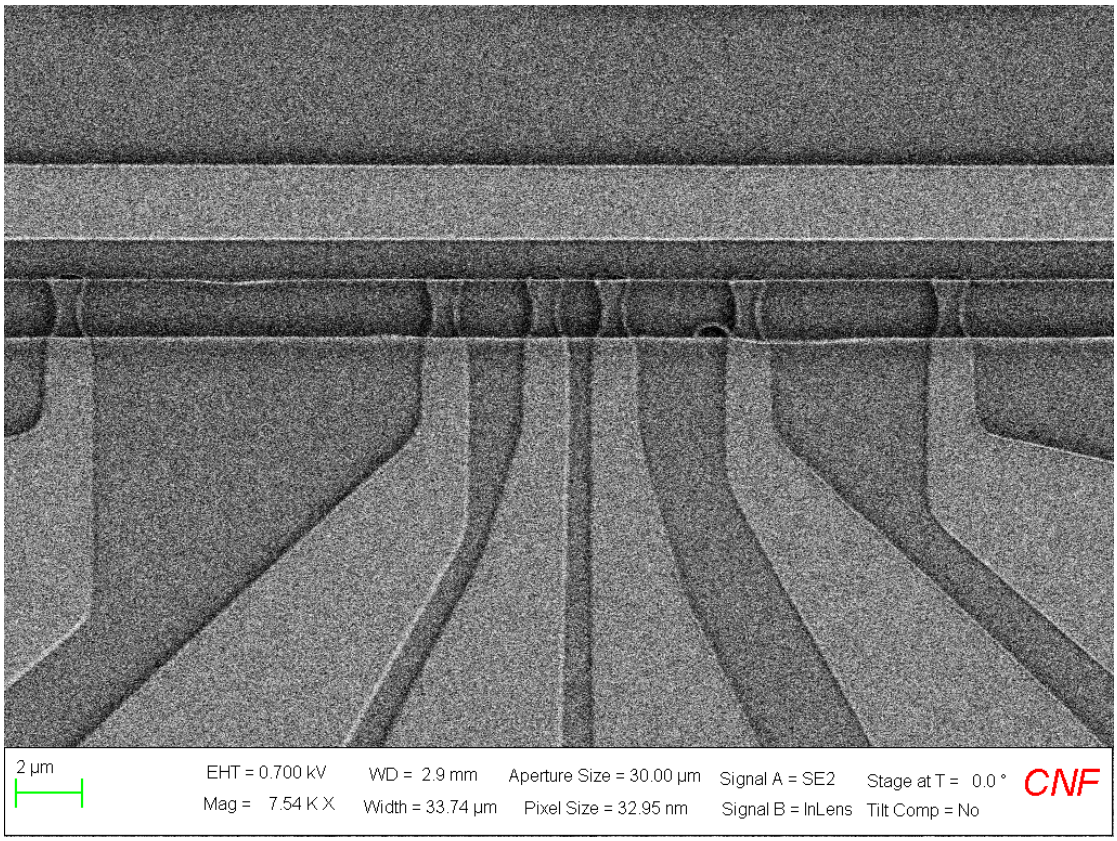

Figure 4.5: SEM image of the Py 2 μm device to be measured with TRANE.

CHAPTER 5

TRANE MEASUREMENT OF STATIC MAGNETIZATION

In this chapter, we discuss the capabilities of TRANE to measure the spatial variations in the magnetic moment. Using a microscope objective, we create a focused laser spot on the sample surface of approximately 310 nm in Gaussian width (730 nm FWHM), which generates the spatially localized temperature gradient to measure the magnetic moment with TRANE. We image the magnetization by scanning the focused laser across the sample with the FSM. With these measurements, we determine the spatial resolution of TRANE to be set by the thermal spot size and also explore avenues to achieving sub-diffraction spatial resolution.

5.1 Magnetic Switching and Hysteresis

To demonstrate the spatial measurements of TRANE, we study a Co cross shown in Fig. 5.1, where each arm of the cross is 18 μm in width. As shown in Fig. 5.1, we connect to the top and bottom contacts to measure the anomalous Nernst voltage, which is proportional to the magnetic moment projection in the x-direction. We manipulate the magnetic moment of the cross structure by applying an external magnetic field in the x-direction. With a large the external magnetic field, the magnetization is saturated and aligned with the external field. We can switch the magnetization with a large external field in the opposite direction.

To show that TRANE is capable of properly measuring the magnetic mo-

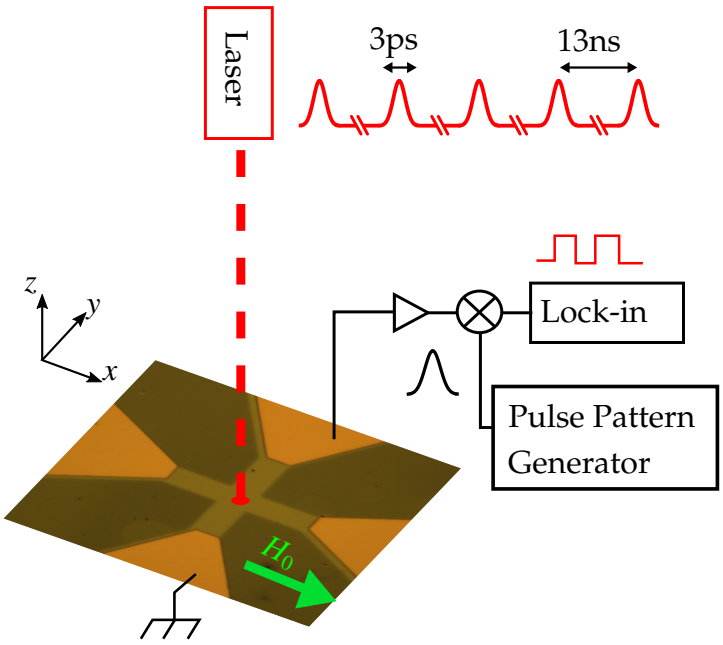

Figure 5.1: The TRANE setup to measure magnetic switching and hysteresis in the Co cross.

ment, we fix the laser spot at the center of the cross and measure the TRANE signal as a function of the applied magnetic field. We obtain Fig. 5.2 by measuring V_{TRANE} and the longitudinal MOKE signal by sweeping the applied field to go from a large negative field, to a large positive field and back. By comparing the TRANE signal and the MOKE signal, the magnetic switching occurs at the same field, which shows that TRANE is capable of measuring the magnetic moment precisely. It is clear that for this sample, under the same conditions, the TRANE signal has a much higher signal to noise ratio than longitudinal MOKE. Also, note that V_{TRANE} is centered about zero and the switching of the magnetic moment causes the sign of the signal to change. Therefore, unlike MOKE, we have a measure of the magnetic moment projection about zero and not a relative signal to an arbitrary value when measuring MOKE with photodiodes.

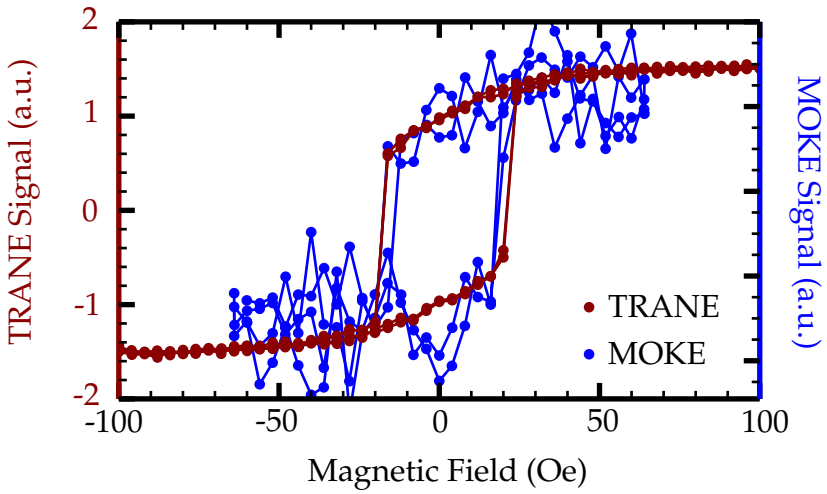

Figure 5.2: The magnetic switching of the Co cross.

We note that when the applied magnetic field is greater than the saturating field, V_{TRANE} is constant within the experimental noise. This suggests the voltage from the ordinary Nernst effect is much less than the anomalous Nernst effect. Therefore, we assume for all our TRANE measurements, the ordinary Nernst effect can be neglected and the signal is due to the anomalous Nernst effect. We do not do a direct comparison of the two contributions due to the difficultly involved in obtaining a precise measurement of the ordinary Nernst effect since it requires a large magnetic field.

5.2 TRANE Sensitivity

The sensitivity of the TRANE measurement is determined from the relative noise level to the overall signal size at magnetic saturation using hysteresis measurements as shown in Fig. 5.2. In the measurement geometry, the satu-

rated moment is perpendicular to the TRANE voltage so that ($V_{TRANE}^{max} - V_{TRANE}^{min}$) corresponds to a 180^o rotation. The TRANE voltage, V_{TRANE}, is related to the magnetization angle, θ, with respect to the x-axis given by

$$V_{TRANE} = \eta \cos(\theta), \tag{5.1}$$

where η is a proportionality constant, dependent on the sample and electronic collection circuits. The angular sensitivity, $\delta\theta$ is dependent on the signal noise level, δV_{TRANE}, through the error propagation such that

$$\delta\theta = \left|\frac{\partial V_{TRANE}}{\partial \theta}\right|^{-1} \delta V_{TRANE}. \tag{5.2}$$

As a longer sampling time will reduce the value of δV_{TRANE} regardless of the sample, it is desirable to have a sensitivity figure of merit independent of the sampling time. Thus, the signal-to-noise ratio must be scaled to account for the measurement rate, in the case of a lock-in measurement this is the time constant. The TRANE signal noise level is related to the lock-in time constant, T_c and the standard deviation σ_V by [98]

$$\delta V_{TRANE} = \sigma_V \sqrt{T_C}. \tag{5.3}$$

This yields an equation for the angular sensitivity of

$$\delta\theta = |\eta \sin(\theta)|^{-1} \sigma_V \sqrt{T_C}. \tag{5.4}$$

We determine the standard deviation of V_{TRANE} at saturation, σ_V^{sat}, which occurs at $\theta = 90^o$. Therefore, the angular sensitivity of TRANE can be determined by

$$\delta\theta_{min} = \frac{\sigma_V^{sat}}{(V_{TRANE}^{max} - V_{TRANE}^{min})/2} \sqrt{T_C}. \tag{5.5}$$

We apply this calculation to measure the TRANE angular sensitivity of Co crosses of two different widths as depicted in Fig. 5.3, where we find that

$\delta\theta_{min} = 4.6^{o}/\sqrt{\text{Hz}}$ for the 52 μm cross and $\delta\theta_{min} = 0.73^{o}/\sqrt{\text{Hz}}$ for the 18 μm cross. This result shows that the magnetic moment angular sensitivity of TRANE is highly dependent on the sample. As discussed in Sec. 2.4, the total TRANE voltage will depend on the overall sample width due to the effective resistance shunting, with a scaling of d^2/w, the TRANE voltage increases as the sample width decreases. Therefore, to achieve the greatest angular sensitivity with TRANE, we must use a heat spot of approximately the same width as the sample.

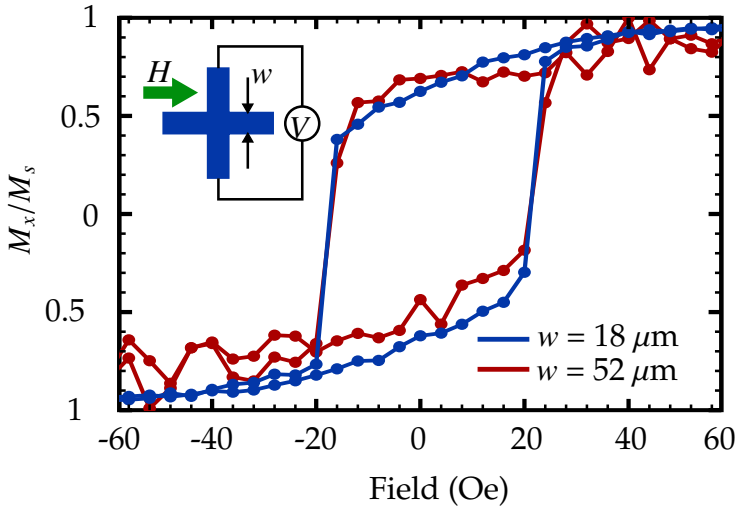

Figure 5.3: In this graph we plot TRANE measured hysteresis loops for two different cross sizes. We observe that the sensitivity is $\theta_{min} = 4.6^{o}/\sqrt{\text{Hz}}$ for the 52 μm cross and $\theta_{min} = 0.73^{o}/\sqrt{\text{Hz}}$ for the 18 μm wide cross.

5.3 Two Dimensional Scans

Next, we experimentally demonstrate that TRANE is capable of measuring the spatial variation in the magnetic moment by scanning the laser across the Co

cross. We prepare the magnetic moment configuration for mapping by starting at a large negative applied field to saturate the magnetization, then set the applied field to 32 Oe, where we will measure the spatial dependence of the magnetic moment. Fig. 5.4a shows the magnetic moment projection in the x-direction from scanning the laser across the sample. The image in Fig. 5.4 shows multiple mangetic domains which is the result of the shape anisotropy created from the cross structure. The saturating magnetic field for the cross along the length of the x-axis is lower than the saturating field in the cross arms that align along the y-axis. Using TRANE, we can see that at a field of 32 Oe, the magnetic moment along the length of the cross is in the opposite direction compared to the vertical arms.

We show the vertical and horizontal line cuts of the TRANE 2D scan in Fig. 5.4b and c. By taking the line cut across the domains, we can clearly see that the two domains are separated by a domain wall where the TRANE signal is zero, due to the zero magnetic moment along the x-axis projection. In Fig. 5.4c, the TRANE signal is zero when measuring off the sample and there are no edge artifacts unlike MOKE where the edge artifacts are prominent as shown in Fig. 3.14. Therefore, due to the lack of edge artifacts and the $1/w$ scaling of the signal, TRANE is much more suitable for measuring much smaller features compared to MOKE.

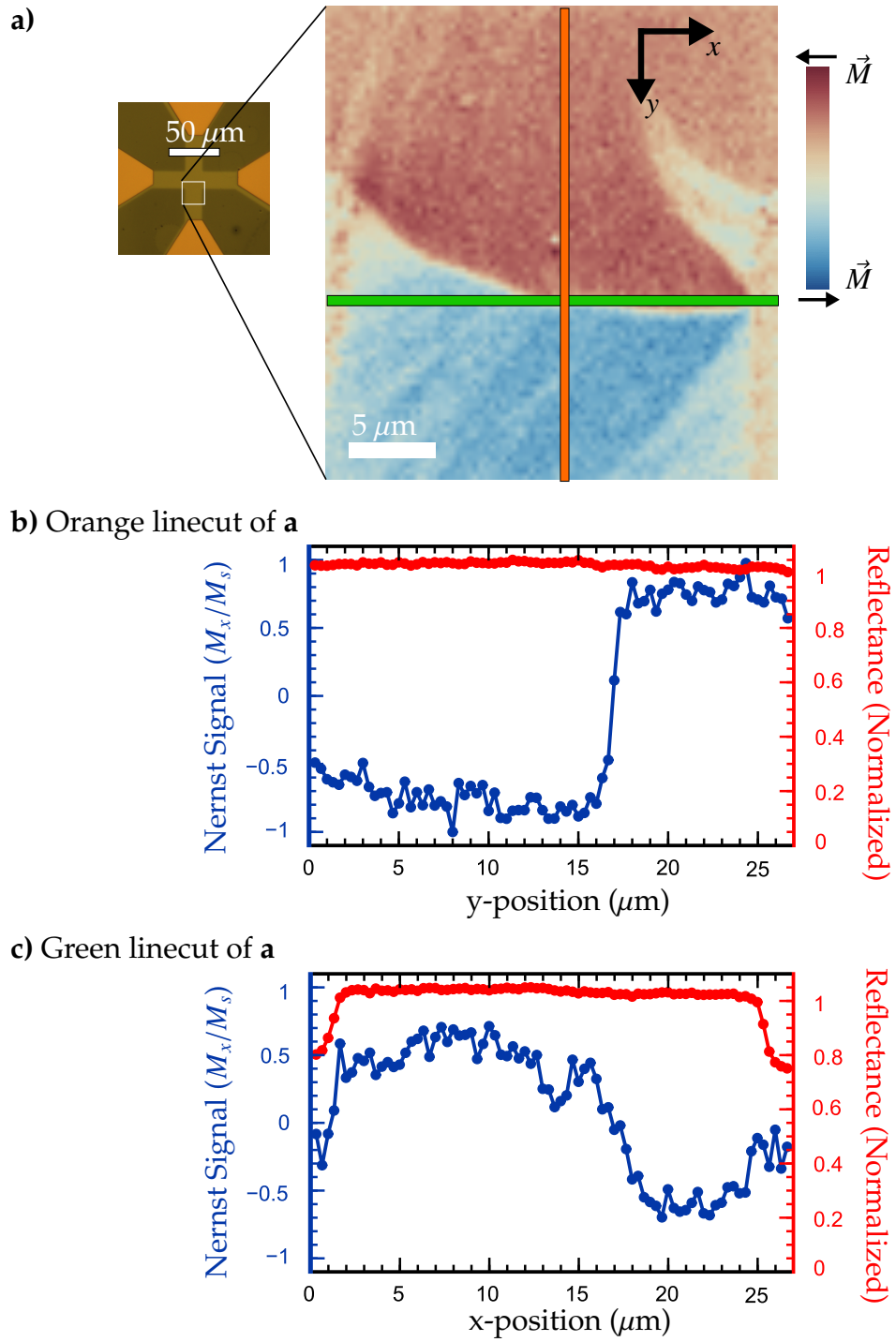

Figure 5.4: 2D TRANE measurement of a 18 μ wide Co cross. **a)** 2D TRANE measurement of the magnetic moment x-projection. **b)** The vertical linecut of the 2D TRANE measurement. **c)** The horizontal linecut of the 2D TRANE measurement.

5.4 Spatial Resolution

We determine the spatial resolution of TRANE from a line cut of the spatial 2D scan across a portion of the domain wall in Fig. 5.4. For the cobalt films studied here, the domain walls are 150-200 nm wide [99], which is far below the 730 nm FWHM (310 nm Gaussian width) of the laser spot we measured for our apparatus. We use this fact to evaluate the resolution of our TRANE microscope by fitting spatial line cuts (Fig. 5.4) across a magnetic domain wall with the convolution of a step function and a Gaussian function of width, δ.

To model the line cut of the domain wall, we assume the temperature gradient profile has a Guassian profile in the lateral dimensions. Thus, the profile of the domain wall can be fit to the convolution of a Gaussian and step function given by

$$V_{TRANE}(y) = Ae^{(y-y_0/2y_{res})^2} \otimes (2H(y) - 1), \tag{5.6}$$

where A is the amplitude, y_0 is the center position, y_{res} is the Gaussian width and H is the Heaviside step function. The Gaussian width is taken to be the spatial resolution of TRANE. We determine the fit with a least means squared method to with Gaussian width, amplitude and center position as free variables. We apply this method for the 4 μm region of the domain wall as shown boxed in Fig. 5.5a. This region was chosen because it was the portion of the image with the clearest step function behavior. The results of the individual fits are shown in Fig. 5.5b. The mean of the Gaussian width is 325 nm with a standard deviation of 70 nm, suggesting that the spatial resolution of TRANE is limited by the size of the heat spot.

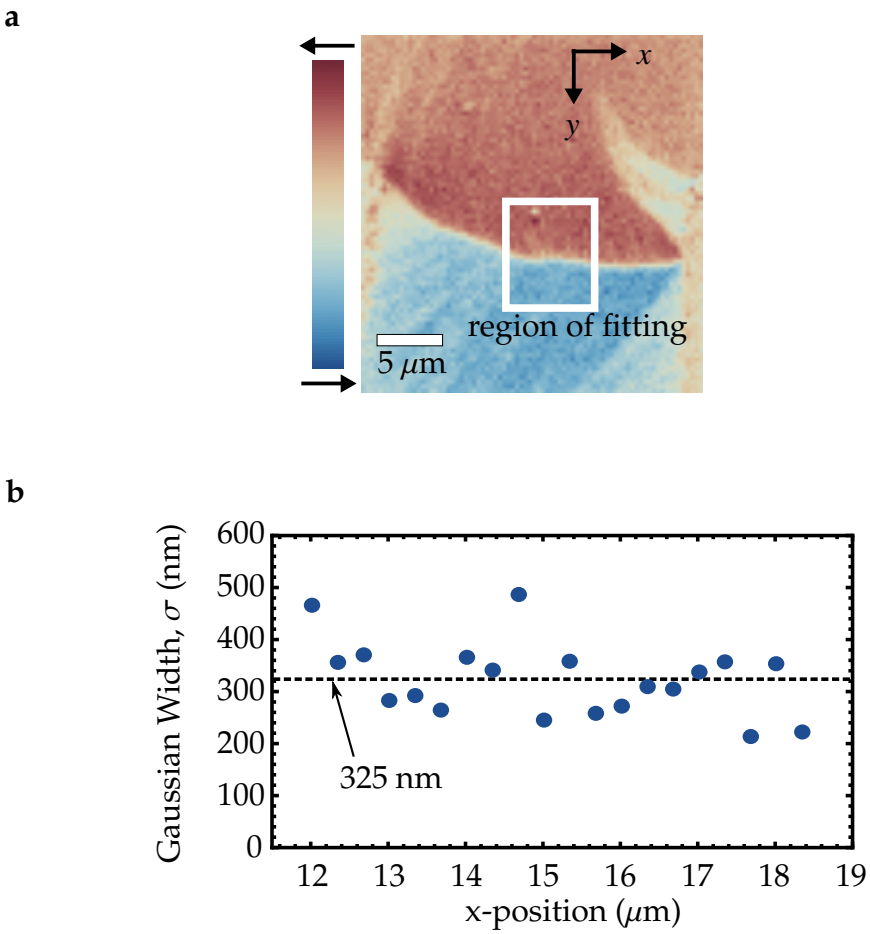

Figure 5.5: Experimentally determining the spatial resolution of TRANE from a domain wall structure.

5.5 Numerical Simulations of Temperature Gradient

We use numerical simulations to predict the relation between the spatial resolution of TRANE with the size of the heat source. The finite element modeling of the thermal gradient evolution used for determining the temperature and thermal decay times was performed using the COMSOL Multiphysics Heat Transfer Module. We consider a single temperature diffusive model in which the laser is treated only as a heat source, rather than considering the specific photon inter-

actions with the phonon and electrons. This is justified by the fact that the optically excited electrons are thermalized on time scales comparable to the laser pulse width of 3 ps [100]. In our model, we consider a Py sample with lateral dimensions of 10 μm $\times$ 2 μm and 30 nm thick, placed on top of a bulk sapphire substrate. For the calculation, we assume that the heat is only generated in the Py, which is valid due to the large bandgap of sapphire, leading to it being transparent to the laser. The spatiotemporal evolution of the tempearture gradient in our system is calculated numerically with the Fourier diffusion equation using the material parameters given in Table 5.1. The heat source $Q(\vec{x}, t)$, is given by,

$$Q(\vec{x}, t) = \frac{Q_0}{2\pi\,\sigma_x\,\sigma_y} e^{-\left(\frac{1}{2}\right)\left[(x/\sigma_x)^2+\left(y/\sigma_y\right)^2\right]} e^{-z/d} e^{-(t-t_0)(2\tau)^2} \tag{5.7}$$

where, σ_x and σ_y are the Gaussian widths in the x and y direction of the laser spot (310 nm), d is the skin depth (12nm), Q_0 is the incident peak power of a single pulse set to 2.19 W, and τ is the pulse Gaussian temporal width of the 3 ps pulse.

Material	Thermal Conductivity (W m^{-1} K^{-1})	Specific Heat (J g^{-1} K^{-1})	Density (g cm^{-2})
Sapphire [93]	30.3	0.764	3.98
Permalloy	46.4 [101]	0.43 [102]	8.7 [103]

Table 5.1: The material parameters used for the finite element simulation of the temperature.

Figure 5.6a-d shows the cross-sectional temperature due to a 310 nm wide heat source. Fig. 5.6b and c show the evolution of the temperature after the laser pulse. Though after the pulse, the temperature does spread laterally, the out-of-plane temperature gradient does not diverge from the heat source. Since TRANE is only dependent on the temperature gradient in the out-of-plane direction, these simulations confirm the experimental results that the spatial reso-

lution is equal to the size of the thermal source at 310 nm.

To see if the spatial resolution relation to the thermal spot size holds true for smaller sources, we repeat the prior simulations for a heat spot size of 50 nm in width. The results of these simulations are shown in Fig. 5.7. Similar to before, we see that the temperature gradient has the same width as the thermal spot size for a 50 nm wide spot. These simulations suggest that if we can confine the heating spot size to 50 nm, then we can use TRANE to measure magnetic moments with 50 nm spatial resolution. Experimental results have shown with HAMR devices that using a plasmon antenna, one can confine a heat source to such a size [104]. Therefore, using a plasmon antenna to generate a 50 nm heat source for TRANE measurements provides a route to achieve sub-diffraction spatial resolution measurements of magnetization.

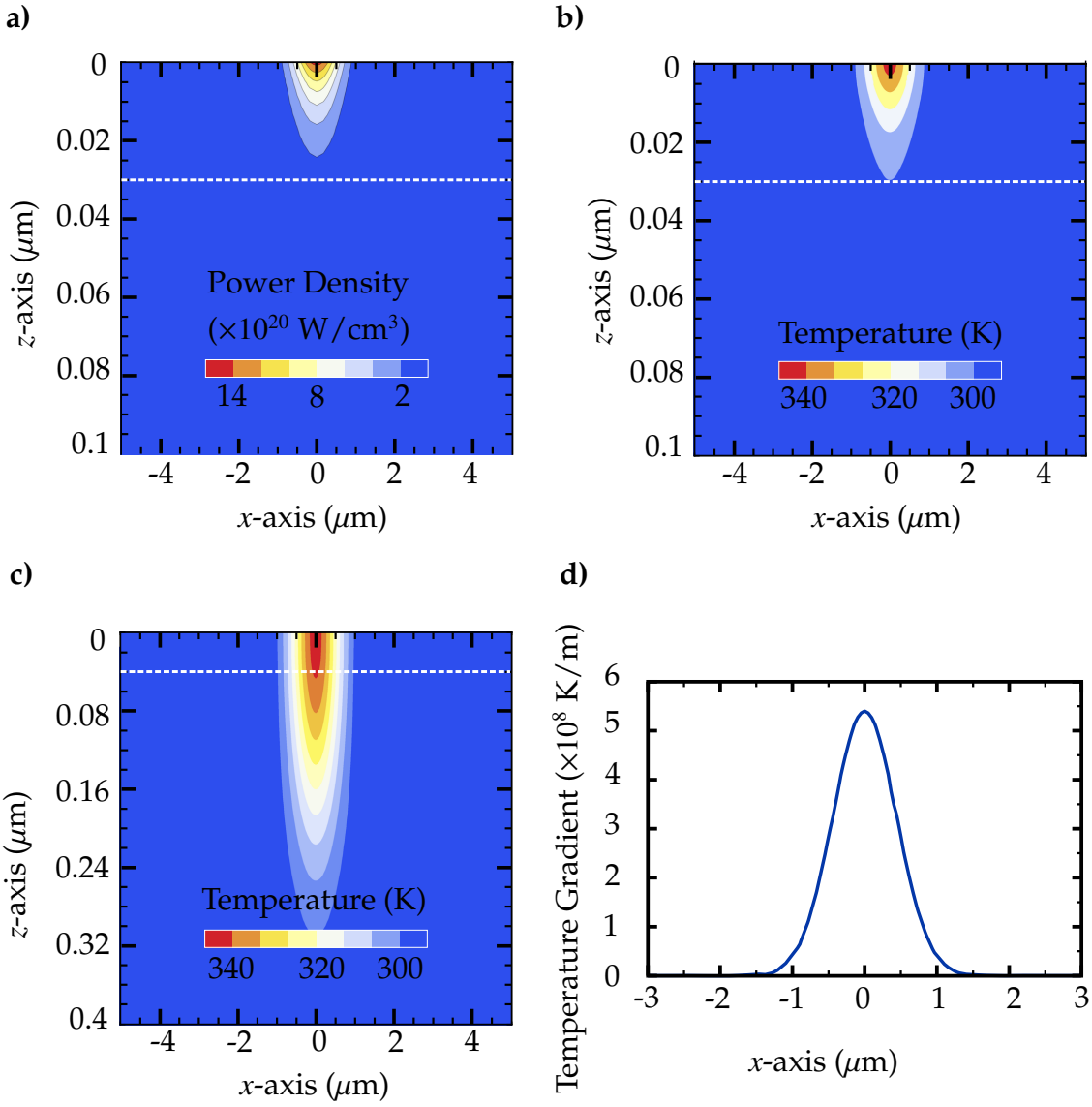

Figure 5.6: Finite element method numerical simulations of the temperature gradient for a heat source of 310 nm in width. The white dashed line shows the interface of Py and sapphire. **a)** the power density of the heat source. **b)** the temperature at the peak of the pulse. **c)** the temperature 982 ps after the peak. **d)** the temperature gradient profile at the top surface of Py.

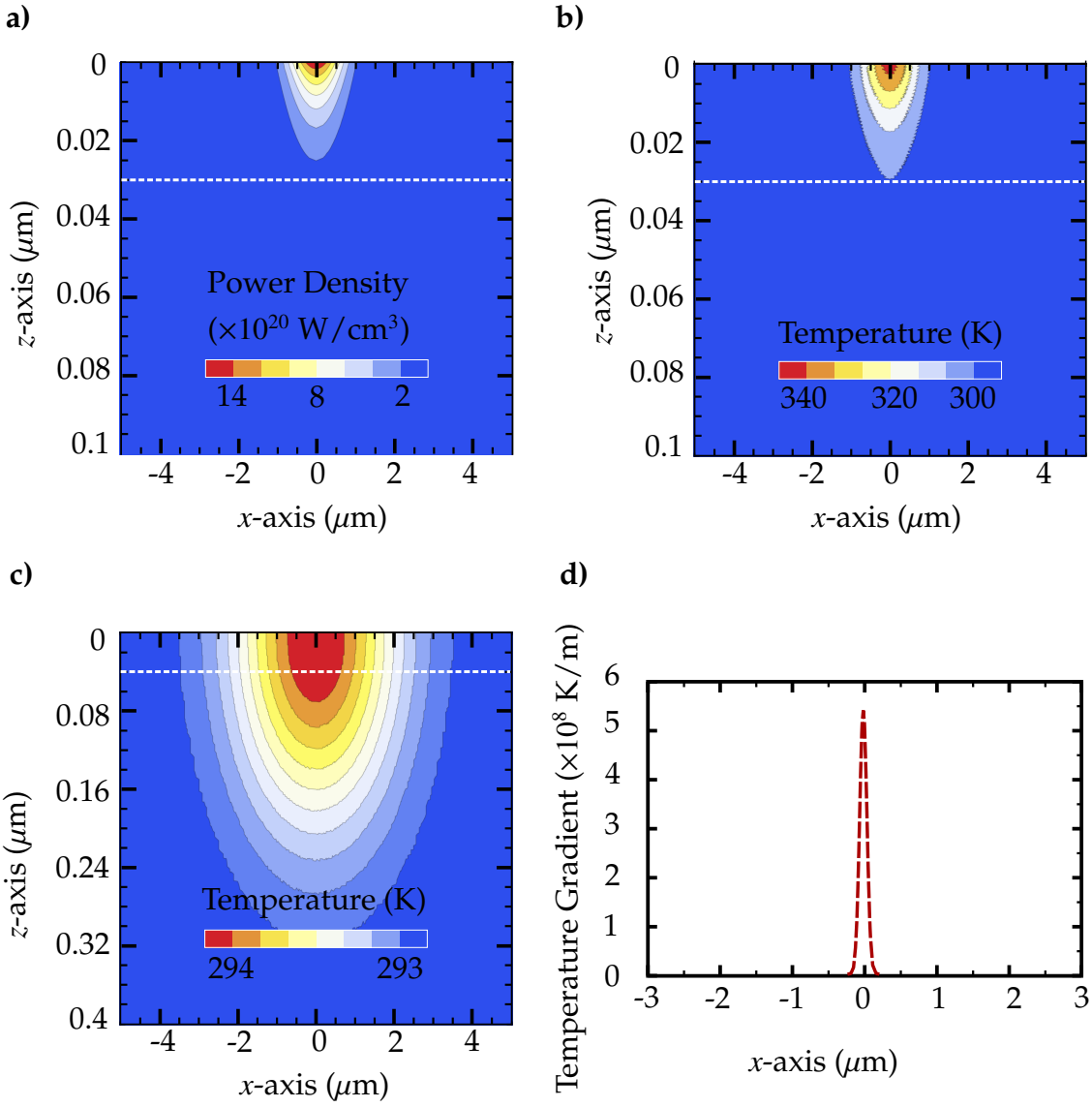

Figure 5.7: Finite element method numerical simulations of the temperature gradient for a heat source of 50 nm in width. The white dashed line shows the interface of Py and sapphire. **a)** the power density of the heat source. **b)** the temperature at the peak of the pulse. **c)** the temperature 982 ps after the peak. **d)** the temperature gradient profile at the top surface of Py.

CHAPTER 6

TRANE MEASUREMENT OF TIME VARYING MAGNETIZATION

In this chapter, we use ferromagnetic resonance (FMR) to demonstrate the temporal capabilities of TRANE. FMR is the spatially uniform magnetic precession about the equilibrium position. It is chosen to demonstrate TRANE microscopy capabilities because it is the simplest and the most studied of the magnetic dynamics phenomena. We use TRANE FMR measurements up to 16.4 GHz to show that for the sample measured the upper bound of the temporal resolution 30 ps. Further, numerical simulations suggest that the temporal resolution is approximately 10 ps. With the TRANE FMR measurements, we find the damping to be the same as the electrical measurements as will be discussed in Chapter 7, which suggests that the temperature increase does not disturb the measurement of the magnetic dynamics. We also proceed to use TRANE to measure non-linear dynamics and discuss the intricacies involved with such measurements.

6.1 Time Evolution of the Magnetic Moment

We begin with a theoretical description of the equation of motion of the magnetic system. To describe the temporal evolution of the magnetic moment, we assume the electron spins contributing to the magnetic moment are localized core electrons, therefore do not move under an applied electric field. The Hamiltonian for these core electron spins are described by the Zeeman interaction as

$$\hat{H} = -\gamma \vec{H}_{eff} \cdot \vec{\hat{S}} \tag{6.1}$$

where γ is the gyromagnetic ratio of the electron, $\vec{H}_{eff}$ is the effective magnetic field and $\hat{S}$ is the spin operator. From the Heisenberg picture, the time evolution of the electron spin is given by

$$\begin{aligned} \partial_t \vec{\hat{S}} &= \frac{i}{\hbar}\left[\vec{\hat{S}}, \hat{H}\right] \\ &= \gamma \vec{\hat{S}} \times \vec{H}_{eff}. \end{aligned} \tag{6.2}$$

For the typical ferromagnetic transition metals, we can assume that a large number of spins contribute to the total magnetic moment, thus we can assume the classical limit of

$$\frac{\left\langle \vec{\hat{S}} \right\rangle}{S} = \frac{\vec{M}}{M_S}, \tag{6.3}$$

where S is the magnitude of the spin vector, $\vec{M}$ is the classical magnetization vector and M_s is the saturation magnetization. Applying the classical picture of the spins to Eqn. 6.2, we obtain the equation of motion of the magnetic moment with

$$\partial_t \vec{M} = -\gamma\left(\vec{M} \times \vec{H}_{\text{eff}}\right). \tag{6.4}$$

To account for experimental evidence of magnetic damping in experiments, Gilbert introduced a phenomenological term to give the Landau-Lifshitz-Gilbert equation of [105]

$$\partial_t \vec{M} = -\gamma\left(\vec{M} \times \vec{H}_{\text{eff}}\right) + \frac{\alpha}{M_S}\left(\vec{M} \times \partial_t \vec{M}\right) \tag{6.5}$$

where the α is the phenomenological Gilbert damping term. The LLG equation has been highly successful in describing a wide variety of magnetic phenomena [106].

6.2 Theory of FMR

Ferromangetic resonance (FMR) describes the small angle precession that is driven in resonance by an external driving force, which in this chapter corresponds to a sinusoidal driving magnetic field. To describe the theory of FMR, we begin with the small angle approximation of the LLG equation, such that

$$\vec{M} = \vec{M}_0 + \vec{m}(t) \tag{6.6}$$

where $\vec{M}_0$ is the static equilibrium magnetic moment and the $\vec{m}(t)$ describes the excitation. In the small angle approximation, $|\vec{m}| \ll M_S$. Applying this to the LLG equation of Eqn. 6.5, and taking to first order of m, we have

$$\partial_t \vec{m} = -\gamma \left(\vec{M} \times \vec{H}_{\text{eff}} + M_s \vec{m} \times \vec{H}_{\text{eff}} \right) + \frac{\alpha}{M_s} \left(\vec{M} \times \partial_t \vec{m} \right). \tag{6.7}$$

To describe the effective magnetic field, we need to consider the finite size effects of the system. The finite size of the ferromagnetic device creates an effective shape anisotropy for the magnetic moment as a consequence of the dipolar interactions. For an ellipsoidal shaped ferromagnet, the free energy can be expressed as[107]

$$F = \frac{M_x^2 N_x}{2} + \frac{M_y^2 N_y}{2} + \frac{M_z^2 N_z}{2} - \vec{M} \cdot \vec{H}_a, \tag{6.8}$$

where $\vec{H}_a$ is the applied mangetic field, M_i is the component of the magnetic moment in the x, y, z direction, and N_x, N_y, and N_z are unitless phenomenological anisotropic constants, ranging between 0-1, such that $N_x + N_y + N_z = 1$. Hence, the effective field is given by

$$\begin{aligned} \vec{H}_{eff} &= -\frac{\partial F}{\partial \vec{M}} \\ &= \vec{H}_a - N_x M_x \hat{x} - N_y M_y \hat{y} - N_z M_z \hat{z}. \end{aligned} \tag{6.9}$$

We can determine the anisotropic constants N_i by measuring the demagnetizing fields $H_{d,i}$ for the given direction,

$$H_{d,i} = -N_i M_s, \tag{6.10}$$

where i is one of x, y, z. In this chapter, we measure magnetic dynamics of thin film samples patterned into wires and label the axis to correspond to those depicted in Fig. 6.1. The shape anisotropy of the samples are approximated as an elongated ellipsoid and we treat the long axis anisotropy as $N_x = 0$ and we measure $N_y = H_{d,y}/M_s$ and thus $N_z = 1 - N_y$.

To drive the ferromagnetic resonance, we apply a static magnetic field along the direction of the wire, $H_0\hat{x}$, and a perpendicular AC magnetic field, $\vec{h}(t)$. The total effective magnetic field can be expressed as

$$\vec{H}_a(t) = H_0\hat{x} + \vec{h}(t) - N_x M_x\hat{x} - N_y M_y\hat{y} - N_z M_z\hat{z}. \tag{6.11}$$

Fig. 6.1 shows the magnetic fields and their directions along with the precessing magnetic moment. Applying the effective field and the magnetic moment of Eqn. 6.6 to the LLG equation of Eqn. 6.5 and taking the first order of m and h, we can express the time evolution of the magnetic moment as

$$\dot{\vec{m}} = -\gamma\left[M_s\left(m_z N_z\hat{y} - m_y N_y\hat{z}\right) - m_y H_0\hat{z} + m_z H_0\hat{y} + M_s\hat{x}\times\vec{h}\right] + \alpha\left(\hat{x}\times\dot{\vec{m}}\right). \tag{6.12}$$

From the description of FMR in Fig. 6.1, it is driven by an out-of-plane sinusoidal field, which can be expressed as $h_z(t) = Re[\tilde{h}_z e^{i\omega t}]$. With the excitation field as a sinusoidal pattern, the magnetic moment can similarly be written as $m_i(t) = Re[\tilde{m}_i e^{i\omega t}]$. Note that $\tilde{h}_z$ and $\tilde{m}_i$ are both complex. Applying these expressions to Eqn. 6.12, we can show that each component of the magnetic moment

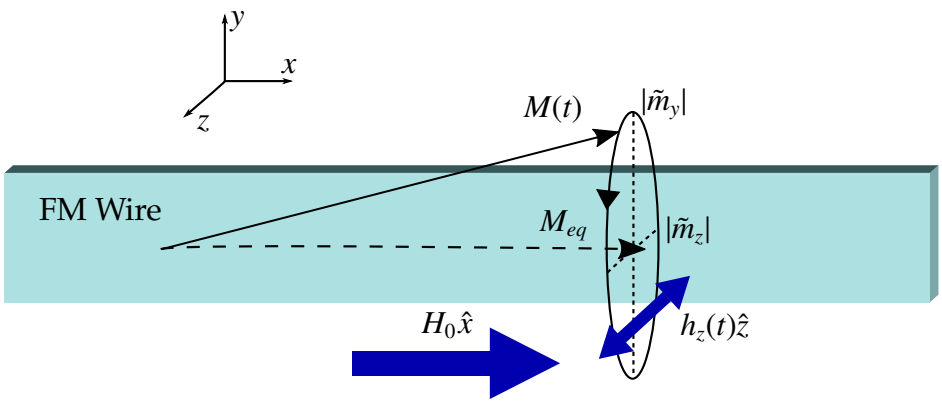

Figure 6.1: Depiction of the ferromagnetic resonance.

can be expressed in terms of a matrix equation as

$$\begin{pmatrix} i\omega & \gamma(H_0 + M_s N_z) + i\alpha\omega \\ -\gamma(H_0 + M_s N_z) - i\alpha\omega & i\omega \end{pmatrix} \begin{pmatrix} \tilde{m}_y \\ \tilde{m}_z \end{pmatrix} = \gamma M_s \begin{pmatrix} \tilde{h}_z \\ 0 \end{pmatrix}. \tag{6.13}$$

Solving the matrix equation to give the expression for $\tilde{m}_y$ gives

$$\tilde{m}_y = \frac{i\gamma\omega M_s \tilde{h}_z}{-\omega^2 + \left[\gamma(H_0 + M_s N_y) + i\alpha\omega\right]\left[\gamma(H_0 + M_s N_y) + i\alpha\omega\right]}, \tag{6.14}$$

and similarly for $\tilde{m}_z$ gives

$$\tilde{m}_z = \frac{\gamma M_s \tilde{h}_z \left[\gamma(H_0 + M_s N_y) + i\alpha\omega\right]}{-\omega^2 + \left[\gamma(H_0 + M_s N_y) + i\alpha\omega\right]\left[\gamma(H_0 + M_s N_y) + i\alpha\omega\right]}. \tag{6.15}$$

From the expressions of $\tilde{m}_y$ and $\tilde{m}_z$, we can see that there is a phase difference of approximately $e^{i\pi/2}$ between the two components. This shows that the magnetic moment will oscillate about the equilibrium position in a ellipsoidal pattern.

The expression for the magnetic moment can be simplified to show the physics more clearly with several assumptions. For the magnetic materials considered, the magnetic damping is low such that $\alpha \ll 1$. By taking the approximation $1 + \alpha^2 \approx 1$ and using the fact that $N_y + N_z = 1$, we can express the Fourier

component of the y-component of the magnetization as

$$\tilde{m}_y = \left(i\gamma\omega M_s \tilde{h}_z\right) \frac{1}{\gamma^2(H_0 + M_s N_y)(H_0 + M_s N_z) - \omega^2 + i\alpha\omega\gamma(2H_0 + M_s)}. \tag{6.16}$$

By defining H_r in terms of the driving frequency ω such that

$$\omega^2 = \gamma^2(H_r + M_s N_y)(H_r + M_s N_z), \tag{6.17}$$

we arive at the expression of

$$\tilde{m}_y = \left(\frac{i\gamma\omega M_s \tilde{h}_z}{\gamma^2(H_0 + H_r + M_s)}\right)\left(\frac{(H_0 - H_r) - i(\alpha\omega/\gamma)\left(\frac{2H_0+M_s}{H_0+H_r+M_s}\right)}{(H_0 - H_r)^2 + \left[(\alpha\omega/\gamma)\left(\frac{2H_0+M_s}{H_0+H_r+M_s}\right)\right]^2}\right). \tag{6.18}$$

If we define

$$\Delta H = \left(\frac{\alpha\omega}{\gamma}\right)\left(\frac{2H_0 + M_s}{H_0 + H_r + M_s}\right) \tag{6.19}$$

the magnetic moment can be simplified to

$$\tilde{m}_y = \left(\frac{M_s}{\alpha(2H_0 + M_s)}\right)\left(\frac{1 + i\left(\frac{H_0-H_r}{\Delta H}\right)}{1 + \left(\frac{H_0-H_r}{\Delta H}\right)^2}\right)\tilde{h}_z. \tag{6.20}$$

Since $\alpha \ll 1$, we can see from the denominator of the second term in Eqn. 6.20 that for $|H_0 - H_r| \gg \Delta H$, the denominator of the second term is large and thus the magnetic moment precession is small. The magnetic dynamics are measurable in size when $|H_0 - H_r| \ll H_0$, where the denominator in the second term is small. Under such conditions, the denominator of the second term is minimized when $H_0 = H_r$, thus leading to the maximum precession angle. Therefore, when measuring magnetic dynamics, we can approximate ΔH as

$$\Delta H \approx \frac{\alpha\omega}{\gamma}. \tag{6.21}$$

Finally, the y-component of the magnetic moment in the time domain is given by

$$m_y(t) = \left(\frac{M_s}{\alpha(2H_0 + M_s)}\right)\left[\cos(\omega t + \phi)\left(\frac{1}{1 + \left(\frac{H_0-H_r}{\Delta H}\right)^2}\right) - \sin(\omega t + \phi)\left(\frac{\left(\frac{H_0-H_r}{\Delta H}\right)}{1 + \left(\frac{H_0-H_r}{\Delta H}\right)^2}\right)\right]\left|\tilde{h}_z\right|, \tag{6.22}$$

where ϕ is the phase of $\tilde{h}_z = \left|\tilde{h}_z\right| e^{i\phi}$. We can see that the magnetic response to the driving field is in the form of a linear combination of a symmetric and antisymmetric Lorentzian, where ΔH is the linewidth. The peak of symmetric Lorentzian occurs at $H_0 = H_r$, therefore, we can define H_r as the resonant field. Therefore, the Kittel FMR frequency as a function of the applied magnetic field, H_0 along the easy axis, with the anisotropic effective fields is given by

$$f = \frac{\gamma}{2\pi}\sqrt{(H_0 + N_y M_s)(H_0 + N_z M_s)}. \tag{6.23}$$

6.3 Measuring Magnetic Dynamics with TRANE

We stroboscopically measure magnetic dynamics in $Ni_{20}Fe_{80}$ (permalloy (Py)) wires with TRANE using the apparatus depicted in Fig. 6.2. To excite magnetization dynamics, a microwave frequency current is passed through an on-chip copper wire to generate an out-of-plane AC magnetic field in the permalloy. The wire axis of the sample is aligned parallel to the applied static magnetic field and the contacts are placed so as to measure the M_y component of the magnetization (perpendicular to both the wire axis and the excitation field). To measure magnetic dynamics, we use an additional step of lock-in detection to reference the signal to both the optical chopping frequency and to a small amplitude field modulation along the direction of the static magnetic field. The dual referenced lock-in detection allows us to reject non-magnetic contributions to the signal.

TRANE is a stroboscopic technique, therefore, it can only measure magnetic dynamics with a periodicity that is commensurate with laser repetition rate. Since the laser repetition rate is set and can only be changed by integer multiples from the pulse picker, the magnetic dynamics must be driven with a stimulus

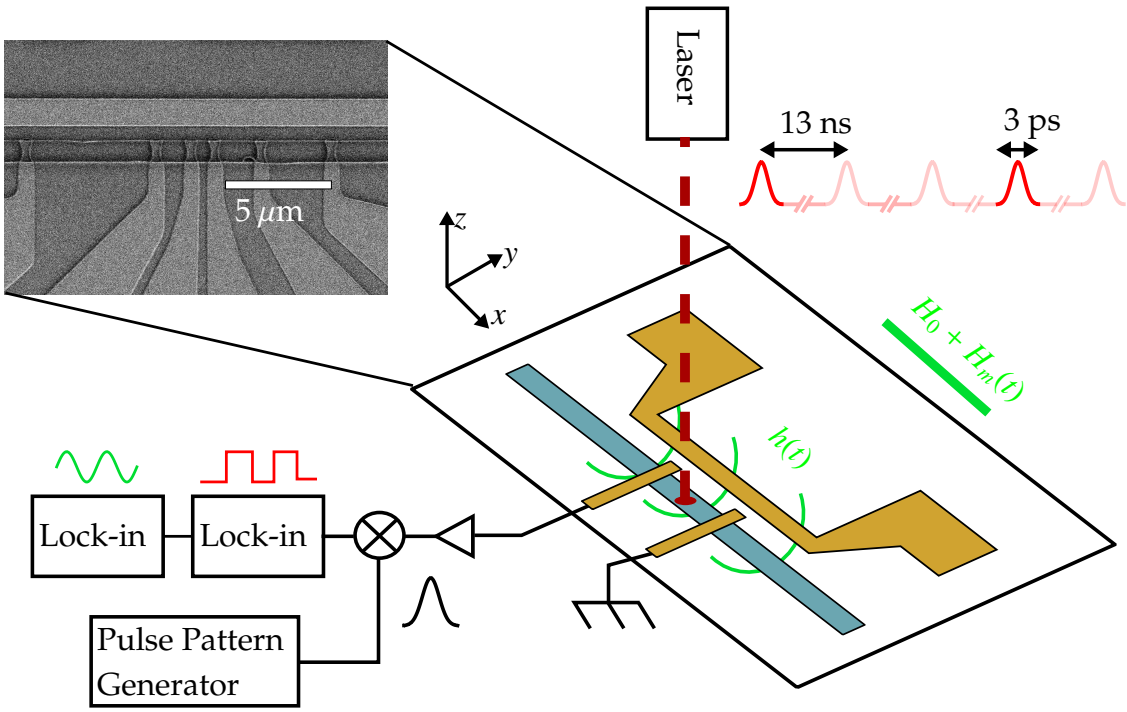

Figure 6.2: The schematic of the temporal measurements with TRANE.

that references the same clock as the laser and also have a period commensurate with the laser repetition rate. We use electrical currents generated by an arbitrary waveform generator (AWG) to excite magnetic dynamics, where we set the proper timing with the laser by using the schematic shown in Fig. 6.3. The laser has a fast photodiode detector that generates a voltage pulse corresponding to the laser pulses. The photodiode voltage is sent to the pulse picker controller, where it outputs a voltage pulse for the repetition rate set by the pulse picker. We use the pulse picker synchronisation output as the input clock of the

pulse pattern generator (PPG), where it output a 1.5 ns width pulse to trigger the AWG.

To induce magnetic dynamics, we have fabricated a copper stimulation wire in close proximity to the magnetic permalloy (Py) wire. The device in which we measure magnetic dynamics with TRANE is shown in Fig. 6.4, where edge to edge distance between the stimulation wire and the Py wire is 1 μm, and both the stimulation wire and Py wire have widths of 2 μm. We connect the stimulation wire to an AWG to pass a time varying current, which allows us to generate fast time-varying magnetic fields. The clock of the AWG is referenced to the 25.3 MHz laser repetition rate and is multiplied up within the AWG to a sampling rate of 19.98 GS/s. Waveforms from the AWG can be delayed in steps of 50 ps with respect to the laser pulses without re-triggering, therefore allowing the time varying magnetic behavior to be stroboscopically probed with TRANE.

To detect the TRANE signal, we connected to the set of electrical contacts that are 3 μm apart, as shown in Fig. 6.4, which resulted in a total DC resistance of 74 Ω. These contacts were chosen to compromise the matching of 50 Ω impendance and enough spacing for possible spatial scans. The resistance of the stimulation wire is 48 Ω, which is close to the ideal 50 Ω impedance match to reduce electrical reflections in the RF circuit. For the TRANE magnetic dynamics measurements, we apply a static magnetic field along the x-direction, so the magnetic moment equilibrium position is along the length of the wire. Therefore passing current in the stimulation wire to generate an out-of-plane magnetic field will excite the magnetic moment away from equilibrium, thus inducing magnetic dynamics.

We calculate the magnetic field generated by the stimulation wire with a

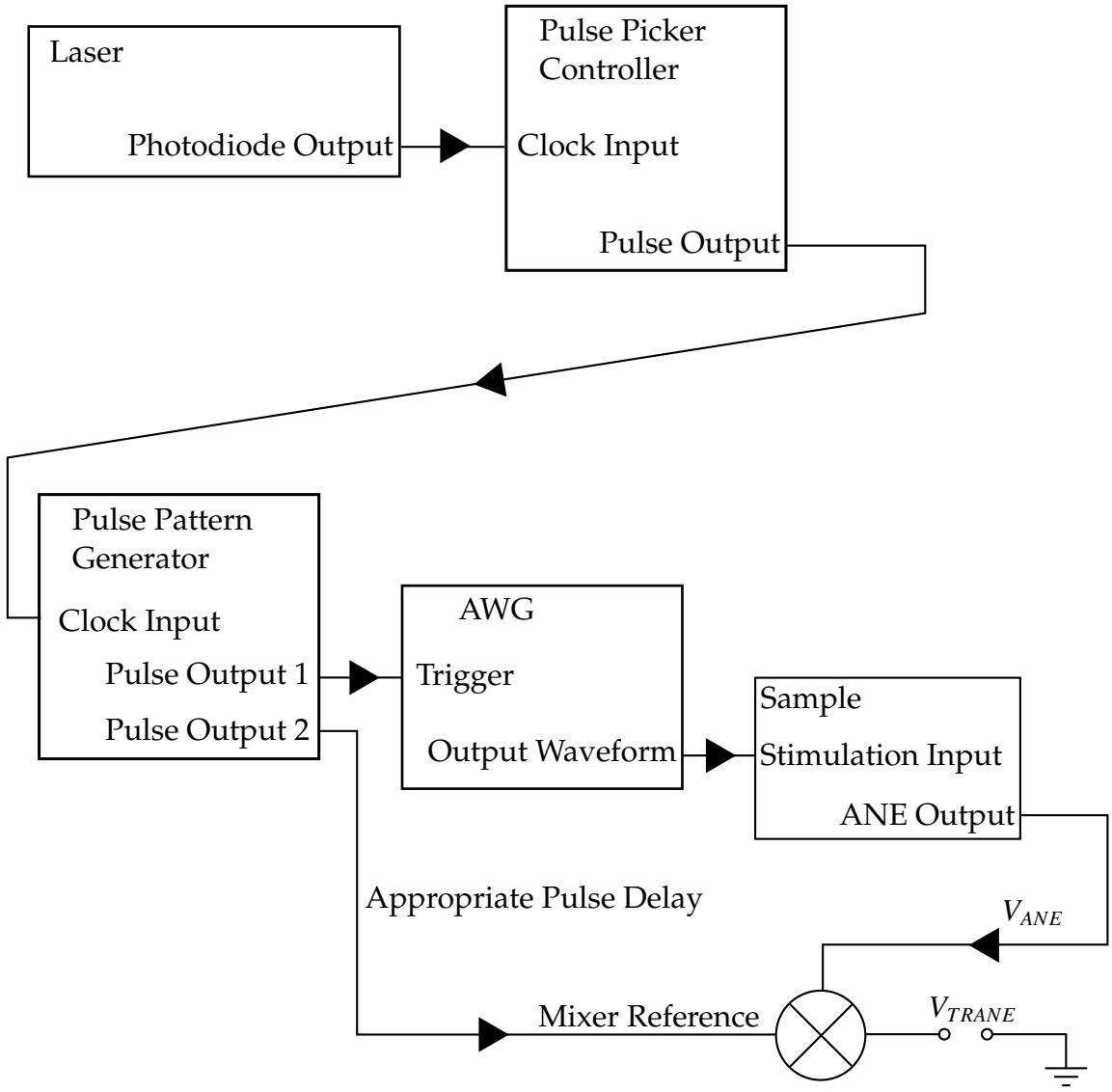

Figure 6.3: The schematic diagram of the timing of the electronics to properly measure magnetic dynamics.

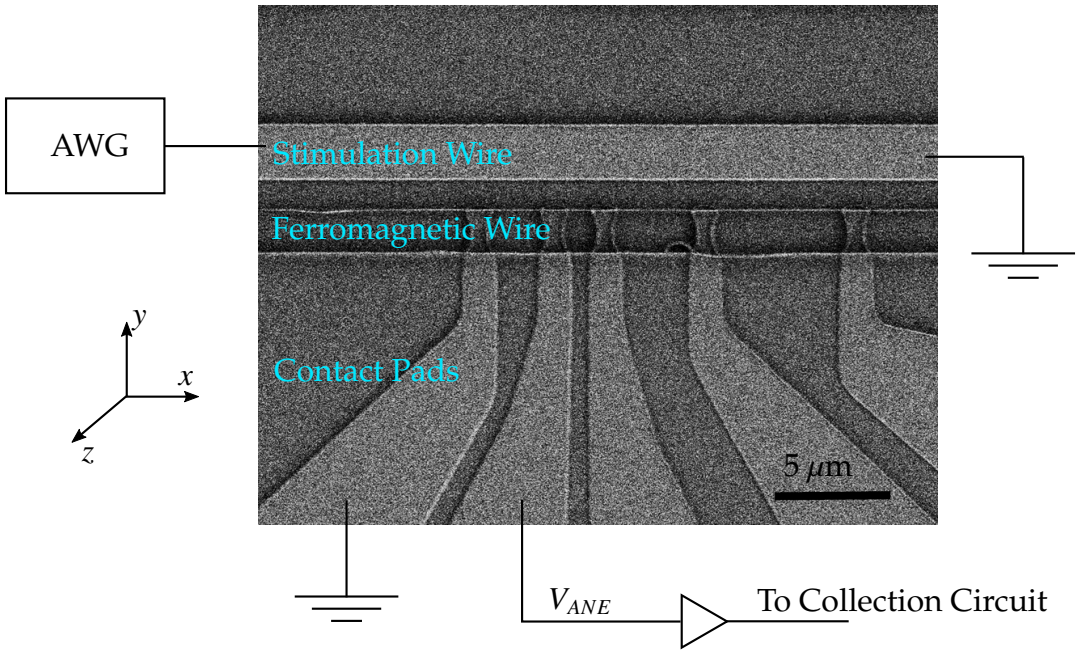

Figure 6.4: The samples to measure magnetic dynamics with TRANE.

finite-element method numerical simulations. Fig. 6.5 shows the calculated out-of-plane magnetic field for a 5 GHz AC current in the stimulation wire with a current density of 2×10^6J/cm^2. Due to the decay in the generated magnetic field away from the stimulation wire, to obtain the largest magnetic field we would place the Py wire close to the stimulation wire. The disadvantage of placing the Py wire in close proximity is the inhomogeneity of the magnetic field. For the 2 μm wire as depicted in Fig. 6.4, where we have a 1 μm spacing, the magnetic field at the near and far edges varies by a factor of 2.

6.3.1 Inductive Cross-Talk

To induce magnetic dynamics, we apply a time varying current in the stimulation wire to generate a corresponding time varying, out-of-plane magnetic field

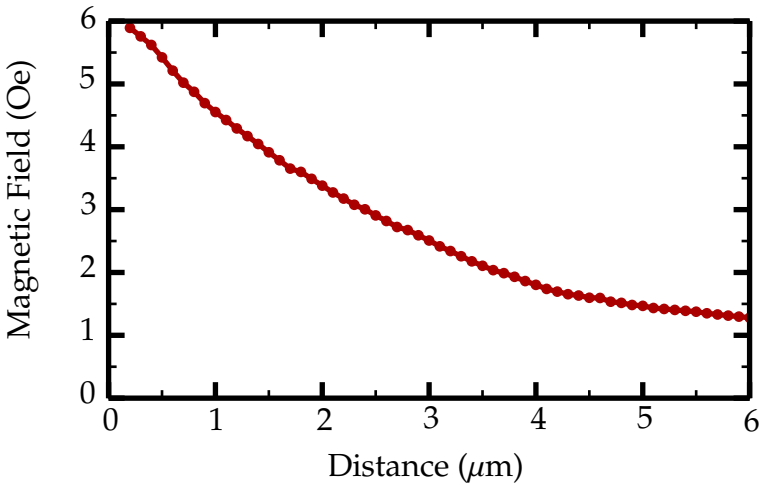

Figure 6.5: The out-of-plane magnetic field generated by a 5 GHz AC current in the stripline.

at the ferromagnetic wire. Due to the geometry of the setup, inductive coupling between the wires causes an induced current in the ferromagnetic wire when we apply a time varying current in the stimulation wire. To determine the inductive coupling between the two wires, we use a vector network analyzer (VNA) to measure S_{21}, the transmission coefficient of the AC power from the input port of the stimulation wire to the output port of the ferromagnetic wire. The amplitude of S_{21} gives the inductive coupling between the stimulation wire and the ferromagnetic wire. Fig. 6.6 shows a VNA measurement of S_{21} for the stimulation wire that is 1 μm away from a 3 μm wide Py wire. These results show that for frequencies ranging from 4-8 GHz, the S_{21} coupling is between -15 dB to -4 dB. This large inductive coupling between the stimulation wire and the ferromagnetic wire leads to a large induced current in the ferromagnetic wire when driving magnetic dynamics. The induced current creates to a large resistive component of the measured signal as discussed in Sec. 8.2. We note that we measure the magnetic dynamics with TRANE of 2 μm wide samples and not

with the 3 μm wide samples, but the general trend for the inductive coupling for either sample is very similar.

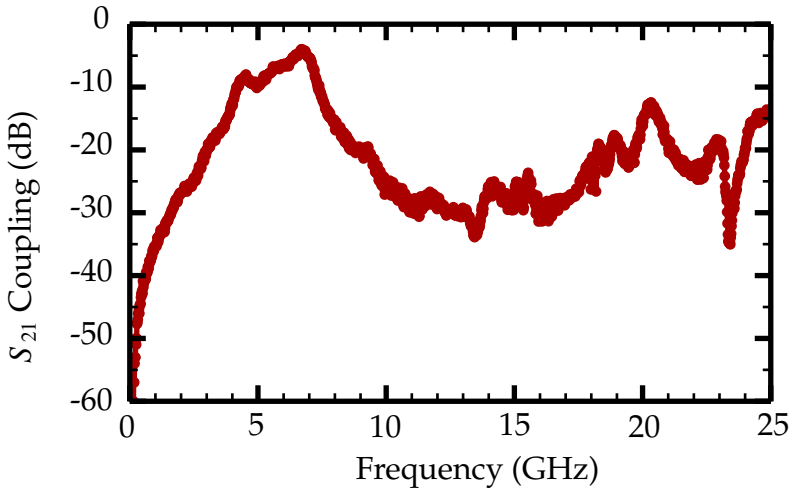

Figure 6.6: The vector network analyzer measurements of the inductive cross-talk between the stimulation wire and the magnetic wire.

6.3.2 Dual Demodulation

Due to the inductive cross-talk between the stimulation wire and the magnetic wire, as described in Fig. 6.6, there is a large electrical current present in the magnetic wire. As will be discussed in Sec. 8.2, the electrical current in the magnetic wire leads to an additional non-magnetic signal in the TRANE measurement. This additional term is proportional to the electrical current in the magnetic wire and has same frequency as the driving frequency and hence magnetic dynamics, thus it will interfere with our measurement of the magnetic dynamics. To remove this additional resistive contribution, we modulate the applied in-plane magnetic field and measure its dependence with a lock-in amplifier. By

modulating the in-plane magnetic field, we only measure the magnetic contribution of the signal, thus we remove the resistive component of the signal.

Dual demodulation is a powerful experimental technique to measure a signal in the presence of a large background [108]. Here, we describe how we measure the magnetic dynamics with TRANE from the dual demodulation of the signal. We express the total TRANE signal as

$$V_{signal} = V_{res}(P_L, t) + V_{TRANE}(P_L, H, t), \tag{6.24}$$

where V_{res} is the resistive signal, which is dependent on P_L, the laser power and V_{TRANE} is the TRANE voltage, dependent on P_L and H, the magnetic field. In this chapter, we perform the dual demodulation measurement by chopping the laser at 9.8 kHz and modulate the field by varying the current in the electromagnet between 5-10 Hz with an amplitude of 13.9 G. By chopping the laser, the power changes between $P_L = {P_L}^0$ and $P_L = 0$, where $V_{res}(P_L = 0, t) = 0$ and $V_{TRANE}(P_L = 0, H, t) = 0$. Higher and more stable frequencies, as described in Sec. 3.1.1 and Sec. 3.2, are used in the latest development of the TRANE setup to provide better results, but were not yet developed when performing the measurements for this chapter. Fig. 6.7 shows the schematic to measure the TRANE voltage with dual demodulation.

The mathematical description of the dual demodulation process is described in Sec. A.1.3. By first demodulating the with the laser chopping frequency, we measure in the first lock-in

$$V_{LI1}(t) = \frac{2}{\pi}\left(V_{res}({P_L}^0, t) + V_{TRANE}({P_L}^0, H(t), t)\right). \tag{6.25}$$

As shown in Fig. 6.7, the x-output of V_{LI1} is the input for the second demodulation, therefore the first phase must be set properly to measure with dual demodulation. In the setup, $\omega_L \gg \omega_H$, thus we can assume that $H(t)$ is constant

over the period of the laser chopping. By demodulating with the magnetic field, we measure only the TRANE voltage corresponding to the magnetic dynamics. Since the 13.9 G magnetic field modulation is on the order of magnitude of the FMR linewidth, we cannot take the linear approximation for the lock-in measurement. The exact treatment will be discussed in Sec. 6.4.1.

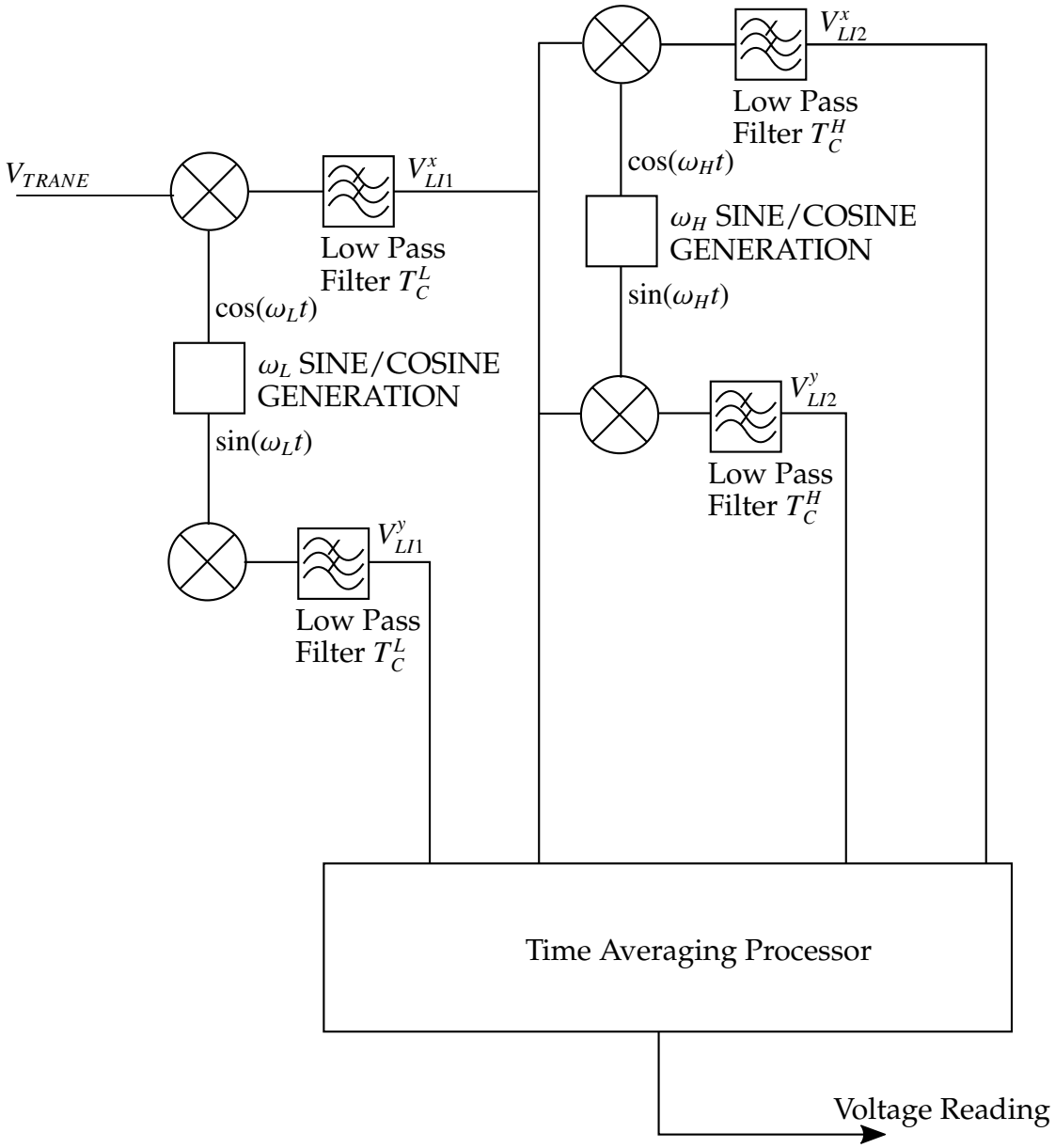

Figure 6.7: The schematic of the dual demodulation TRANE measurement.

6.4 Measuring FMR with TRANE

We excite FMR in the Py wire with the out-of-plane magnetic field generated by an AWG sinusoidal waveform, with the clock referenced to the laser repetition rate. To properly stroboscopically measure with TRANE, the frequency of the AWG created CW waveforms must satisfy both the sampling rate of the AWG and match laser repetition rate, thus constraining TRANE to be capable of measuring only specific discrete frequencies of FMR. To observe the FMR phase behavior, we introduce delays in the AWG waveform in steps of 50 ps with respect to the laser pulses without re-triggering. For excitation frequencies above 5.7 GHz, the output frequency of the AWG was doubled or quadrupled with electrical frequency multipliers to achieve frequencies up to 16.4 GHz. This excitation signal was then amplified to a power between 13-20 dBm and coupled to the copper stimulation wire.

To measure the FMR of the Py wires, we detect the projected in-plane magnetic moment perpendicular to the wire. We plot the stroboscopic TRANE measurements of FMR at 5 GHz as a function of the magnetic field in Fig. 6.8. Fig. 6.8 shows two different phases of the same FMR frequency controlled by electrically shifting the time delay between the microwave magnetic field drive and the laser probe by 50 ps. The corresponding shift of the lineshape results from measuring the magnetic moment at a different part of the precessional cycle, testifying that the short-lived thermal gradient is a time-domain probe.

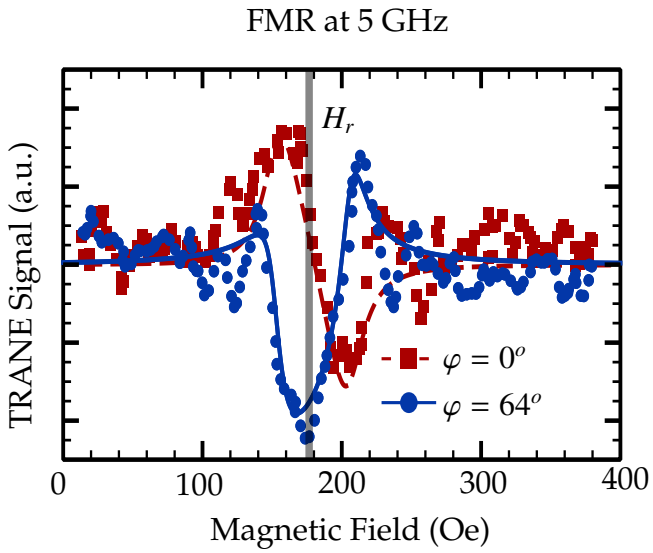

Figure 6.8: The measurement of FMR by varying the static magnetic field.

6.4.1 Fitting FMR

The magnetic moment projection amplitude of the FMR motion is the linear combination of symmetric and antisymmetric Lorentzian functions, as described in Eqn. 6.22. The TRANE voltage is proportional to the magnetic moment projection, thus dependence on the applied magnetic field H_0 is given by

$$V_{TRANE}(H_0) = A\left[\cos(\varphi)\left(\frac{1}{1+\left(\frac{H_0-H_r}{\Delta H}\right)^2}\right) + \sin(\varphi)\left(\frac{\left(\frac{H_0-H_r}{\Delta H}\right)}{1+\left(\frac{H_0-H_r}{\Delta H}\right)^2}\right)\right], \tag{6.26}$$

where H_r is the resonance field and ΔH is the linewidth. When measuring magnetic dynamics with TRANE, a time-varying magnetic field is applied across the ferromagnet. This induces an electrical current in the ferromagnetic wire, which creates a large background voltage across the wire which is removed with a lowpass filter. In addition to the magnetic signal due to FMR, we also detect an induced electrical response from coupling between the microwave antenna and the magnetic channel that is detected because of the temperature in-

duced resistance change. However, since the resistance change contribution is independent of magnetization, we are able to remove it by using the dual demodulation technique described in Sec. 6.3.2. We detect the signal by using two lock in amplifiers connected in series, the first demodulation was referenced to a square modulated 9.7 kHz signal from an optical chopper and the second demodulation was referenced to a 13.9 Oe sinusoidal field modulated at 10 Hz (5 Hz for FMR frequencies above 10 GHz). The TRANE signal detected by the second lock-in can be modeled by

$$S_m(H) = A\Bigg[\cos(\varphi)\int_0^{2\pi/\omega_m}\left(\frac{1}{1+\left[(H_0+H_m\cos(\omega_m t)-H_r)/(\Delta H)\right]^2}\right)dt + \sin(\varphi)\int_0^{2\pi/\omega_m}\left(\frac{(H_0+H_m\cos(\omega_m t)-H_r)/(\Delta H)}{1+\left[(H_0+H_m\cos(\omega_m t)-H_r)/(\Delta H)\right]^2}\right)dt\Bigg]. \quad (6.27)$$

The resulting analytical equation is then used to fit the resonance data obtained with TRANE to quantify the values of the linewidth, amplitude, phase, and center frequency. We note that the modification to the Lorentzian shape does not add free parameters to the fitting function because the modulation amplitude is a known value. The modulation does impact the uncertainty and it reduces the overall signal amplitude, but at the benefit of increased angular sensitivity.

The FMR data are analyzed by fitting to Eqn. 6.27, with the linear combinations of symmetric and anti-symmetric Lorentzian functions modified to account for the magnetic field modulation. We apply the fitting to the 5.00 GHz stimulations of Fig. 6.8, where the two plots are seperated by 50 ps or a quarter period. From the fit, we find a maximum precession angle of 0.07^{o} at the resonant field of 180 Oe. With a sensitivity of $0.093^{\text{o}}/\sqrt{\text{Hz}}$ for this sample, we show that TRANE is capable of measuring small magnetic dynamics.

We also extract from the fit a phase difference between the two of $64^{\text{o}} \pm 24^{o}$. The discrepancy from our expectation of a 90^{o} shift might be due to phase

drift between the excitation and the measurement on laboratory time scales, or because our model accounts only for a single, uniform FMR mode. Close inspection of the two data sets in Fig. 6.8 reveals additional features that are anti-correlated between measurement phases. This suggests more complicated magnetic behavior than we model, including the existence of additional magnetic modes that may influence the accuracy of the phase we extract from fitting. Although full imaging and analysis of these modes is a capability of TRANE microscopy, their detailed study is beyond this scope of the present demonstration.

6.4.2 Kittel Fit

By repeating the TRANE FMR measurements at various frequencies, we plot the resonant frequency dependence on the applied magnetic field in Fig. 6.9. To fit the frequency dependence on the resonant field to the Kittel frequency, we begin with Eqn. 6.23 and apply the expression for the hard-axis demagnetizing field of $H_{d,y} = N_y M_s$ thus giving the expression of

$$f = \frac{\gamma}{2\pi}\sqrt{(H_r + H_{d,y})(H_r + M_s - H_{d,y})}. \tag{6.28}$$

We determine the demagnetizing field of $H_{d,y} = 160$ Oe, by measuring the saturation hard-axis magnetic field with TRANE by applying a magnetic field in the y-direction, as shown in Fig. 6.10. By fitting the frequency with the resonant field, where we have M_s as the only free parameter, we find a saturating magnetic moment of $M_s = 840\,\text{emu/cm}^3$. Using the value of M_s obtained from the fit, we find $N_y = 0.015$, and $N_z = 0.985$.

The inset of Fig. 6.9 plots the linewidth, ΔH versus the FMR frequency, f,

and the fit to the Gilbert damping parameter, α,

$$\Delta H = \frac{2\pi f}{\gamma}\alpha, \tag{6.29}$$

where γ is the gyromagnetic ratio. The TRANE FMR measurements produce a fit of the Gilbert damping for Py to be $\alpha = 0.009 \pm 0.001$. The damping in this sample is consistent with separate FMR measurements that we made by electrically monitoring the DC rectification voltage as discussed in Chapter 7. These results are also in excellent agreement with literature values for permalloy [109, 110]. The consistency among our various measurements and prior reports supports the idea that the local, transient heating of the sample during measurement does not significantly alter its dynamical properties as probed by TRANE microscopy.

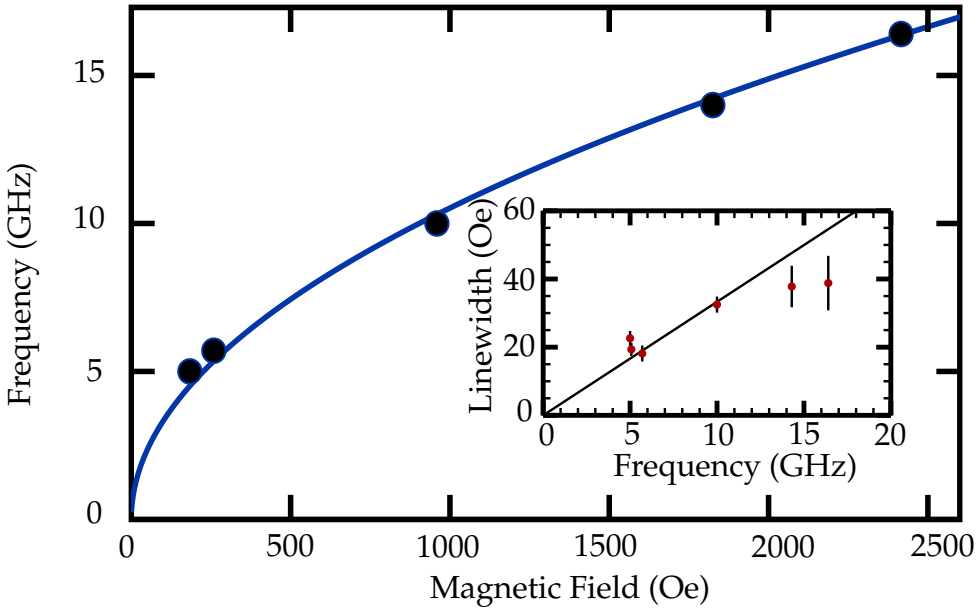

Figure 6.9: A plot of the resonant frequency as a function of the applied magnetic field and the fit to the Kittel frequencies. Inset: The linewidth as a function of resonant frequency to calculate the Gilbert damping parameter.

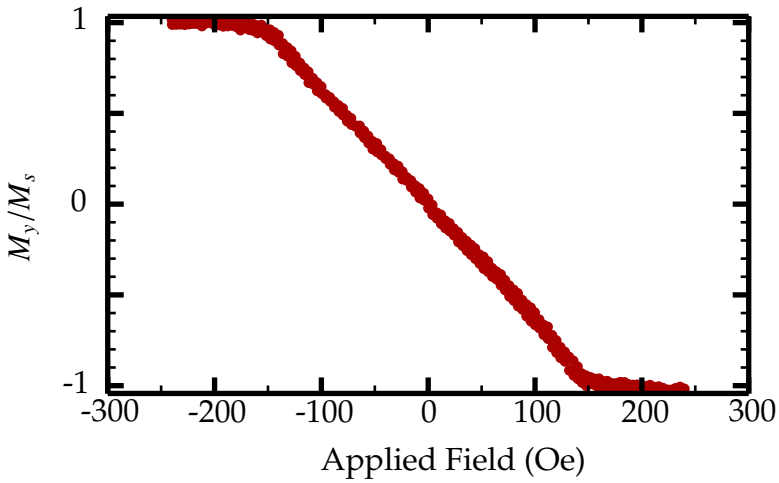

Figure 6.10: We plot the y-component of the magnetic moment measured by TRANE as a function of the applied magnetic field in the y-direction. This provides a measure of the demagnetization field of the hard axis direction of approximately 160 Oe.

6.5 Temporal Resolution

In the TRANE measurement, M_y is stroboscopically transduced by the short thermal pulse. For the TRANE FMR measurement, the drive frequency, f, is chosen to be commensurate with the laser repetition rate, thus creating a constant relationship between the arrival of laser pulses and the phase of the excitation field. The anomalous Nernst voltage generated at the samples electrical pick-ups is

$$V_{ANE}(t) = -\beta N \nabla T_z(t) M_y(t), \tag{6.30}$$

where β is a numerical constant to account for the gain in the collection circuit. Because the magnetization precesses at frequency f, it has a constant phase, φ, with respect to the laser repetition rate. Therefore, Eqn. 6.30 simplifies to

$$V_{ANE}(t) = -\beta N \nabla T_z(t) M_{y,prec} \cos(2\pi f t + \varphi), \tag{6.31}$$

where $M_{y,prec}$ is the precessional amplitude along y. The phase is determined by the relative delay between the laser pulses with respect to the AC magnetic excitation, and defines which segment of the precessional cycle is probed. The final signal we measure after the amplifiers and mixer is described by an integral over the laser pulse period, T, such that

$$V_{TRANE} \propto m_{y,prec} \int_0^T \nabla T_z(t) \cos(2\pi f t + \varphi)\, dt. \tag{6.32}$$

Thus, the magnetic moment is interrogated only when the temperature gradient, $\nabla T_z(t)$, is non-zero. In our case, numerical simulations show in Fig. 6.11 that $\nabla T_z(t)$ is non-zero for approximately 10 ps. We note that if $\nabla T_z(t)$ persists over a duration comparable to a half period of the precession, $\frac{1}{2f}$, then V_{TRANE} will integrate to nearly zero. We use this fact to put an upper bound on the time duration of $\nabla T_z(t)$ from the high frequency FMR measurements.

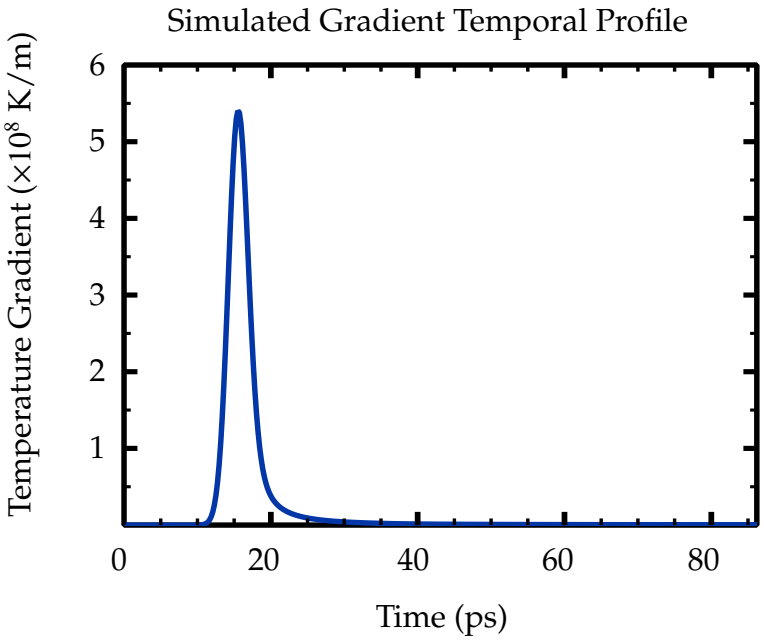

Figure 6.11: The simulated temperature gradient temporal profile.

Direct measurement of the V_{ANE} voltage pulse using an oscilloscope is difficult due to the short temporal duration (ps scale) and the small voltage amplitude (nV scale). As an alternative, we measure the convolution between the V_{ANE} pulse and a reference electrical pulse of known width. In this scheme, we amplify the pulse with two 10 kHz-15 GHz, 15 dB amplifiers (Picosecond Pulse Labs model 5867) and use a high-speed (.5-18 GHz) electrical mixer (Remec model MM94PG-40) to multiply the pulse, V_{ANE}, with an electrical mixing pulse, V_{pulse} of 75 ps in width. When the relative delay between the pulses, τ, is systematically varied, we measure the temporal convolution of the two pulses, V_{mixer} given by

$$V_{\mathrm{mixer}} \propto \int_0^T V_{\mathrm{ANE}}(t)\, V_{\mathrm{pulse}}(\tau - t)\, dt, \tag{6.33}$$

where T is the laser pulse repetition period. The schematic of the timing is shown in Fig. 6.12a. The width of resulting mixed-down signal as a function of τ is most strongly determined but the width of the longest pulse entering the mixer. The measurement of V_{mixer} is shown in Fig. 6.12b with a full-width at half maximum (FWHM) of 75 ps. Since the convolved signal width is similar to the reference pulse width, the V_{ANE} pulses must be shorter than 75 ps.

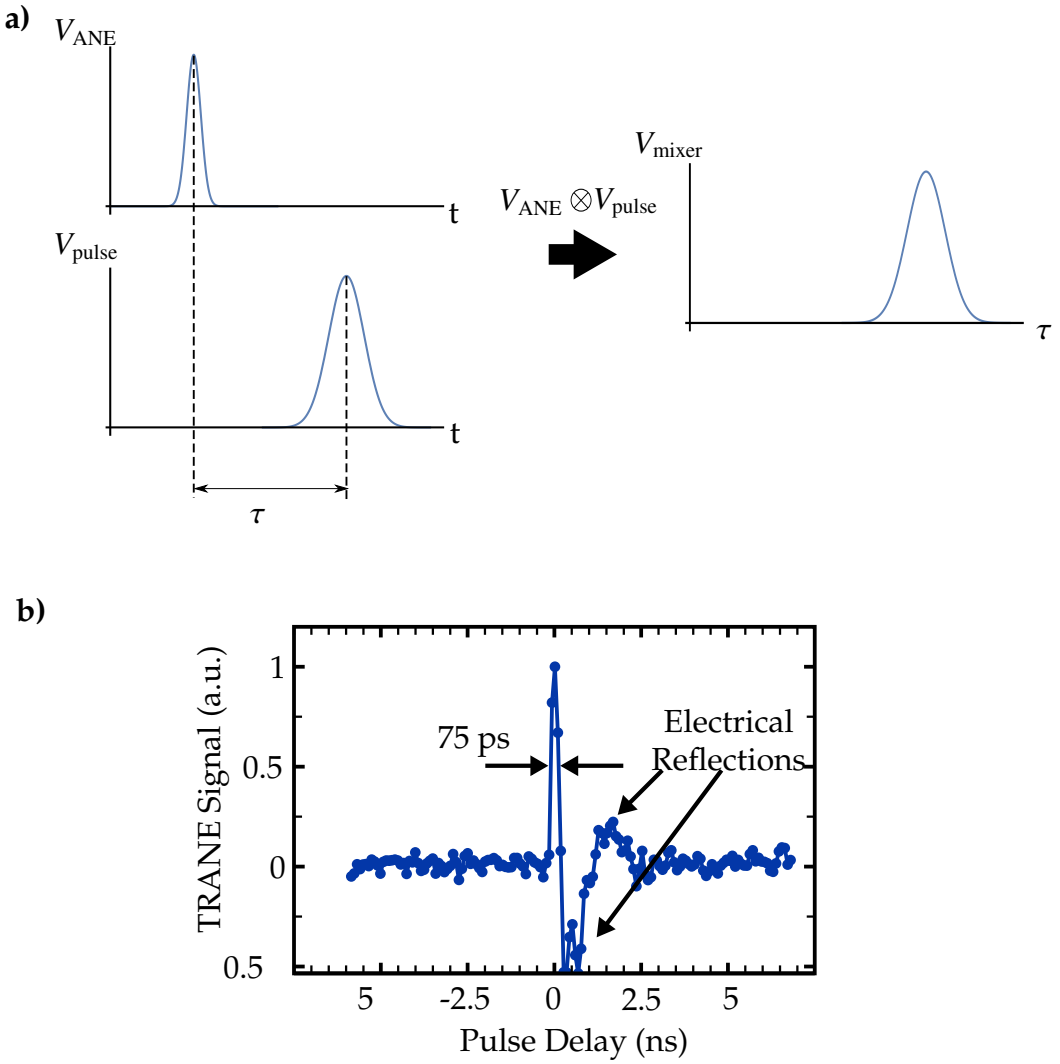

Figure 6.12: **a)** The timing schematic of the convolution between the anomalous Nernst pulse V_{ANE} and the reference pulse V_{pulse} with a time delay of τ to produce the mixing voltage pulse, V_{mixing}.**b)** The measured mixing pulse from a 75 ps reference pulse, suggesting that V_{ANE} is shorter than 75 ps.

We can determine a lower experimental upper bound of the temporal resolution of TRANE from measuring FMR at high frequencies. The highest frequency that our microwave electronics can produce is 16.4 GHz (period of 60 ps), and the results of the TRANE FMR measurement at this frequency is shown in Fig. 6.13, where we observe a clear FMR spectra. As suggested by Eqn. 6.32, the experimental measurement of FMR at 16.4 GHz sets an upper bound of the temporal resolution of TRANE of 30 ps. This is supported by our time-dependent finite element modeling in Fig. 6.11, which shows the temperature gradient pulse has a full width at half-maximum of 10 ps for these samples.

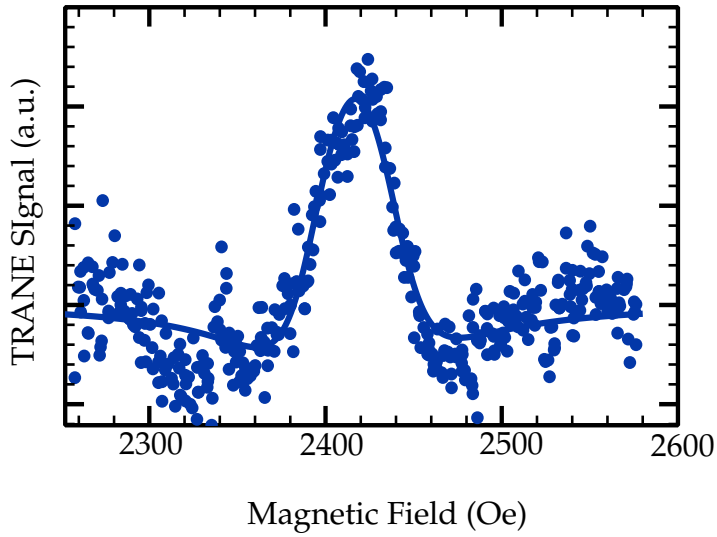

Figure 6.13: Plot of the TRANE FMR measurement at 16.4 GHz.

6.6 RF Pulse Stimulation

We now wish to demonstrate the temporal capabilities of TRANE by measuring non-steady state magnetic dyanmics. To create non-steady state magnetic dynamics, we stimulate the ferromagnet by applying a RF pulse train. Similar

measurements have been measured with TR-MOKE [111]. In this experiment, we apply a 5 GHz RF pulse train of 2.8 ns (14 periods) with the AWG to the stimulation wire to generate an RF magnetic field pulse. The start of each RF pulse is separated by 39.5 ns, the same time separation between the laser pulses. To stroboscopically probe the magnetic dynamics, we vary the relative time delay between the start of the RF pulse and the laser with a shifted waveform using the AWG. This allows our TRANE setup to properly stroboscopically probe the magnetic dynamics.

We would expect the dynamics from an RF pulse to be well described by the FMR theory previously described. During the driving time period, the magnetic moment precession is largest for the magnetic field at the resonant field at 5 GHz. After the pulse, the oscillations should decay at the Kittel frequency corresponding to the applied magnetic field, with higher frequencies for higher fields.

Fig. 6.14 plots two signals as a function of the field and the relative delay with between the start of the RF pulse and the laser pulse at the sample. We use the dual demodulation technique to measure the magnetic dynamics as discussed in Sec. 6.3.2. The plot on the left shows the signal that is demodulated with only the laser power modulation and time averaged over the magnetic modulation period. Therefore, the single demodulation measures the sum of the magnetic and resistive contributions. Since the resistive contribution is much larger, we can treat the single demodulation plot as a measure of the current in the stimulation wire, and thus the magnetic field. The plot on the right shows the dual demodulated signal with both the laser power and the magnetic field modulations. The dual demodulation signal only measures the magnetic contribution.

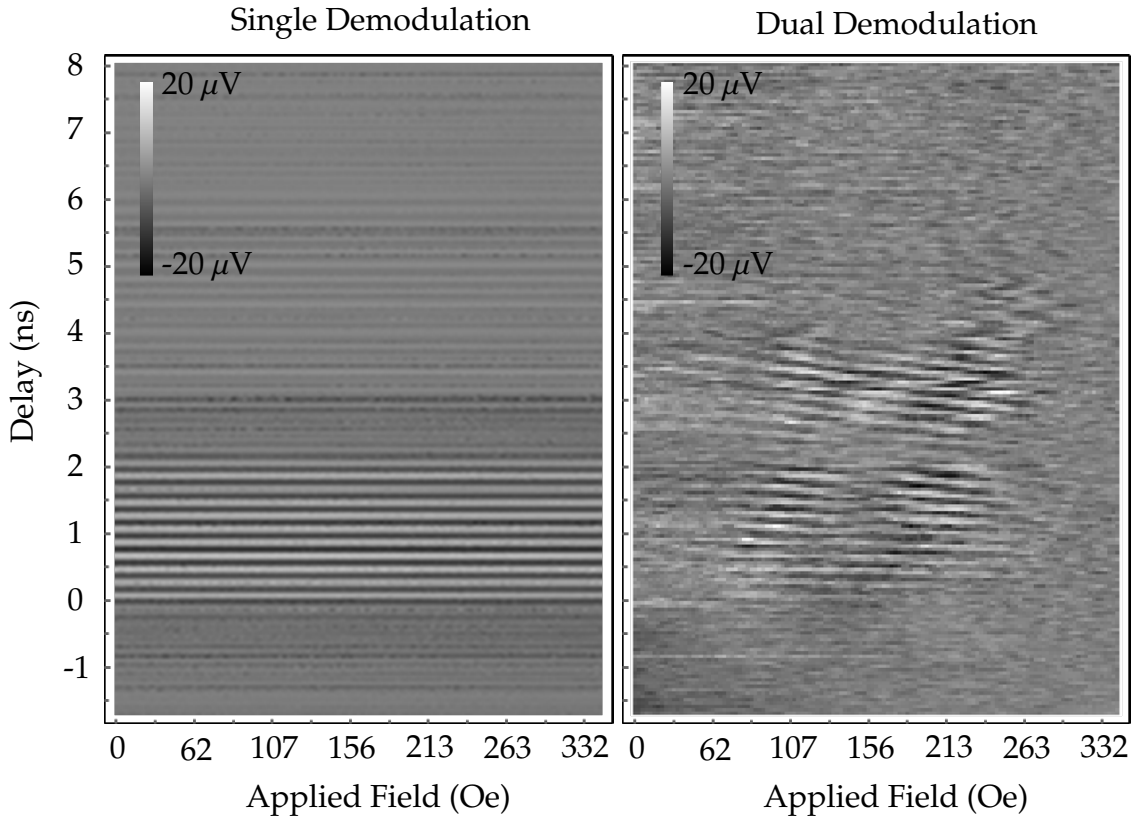

Figure 6.14: The single and dual demodulated signals for a 5 GHz pulse train of 14 periods.

From this plot, we see that during the pulse, we observe magnetic dynamics at 5 GHz. During the driven phase, we can see that the magnetic dynamics vary at a fixed frequency for all applied fields, except for the high fields where we cannot detect a magnetic signal above the noise floor. After the pulse, the magnetic oscillations occur at different frequencies as a function of the magnetic field. The frequency is higher for higher magnetic field as expected from the Kittel frequency. There are two interesting features. First, the magnetic oscillating behavior is large for an appreciable time after the RF pulse ends. Secondly, there is a region between 2-2.5 ns as labeled in Fig. 6.14, where the signal decreases

compared to the signal before and after that time region.

6.6.1 OOMMF simulations

We perform micromagnetic simulations with OOMMF to simulate the magnetic dynamics due to the RF pulse train [112]. The simulation Py sample size had dimensions of 2 μm $\times$ 10 μm $\times$ 10 nm, with a mesh size of 10 nm. We define the axis such that the longest dimension is aligned to the x-axis, and the shortest dimension aligned to the z-axis. A thinner sample was used for the simulation compared to the experiments due to the computer memory constraints of the numerical calculation. With only a single cell in the thickness direction, we have assumed that the measurement was in the thin film limit and the magnetization is constant throughout the thickness of the sample. The magnetic parameters for the simulations were an anisotropy of $K = 0$, an exchange stiffness of $A = 1.3 \times 10^{-11}$ J/m, and a Gilbert damping of 0.01. The saturation magnetization was chosen to be $M_s = 7.6 \times 10^5$ A/m, to match experimental measurements of the hard axis demagnetization field.

To simulate the magnetic dynamics, we begin with a sample where the magnetic moments are set to an equilibrium with an applied static field in the x-direction. We generate magnetic dynamics by applying an out-of-plane, spatially uniform, sinusoidal time varying magnetic field of 5 GHz for a total time of 2.8 ns (14 periods). The amplitude of the sinusoidal out-of-plane magnetic field is 1 Oe. Since we are in the linear-response regime, we can scale the simulation results to match the experimental measurements. The mean magnetic moment in the y-direction as a function of time is plotted for various applied

static fields in Fig. 6.15.

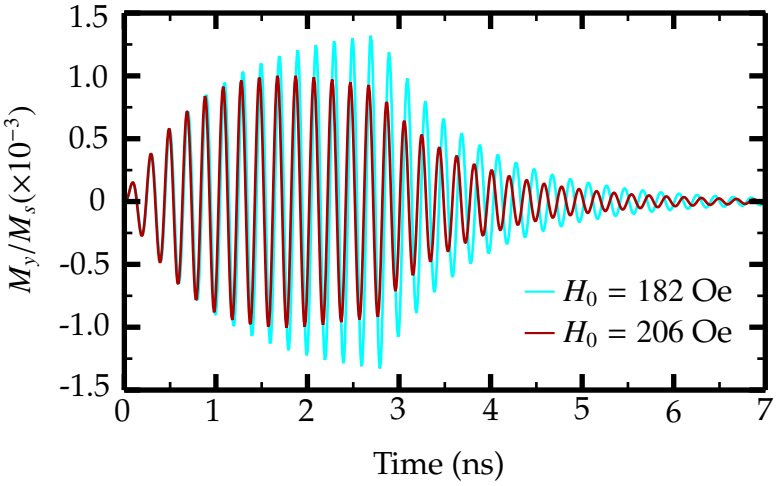

Figure 6.15: The OOMMF simulation of the RF pulse excitation at different static fields.

In the experimental measurement, the magnetic dynamics were measured with the dual demodulation technique, where we modulated the laser power and the magnetic field along the length of the Py wire. To match the simulations, we calculate the modulated signal, S_m from the magnetic dynamics as shown in Fig. 6.15, with the following equation

$$S_m(H_0, t) = \int_0^{2\pi} d\theta \ \cos(\theta)\, m_y(H_x = H_0 + H_m \cos(\theta), t), \tag{6.34}$$

where H_0 is the static magnetic field, $H_m = 13$ Oe is the amplitude of the added field modulation, and t is the relative time after the start of the RF pulse. Fig. 6.16 shows the results of the calculated modulated signal for H_0 and t ranging from 100 – 350 Oe and 0 – 7 ns respectively. To better compare with the experimental results, we introduce noise and set the sampling frequency to match the experimental conditions, where the results are shown in Fig. 6.17. To match the temporal step size in the experiment, we take the data points in Fig. 6.16, where

t is seperated by 50 ps. We introduce the noise by adding to each data point, a random number, which is generated between ±1/5 of the maximal signal in Fig. 6.16, to approximate the signal to noise ratio of the experiment.

Comparing the experimental results of Fig. 6.14 with the simulation results of Fig. 6.17 that there are many features that match between the two. During the RF pulse, where $0 < t < 2.8$ ps, the signal oscillates at a frequency that is independent of H_0 The oscillating signal can only be seen below $H_0 < 250$ Oe, where the signal at fields above that are below the noise level. After the RF pulse, the signal oscillation varies in frequency as a function of the applied field, with the higher fields corresponding to higher frequencies. The feature in the experiment that does not match the simulation is the dead zone occurring after the RF pulse.

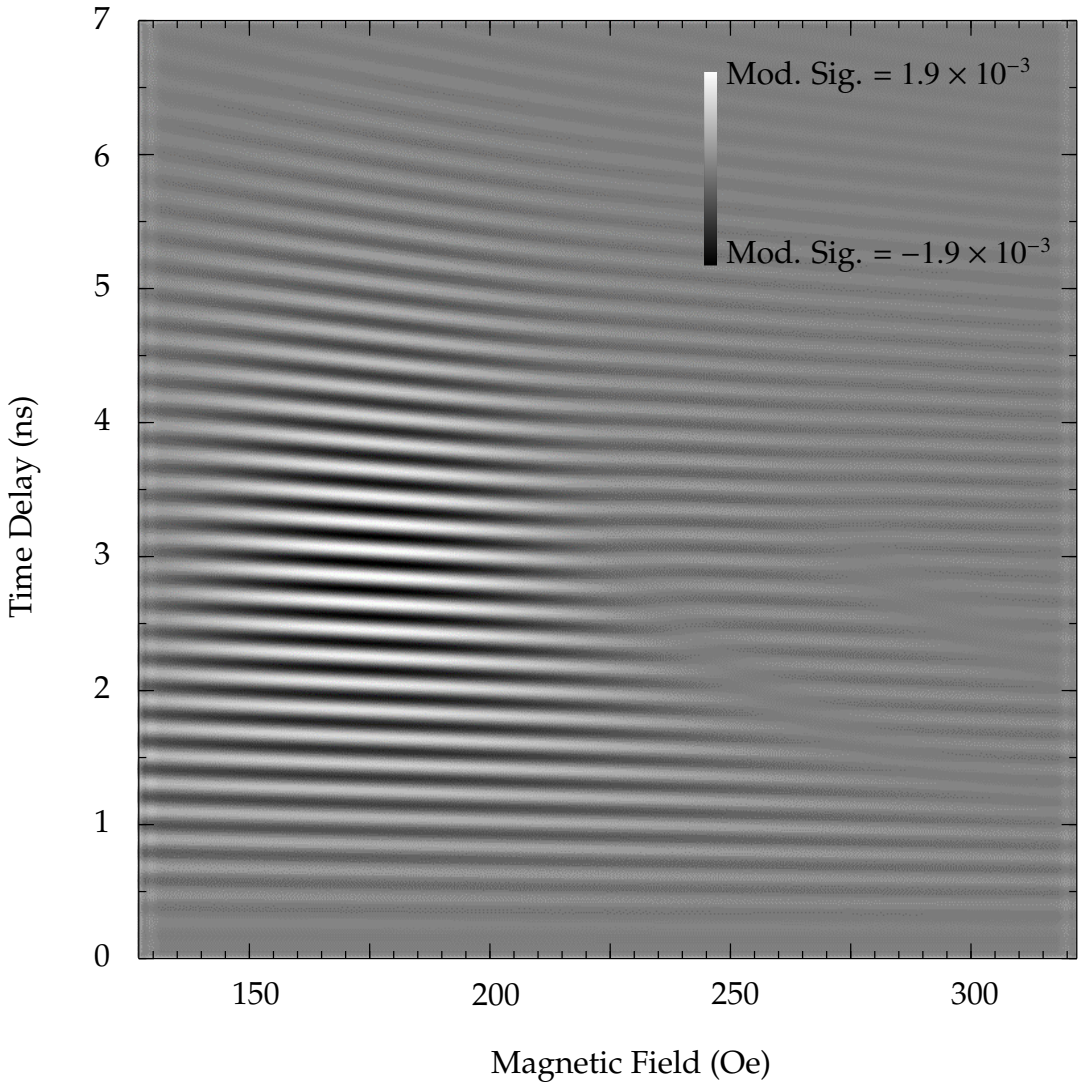

Figure 6.16: The modulated signal of the OOMMF simulation for the RF pulse excitation.

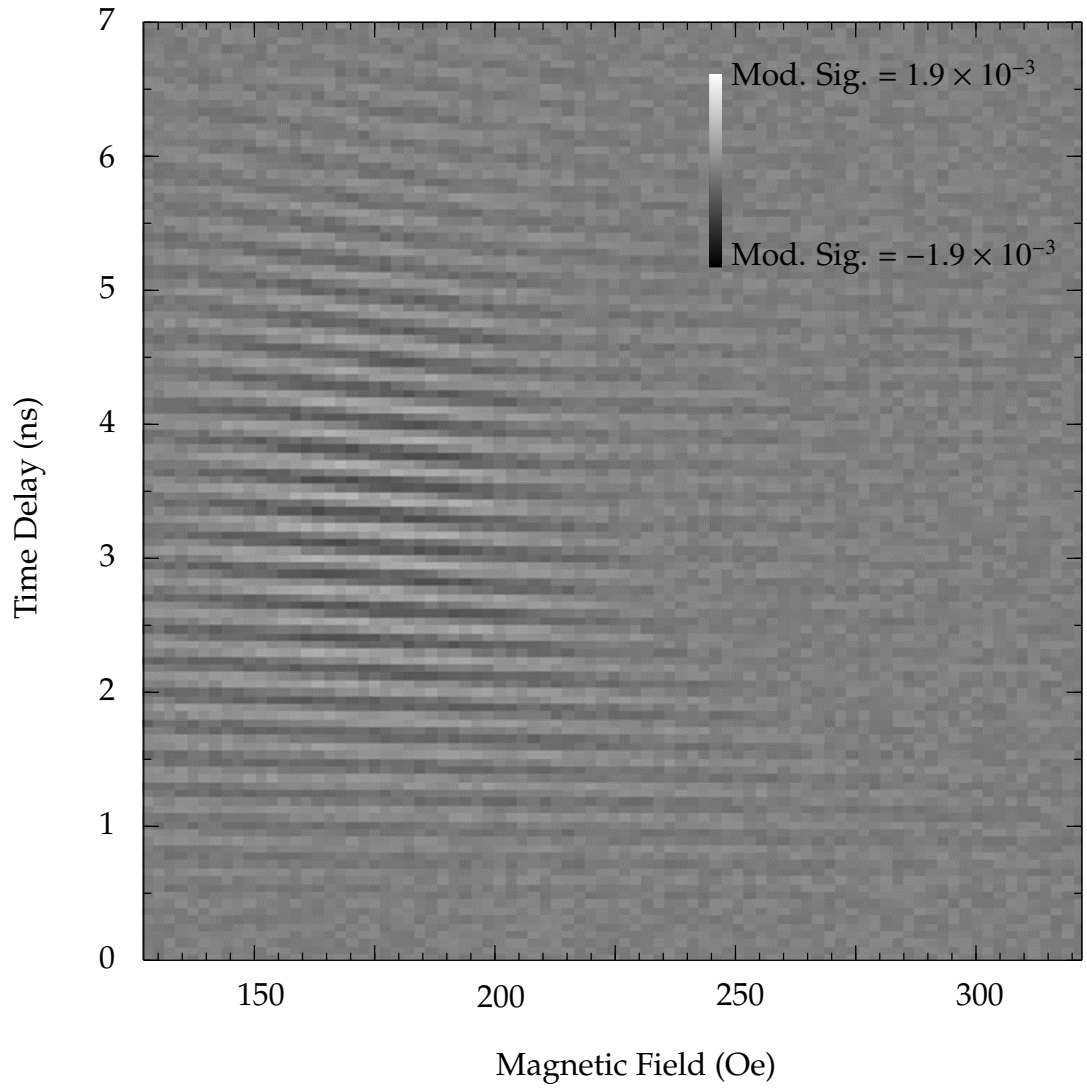

Figure 6.17: The modulated signal of the OOMMF simulation for the RF pulse excitation with noise and sampling rate set to match the experimental results of Fig. 6.14.

To help explain the experimental results, we take line cuts of Fig. 6.16 at various values of H_0, shown in Fig. 6.18. Comparing the results of the simulated magnetic moment of Fig. 6.15 with the modulated signal of Fig. 6.18, the maximum modulated signal does not occur at the time when the magnetic moment is at a maximum. This is because the modulated signal can be approximated by the difference in the magnetic moment as a function of the magnetic field. The large difference in the magnetic moment moment occurs in two regions, near the middle of the RF pulse, where the oscillating magnetic moment is ramping and after the RF pulse ends, where the difference in FMR frequencies cause the magnetic moment to vary in phase as a function of the magnetic field. The phase variance after the RF pulse explains why the long persistance of the modulated signal. A partial explanation of the decrease in the signal from the dead zone in Fig. 6.14 of the experimental data could be caused by the decrease in the modulated signal between the two maximal regions of the ramping regime and the phase change regime. This cannot fully explain the dead zone since the reduced modulated signal from the simulation does not occur at the same time for all magnetic fields.

Another cause for the experimental dead zone could be due to spatially non-uniform magnetic dynamics. Since TRANE is a spatially localized probe, it is sensitive to the spatial variations in the magnetic dynamics. From Fig. 6.5, the magnetic field in the 2 μm wire is highly non-uniform, therefore, there are spatial variations in the magnetic moment. The simulations for a non-uniform magnetic field have not been performed due to the computer memory constraints to save the spatial information of the magnetic moment.

a) Modulated Signal at 182 Oe

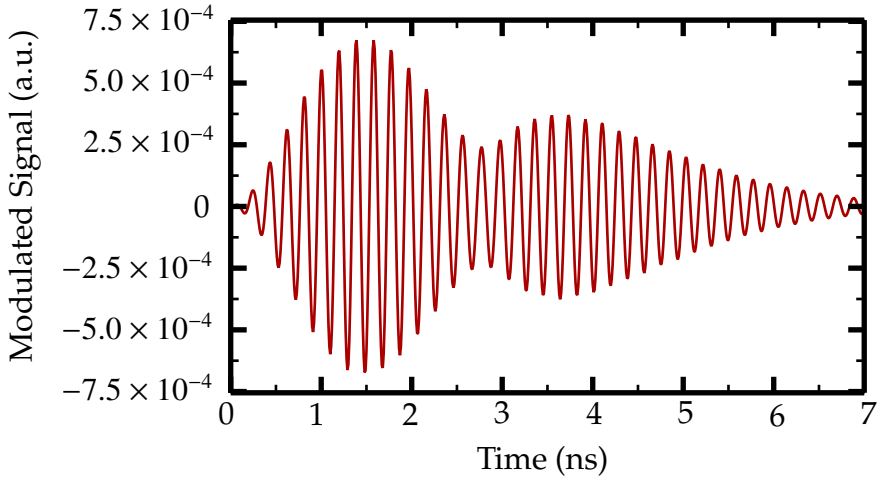

b) Modulated Signal at 206 Oe

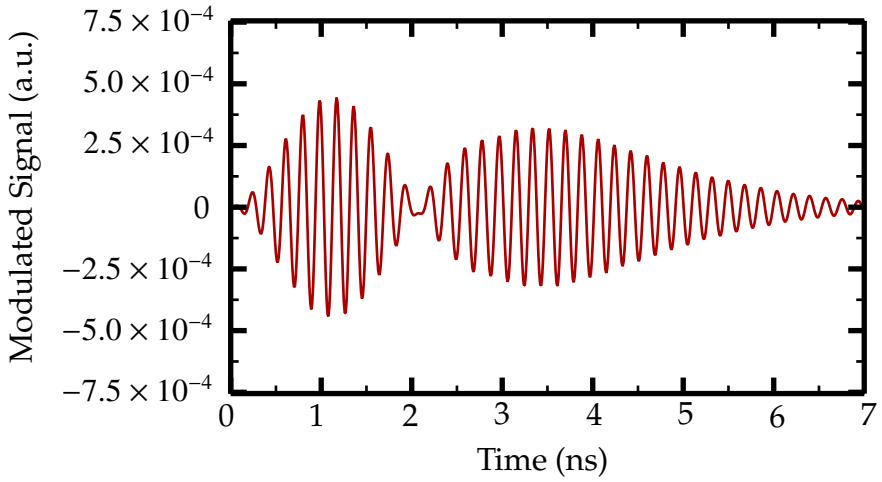

Figure 6.18: The modulated signal at various static magnetic fields from the OOMMF simulation of the RF pulse excitation.

6.7 Impulse Stimulation

The RF pulse induced dynamics are difficult to measure due to the electrical current present in the ferromagnetic wire caused by the inductive coupling. Therefore, measuring the magnetic signal requires dual demodualtion. As shown with the simulation results of the RF pulse, the dual demodulated signal is not straight forward to analyze. To help alleviate the issues involving with measuring magnetic dynamics from RF pulses, we instead can generate magnetic dynamics with a short magnetic field pulse, which we call an impulse excitation. The advantage with the impulse excitation is that the electrical reflections are the same length as the impulse and thus short. This means that for the lock-in measurement with the modulation of the laser power, the electrical cross talk only influences a very short time in the experimental scan.

Here, we perform OOMMF simulations to show the magnetic dynamics induced by such a magnetic impulse and suggest how to best measure such dynamics with TRANE. The simulations are performed on a sample, with dimensions of 5 μm $\times$ 750 nm $\times$ 10 nm, with a mesh size of 10 nm. The magnetic parameters are set to match Py, with an anisotropy of $K = 0$, an exchange stiffness of $A = 1.3 \times 10^{-11}$ J/m, saturation magnetization of $M_s = 7.6 \times 10^5$ A/m and a Gilbert damping of 0.01. We apply a static magnetic field along the long axis of the wire of 182.9 Oe, which corresponds to the ferromagnetic resonance field of 5 GHz. We generate magnetic dynamics with a triangular magnetic pulse of varying widths and with a maximum magnetic field of 1 Oe.

Of the six scans in Fig. 6.19, the 75 ps rise time corresponds to the largest magnetic excitation, with 50 ps and 100 ps rise times producing slightly smaller

magnetic excitation. The magnetic excitation significantly decreases as the magnetic excitation pulse becomes shorter or longer than the optimal width. The impulse excitation can be interpreted as a very short RF pulse, where the largest excitation corresponds to where the spectral function is maximal at the FMR frequency. From the simulations, the optimal rise time is slightly larger than the quarter period of the FMR frequency, which is 50 ps for these simulations. Naively, we would expect the optimal rise time would correspond to a quarter of the period, but a slightly longer rise time produces larger excitations due to the starting conditions.

Comparing the magnetic excitation for the RF pulse in Fig. 6.15 and the optimal excitation pulse of 75 ps in Fig. 6.19, we can see that the magnetic impulse excitation is approximately 1/3 the magnitude of the RF pulse of 14 periods. With the signal to noise ratio of approximately 5:1 from Fig. 6.14 of the RF pulsed experiment. Therefore the signal to noise ratio for the impulse experiment with the sample in Fig. 6.4 would be less than 2:1. For TRANE to measure such an experiment, different samples are required, where there are either larger magnetic fields or larger signal to noise. Since the peak signal occurs for a short time, fine time steps are required. These can be produced by using the marker output of the AWG to generate the magnetic dynamics, since the marker can be delayed with time steps of approximately 1 ps due to an internal digital delay line.

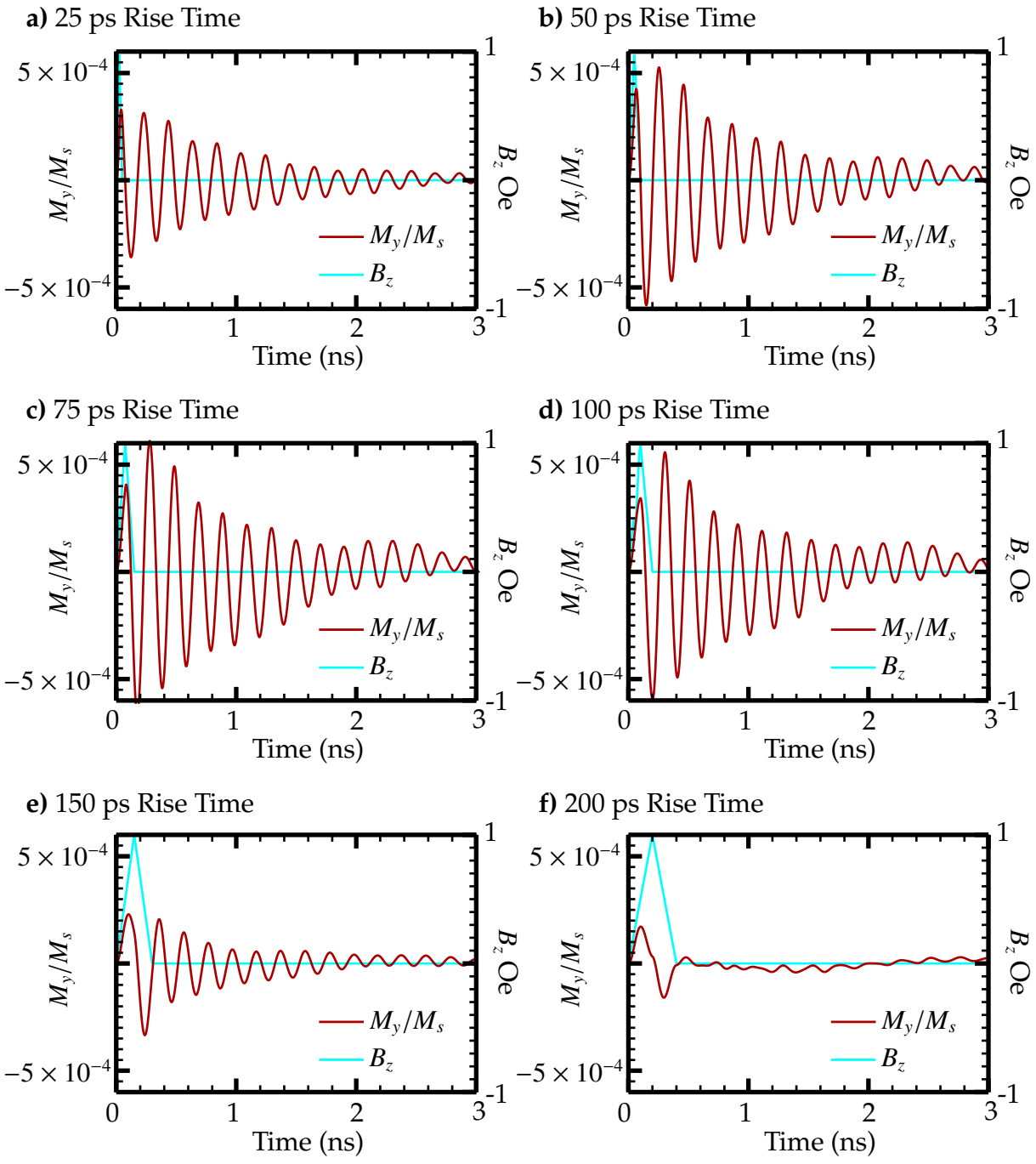

Figure 6.19: OOMMF simulations of the magnetic dynamics induced with a triangular pulse magnetic field of various rise times.

CHAPTER 7

ELECTRICAL DETECTION OF FMR

Ferromagnetic resonance (FMR) is a powerful technique to characterize magnetic materials and devices. FMR can extract characteristics such as the magnetic moment and damping [113]. A prevalent method to measure ferromagnetic resonance is with the anisotropic magnetoresistance (AMR). AMR/FMR electrically measures the oscillating magnetic moment from the voltage that correspondingly oscillates due to the magnetoresistance. There are several subtly different methods to measure FMR through the first-order AMR term, which include ST-FMR [114], Network Analyser [115] and voltage rectification [116]. In this chapter, we discuss the measurement of FMR with voltage rectification and a new method of second harmonic AMR/FMR.

7.1 Anisotropic Magnetoresistance

The anisotropic mangetoresistance (AMR) is a property where the electrical resistivity of the ferromagnetic material is dependent on the direction of the magnetic moment. The electrical resistivity, ρ, of ferromagnetic materials is described by

$$\rho(\theta) = \rho_0 + \Delta\rho \cos^2(\theta(t)), \tag{7.1}$$

where θ is the angle between the magnetization and the current direction, ρ_0 is the resistivity with the magnetic moment is perpendicular to the current, and $\rho_0 + \Delta\rho$ is the resistivity with the magnetic moment parallel to the current. Fig. 7.1 shows the resistance of a 2 μm wide Py wire as a function of the applied field at 45^o to the wire length. From Fig. 7.1, we find an AMR of $\Delta\rho/\rho_0 = 0.02$ at room temperature, consistent with literature values [117]. AMR

arises due to spin-orbit coupling in the ferromagnet; the non-zero total spin of the core-electrons lead to an asymmetrical electron cloud due to the spin-orbit coupling [117, 118, 119]. This leads to scattering rate of the itinerant electrons with the core electrons to be dependent on the direction of the magnetic moment.

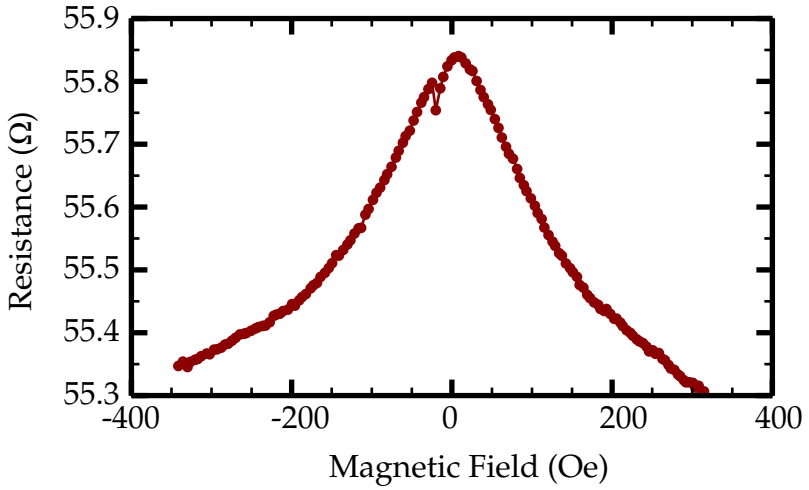

Figure 7.1: The 4 point resistance measurement of a Py sample (2 μ wide and 30 thick) as a function of an applied magnetic field aligned 45^o to the length of the wire.

We measure FMR by using the AMR effect with the voltage across the ferromagnetic wire in the presence of a current such that

$$V(t) = I(t)R(t) = I(t)\left[R_0 + \Delta R \cos^2(\theta(t))\right]. \tag{7.2}$$

For these measurements, we assume the magnetic moment is spatially uniform over the entire sample. The geometry of the sample and the magnetic moment direction are depicted in Fig. 7.2. Working in the small angle limit, where we assume the magnetic precession is small such that $\theta(t) = \theta_0 + \vartheta(t)$, where θ_0 is the angle between the current and the equilibrium position of the magnetic moment and ϑ is the magnetic precession angle such that $\vartheta \ll 1$. We study samples in the

thin film limit, where the thickness dimension is much smaller than the other two dimensions of the sample, we can assume $\vartheta(t) = \beta\cos(\omega t)$. Then the AMR voltage is

$$V(t) = I(t)\left[R_0 + \Delta R\left(\cos^2\theta_0 - \sin(2\theta_0)\beta\cos(\omega t) - \cos(2\theta_0)\beta^2\cos^2(\omega t) + \text{HOT}\right)\right]. \tag{7.3}$$

From Eqn. 7.3, the first order term in β is maximized when $\theta_0 = 45^o$ and the second order term is maximized when $\theta_0 = 0^o$. We will study both of these cases in this chapter.

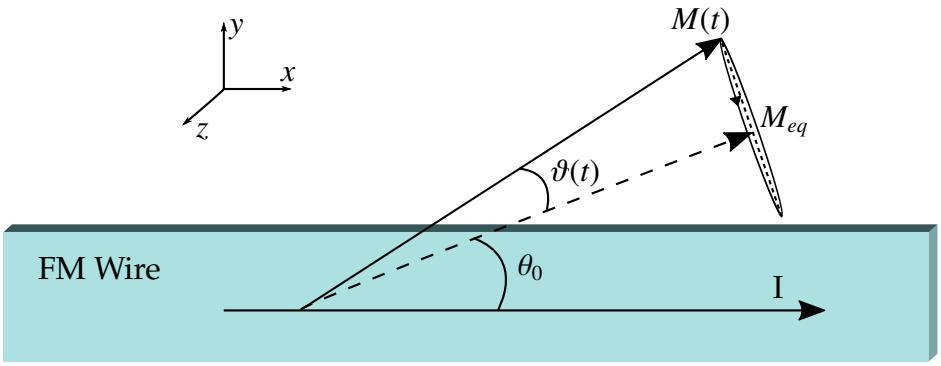

Figure 7.2: The angles of magnetic moment involved with measuring FMR with AMR.

7.2 Electrical Detection with Voltage Rectification

In this section, we will use the voltage rectification method to measure FMR/AMR. As with all first-order FMR/AMR measurements, the magnetic wire needs to be aligned such that the equilibrium magnetic moment is not parallel to the magnetic wire, due to the $\sin(2\theta_0)$ coefficient in Eqn. 7.3. To drive FMR in our samples, we apply an AC current to the stimulation wire. Due

to the inductive coupling between the stimulation wire and magnetic wire, an electrical current is induced in the magnetic wire at the same frequency as the applied AC current. Therefore, $I(t) = I_0 \cos(\omega t + \varphi)$, where the phase is due to the response of the ferromagnetic wire, and is frequency dependent.

Due to the induced current, the DC component of the rectified voltage is

$$V_{DC} = -\left(\frac{I_0 \Delta R}{2}\right) \sin(2\theta_0) \beta \cos(\varphi). \tag{7.4}$$

If the applied static field is large such that

$$H_a \gg M_s N_y, \tag{7.5}$$

we can assume that $\vec{M}_0 \parallel \vec{H}_a$. With such conditions, we can rotate the coordinate system as shown in Fig. 7.3. Using the rotated coordinate system, we can write a new anisotropy constants such that

$$\begin{aligned} N_{x'} &= N_x \cos^2(\theta_0) + N_y \sin^2(\theta_0) \\ N_{y'} &= (N_y - N_x) \sin(\theta_0) \cos(\theta_0). \end{aligned} \tag{7.6}$$

With this description of the rotated coordinate system, we can then describe the effective field along equilibrium magnetic moment position as

$$H_1 = H_0 - M_s N_{x'}. \tag{7.7}$$

Therefore we can see that $\beta \cos(\varphi) = Re[\tilde{m}_{y'} e^{i\varphi}]$ of Eqn.6.20 by setting

$$H_r = \sqrt{\left(H_1 + M_s N_{y'}\right)\left(H_1 + M_s N_z\right)}. \tag{7.8}$$

to give the expression of the rectifying voltage of

$$V = \xi \left(\frac{I_0 \Delta R}{2}\right) \sin(2\theta_0) \left[\cos(\varphi) \left(\frac{1}{1 + \left(\frac{H_1 - H_{r'}}{\Delta H}\right)^2}\right) - \sin(\varphi) \left(\frac{\frac{H_1 - H_{r'}}{\Delta H}}{1 + \left(\frac{H_1 - H_{r'}}{\Delta H}\right)^2}\right)\right], \tag{7.9}$$

where ξ is a numerical constant. Therefore, the voltage rectification measurement of FMR/AMR produces a linear combination of symmetric and antisymmetric Lorentzians, where the phase, φ, is dependent on the inductive response of the magnetic wire.

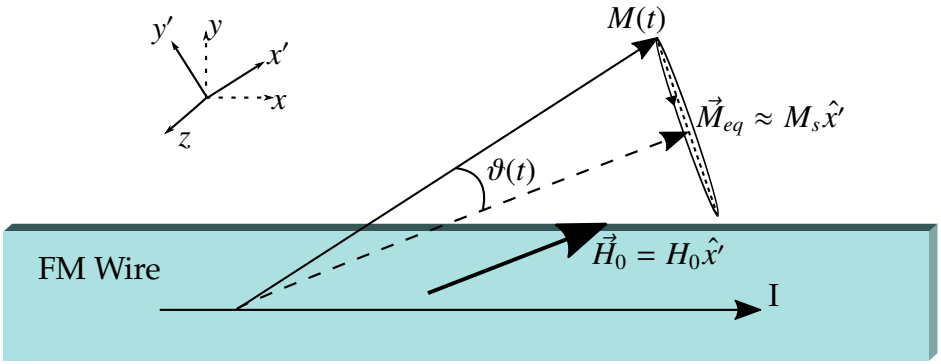

Figure 7.3: The rotated coordinate system for the applied field and equilibrium magnetic moment not aligned to the length of the wire.

7.2.1 Voltage Rectification Setup

Figure 7.4 shows the schematic to measure FMR/AMR with voltage rectification. The sample for measurements of FMR with voltage rectification is the same sample as the one tested for the TRANE magnetic dynamics measurements in the previous chapter. In the setup, we apply a large magnetic field $H_0 + H_m(t)$, where H_m is the modulating component is sinusoidal with an amplitude of 6 Oe and frequency of 800 Hz. The lock-in amplifier uses the modulating field as the reference for demodulation. To maximize the signal, we align the sample so that the applied field is 45^o to the length of the ferromagnetic wire.

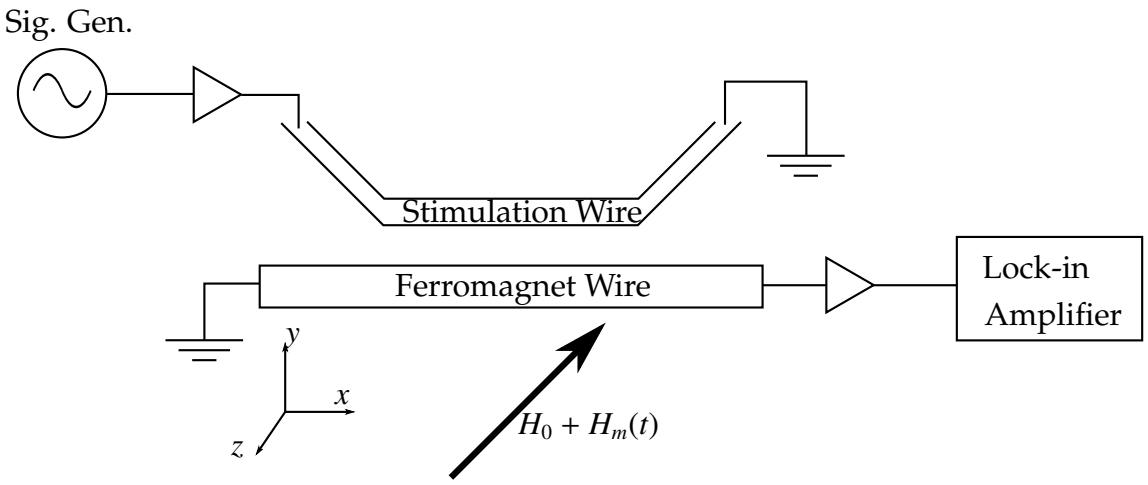

Figure 7.4: The schematic to measure FMR/AMR with voltage rectification.

7.2.2 Voltage Rectification Results

Figure 7.5 shows the measurement at 10 GHz. From the previous chapter, since $M_s N_y = 160$ Oe, we can approximate the magnetic moment is aligned to the applied static field direction. Therefore, we can fit the data to Eqn. 7.9, where ξ, φ, $H_{r'}$, and ΔH are free variables. From the fit, we find for 10 GHz the resonant field is 959 Oe, with a linewidth of 38.4 Oe. Since the linewidth is related to the damping through $\Delta H = \alpha\omega/\gamma$, we measure a damping of 0.01 ± 0.0002 in the Py sample. This matches the damping measured with TRANE for the same sample.

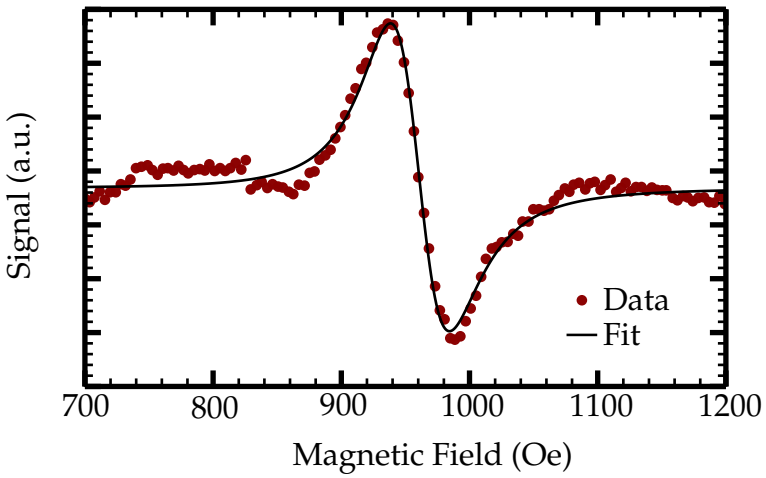

Figure 7.5: Voltage rectification FMR measurements at 10 GHz.

7.3 Electrical Detection with Second Harmonic

An issue with the voltage rectification measurement is that the static field cannot be applied along the length of the wire. Such a geometry would result in zero signal due to the $\sin(2\theta_0)$ coefficient in the first order AMR term. There are situations where it would be advantageous to electrically measure FMR with the field aligned with the wire, such as having a basis to compare the results to the previous chapter. To circumvent this issue, we measure the second order AMR contribution by measuring at a frequency of 2ω, where ω is the driving frequency. Since the signal is at twice the frequency, we call this measurement the 2ω AMR measurement. An advantage for this technique is that it removes other potential contributions to the signal that can occur in a DC measurement, such as spin pumping [20].

7.3.1 2nd Harmonic FMR Detection Setup

To demonstrate the 2ω FMR/AMR technique, we study Py wires, which were grown on the same wafer as the sample in the previous chapter, except we measure wires of widths w = 750 nm and of 30 nm thick. A micrograph of this sample is shown in Fig. 7.6. The thinner wires were chosen due to the better coupling to produce a cleaner plot. Similarly, to stimulate FMR with an out-of-plane magnetic field from a copper stripline 1 μm away from the Py wire.

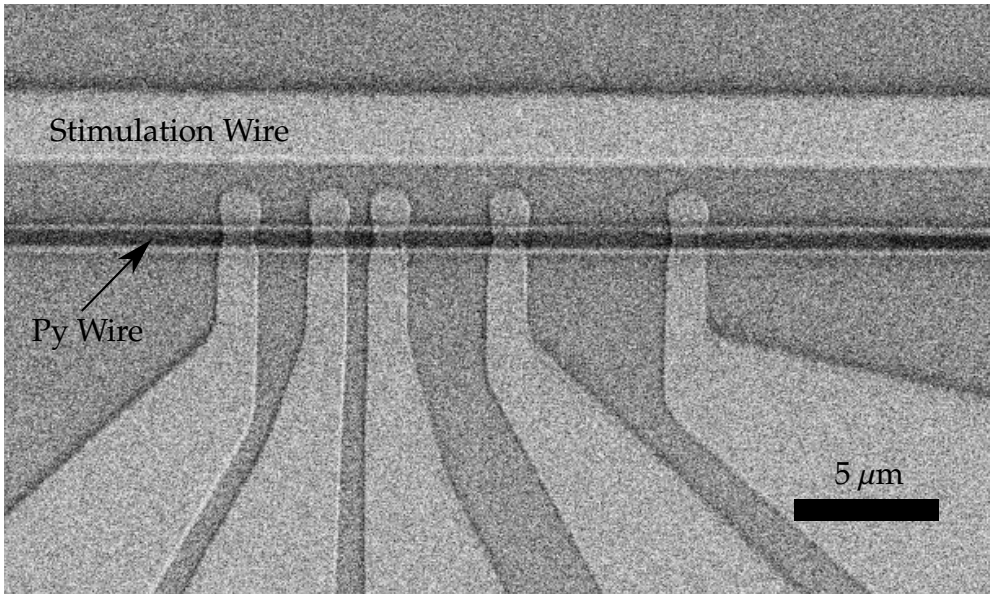

Figure 7.6: Micrograph of the Py sample used to measure 2ω FMR.

A schematic of our measurement technique is shown in Figure 7.7. An RF signal from a signal generator is split. One output from the splitter goes into the stripline generate out-of-plane magnetic fields. The other output from the splitter goes into a frequency doubler and is used as the reference in a frequency mixer. With a bias-tee, the applied current to the ferromagnetic wire is modulated at low frequency relative to the signal generator (1 kHz) to measure the 2ω

AMR signal in the lock-in. The sample is placed in an external magnetic field aligned parallel to the wire. The signal that is measured is the 2ω spectral component of the voltage. By measuring the 2ω spectral component of the voltage, we eliminate the background voltage from cross-talk between the stripline and the Py wire due to inductive coupling.

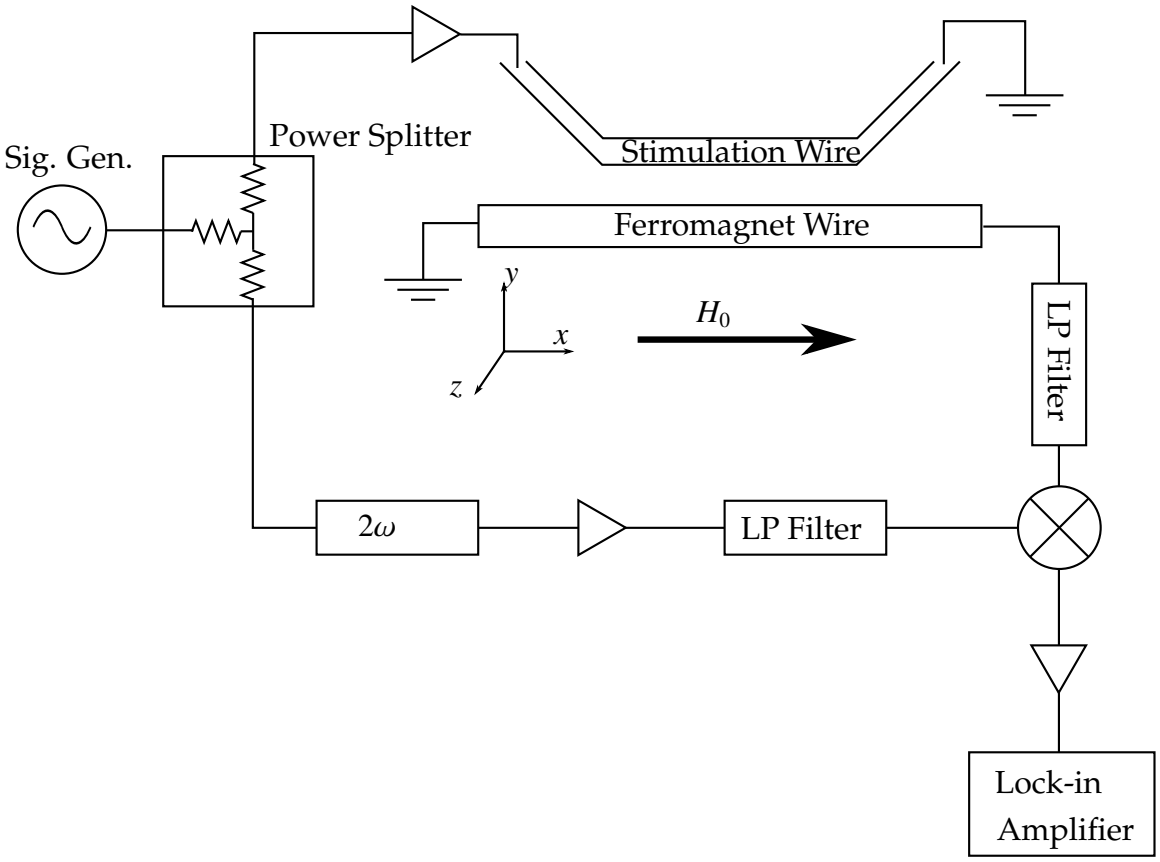

Figure 7.7: The schematic of the 2ω FMR/AMR setup.

7.3.2 2nd Harmonic FMR Dectection Theory

By measuring the 2ω spectral component of the voltage, we can extract the FMR/AMR signal. From Eqn. 7.3, voltage across the ferromagnetic wire in the

presence of an applied current can be written as

$$V(t) = I(t)\Big[R_0 + \Delta R\Big(\cos^2\theta_0 - \sin(2\theta_0)\beta\cos(\omega t) - (1/2)\cos(2\theta_0)\beta^2(\cos(2\omega t) + 1) + \text{HOT}\Big)\Big], \tag{7.10}$$

such that $I(t) = I_{DC} + I_0\cos\omega t + \varphi$, where the first term is the applied DC current and the second term is the induced current due to the coupling as previously discussed. We consider the geometry that maximizes the second order AMR contribution, where the the length of the wire is aligned to the applied magnetic field, which leads to $\theta_0 = 0$, and $\beta \approx \text{Re}[\tilde{m}_y]/M_s$. With the frequency mixer, we measure the Fourier component of the voltage at 2ω, $\tilde{V}(\omega = 2\omega_0)$, defined by

$$\tilde{V}(\omega = 2\omega_0) = \frac{1}{T}\text{Re}\left[\int_T dt\ V(t)\ e^{-i\omega(t+\delta)}\right]_{\omega=2\omega_0} \tag{7.11}$$

where δ is the relative phase delays of the two inputs into the mixer, caused by the circuitry. Applying the geometry of the setup and Eqn. 7.10 to the mixer output voltage, we get the following signal from the frequency mixer:

$$\tilde{V}(\omega = 2\omega_0) = \frac{I\Delta R\cos(2\theta_0)}{2M_s^2}\text{Re}\left[\tilde{m}_y^2 e^{-i2\omega_0\delta}\right]. \tag{7.12}$$

Therefore, we measure a linear combination of the real and imaginary parts of $\tilde{m}_y^2$. From Eqn. 6.20, we find $\tilde{m}_y^2$ to be

$$\tilde{m}_y^2 = A^2\left(\frac{1 - \left(\frac{H_0 - H_r}{\Delta H}\right)^2}{\left[1 + \left(\frac{H_0 - H_r}{\Delta H}\right)^2\right]^2} + i\frac{2\left(\frac{H_0 - H_r}{\Delta H}\right)}{\left[1 + \left(\frac{H_0 - H_r}{\Delta H}\right)^2\right]^2}\right)\tilde{h}_z^2. \tag{7.13}$$

Using this expression for $\tilde{m}_y^2$ and Eqn. 7.12, we can fit to the 2ω signal. Note that from Eqn. 7.12 we can see if a delay line was implemented, the technique is phase sensitive. This is unlike the FMR rectifying voltage measurement where the phase is set due to the magnetic material response.

7.3.3 2nd Harmonic FMR Detection Results

We measure FMR with the 2ω technique by setting a driving frequency and sweeping the magnetic field. Fig. 7.8 shows the 2ω signal as a function of the magnetic field. The red datapoints correspond to the sweep starting from a large saturating field from the negative direction while the blue datapoints correspond to starting from a positive field. From the plots, we can see that the two curves are shifted with respect to one another and are mirror reflection of each other about zero field.

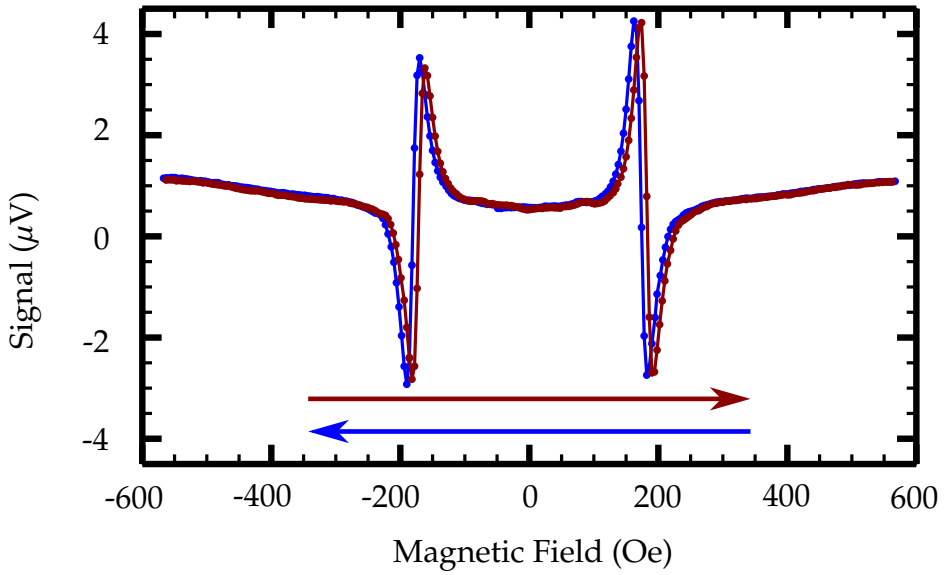

Figure 7.8: The 2ω measured signal as a function of the magnetic field sweep at 5 GHz.

To study this shift in greater detail, we perform fits of both 5 GHz scans in Fig. 7.9. The fits are performed with the amplitude, φ, H_r and ΔH as the free parameters. We see that the sweep starting from high fields has a lower resonant field than the sweep starting from zero. This feature is seen for the nega-

tive fields and also for all other frequencies tested. Since this measurement is non-local, it measures over the entire sample. This suggests possible spatially varying magnetic features at the edge of the sample due to the magnetic switching passing 0 field. Measurements of magnetic hysteresis with TRANE do not show any measurable hysteresis. Due to the small width of the sample, we are unable to measure possible spatial variations of magnetic hysteresis. This could be a future measurement with higher resolution TRANE.

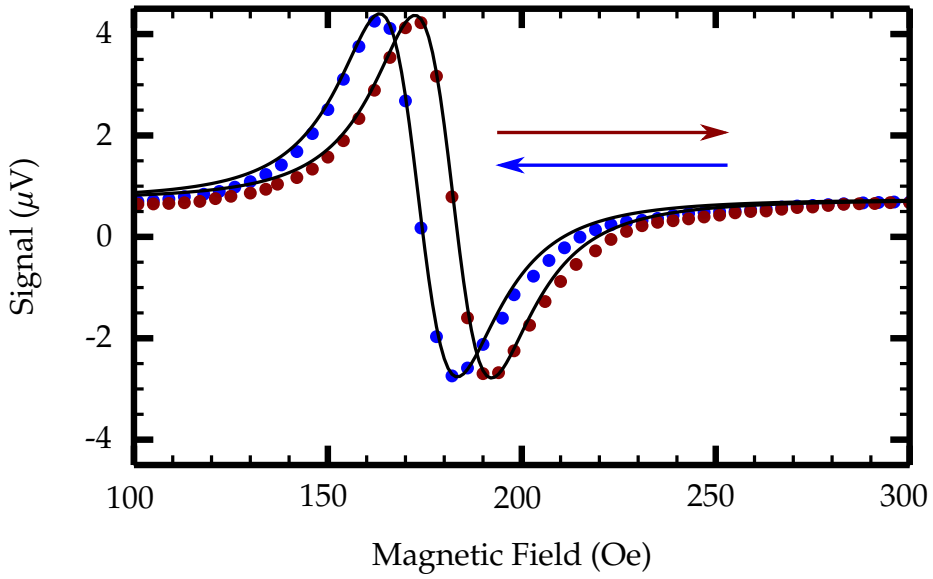

Figure 7.9: Fits of the 2ω measurement of FMR at 5 GHz.

To measure the effective saturating magnetization for the two scans, we plot the FMR frequency as a function of the applied field in Fig. 7.10. The blue curve corresponds to starting the resonant field measured by starting from a high saturating magnetic field, where as the red curve corresponds to starting from zero magnetic field. Applying the expression of the Kittel FMR frequency in Eqn. 6.23, we find $M_s = 761 \pm 1$ from scans starting at zero field and $M_s = 778 \pm 1$

starting with high fields. The smaller effective saturating magnetization with starting from zero fields suggests that the magnetic moments at the edge are not aligned in the same direction as the magnetic field; unlike when starting from a large applied magnetic field, where we expect the magnetic moment of the entire sample to align with the in the same direction as the applied field.

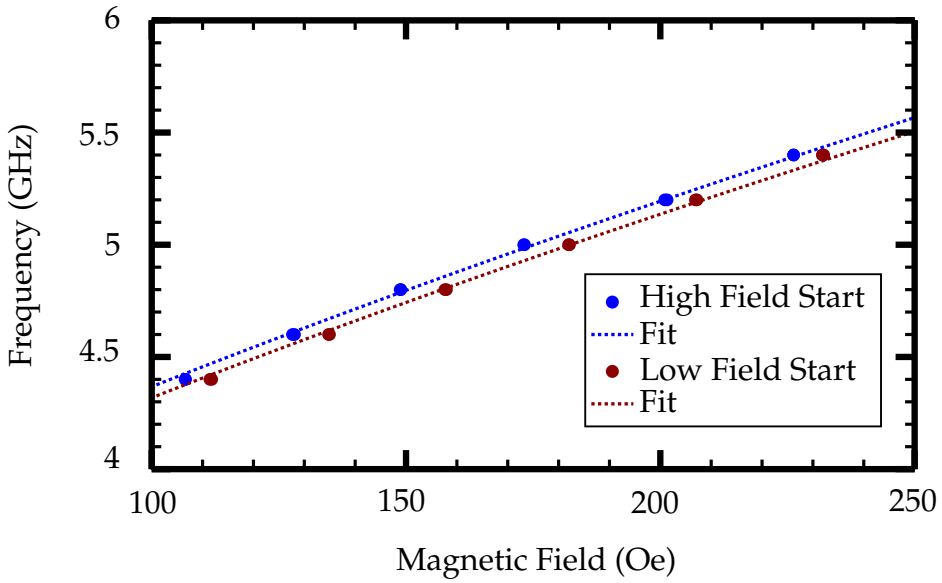

Figure 7.10: The Kittel fit where we plot the FMR frequency as a function of the applied field.

To measure the damping, we fit the linewidth to the data ploted in Fig. 7.11, which shows the linewidth, ΔH as a function of FMR frequency, Applying the expression of the linewdith, $\Delta H = 2\pi\alpha f/\gamma$, to fit the data, we measure a damping parameter of $\alpha = 0.0102 \pm 0.0001$. The damping measured with 2ω matches the damping measured with FMR/AMR rectifying voltage and also the TRANE measurements, which were also measured on the Py grown on the same wafer. This shows that all three measurements are consistent with each other.

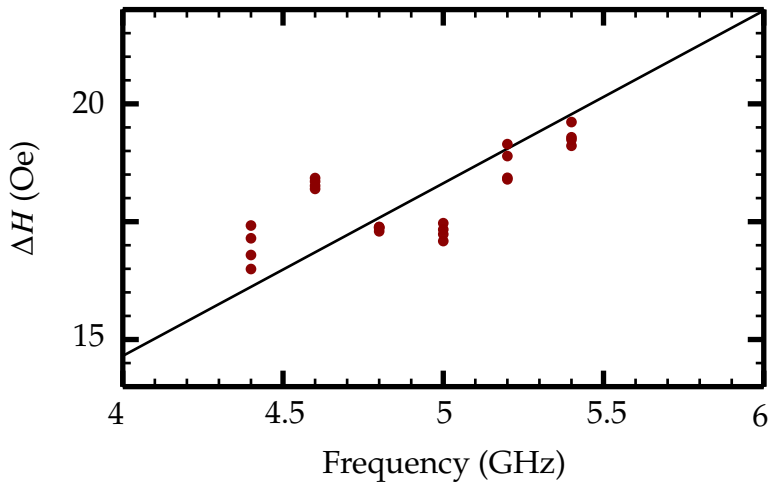

Figure 7.11: The linewidth as a function of the frequency, $\alpha = 0.0102 \pm 0.0001$.

In conclusion, we show that the 2ω FMR/AMR method can measure FMR where the applied field is applied along the length of the ferromagnetic wire. Other techniques that measure the first order contribution from AMR cannot measure in this geometry because the first order contribution is zero when the magnetic moment equilibrium position is aligned with the current. This allows us to make direct comparisons to other experiments where it is advantageous to align the applied field along the length of the wire. Since the 2ω method is a homodyne measurement at twice the driving frequency, it can remove DC voltage artifacts that may occur in certain systems. Also, since the mixing occurs at a electrical mixer, and not in the sample, the technique is phase sensitive unlike other FMR/AMR techniques. The disadvantages with the 2ω measurement is the small signal associated with the second order term and the difficulties involved with higher frequency measurements due to limited bandwidth. Accessing high bandwidths are difficult since we measure at twice the frequecy, this requires the microwave electronics to be suitable to measure at twice the

driving frequency.

CHAPTER 8

MEASUREMENT OF TEMPERATURE INCREASE AND ANOMALOUS NERNST COEFFICIENT

8.1 Background

The interaction between the laser pulse and the sample leads to an increase in temperature at the surface of the sample, creating a time-varying temperature gradient resulting in the anomalous Nernst voltage. In metals, the 794 nm light from the laser interacts with the itinerant electrons raising the total energy of these electrons by the photon energy. These electrons thermalize by interacting with the environment through electron-electron and electron-phonon interactions. These processes have different time scales, leading to describing an electron temperature and lattice temperature. For femtosecond laser pulses, it has been shown that the electron temperature increases dramatically compared to the lattice temperature [120, 121]. For the picosecond laser pulses we use in the TRANE measurement, we assume that the electron-phonon interaction time constant is shorter than the pulse leading to an equal electron and lattice temperatures [100].

The time-varying temperature increase results in a time-varying resistance due to the temperature dependence of the resistance. Since we assume that the electron and lattice temperatures are equal, the time-varying resistance can be expressed as $R(T(t))$, where $T(t)$ is the time-varying temperature of the sample. Since the heating is due to the laser pulse, we expect the time-scale for the resistance increase is of the same order of magnitude as the TRANE signal. Therefore, in the presence of a current in the sample, the time-varying resistance

will produce a time-varying voltage that will be measured in the TRANE setup. This is the source of the large background signal from the FMR measurements due to the inductive cross-talk current. This background signal can be isolated from the TRANE signal by modulating the applied current and measuring with a lock-in at the modulation frequency.

8.2 Experimental Measurement of Resistance Increase

In this chapter, we measure the temperature increase and the resulting resistance increase in the 2 μm wide, 30 nm thick permalloy sample as discussed in Chap. 6. When the laser induces a temperature increase to create the TRANE signal, it also creates an increase in the local resistance. If there is electrical current in the sample, the resistance change creates an additional voltage contribution that is independent of the sample magnetization. In this section, we use the signal from the local resistance change to measure the temperature profile of the sample due to heating from the laser. We determine the local resistance change by measuring the signal dependence on an applied DC electrical current. The DC current is applied to the sample by introducing a bias-tee into the circuit as shown in Fig. 8.1a. To show the relationship between the resistance change and the measured voltage, we begin with the sample voltage, which is given by

$$V_{\text{sample}}(t) = V_{\text{ANE}}(t) + I(t)\,R(t), \tag{8.1}$$

where V_{ANE} is the voltage from the anomlaous Nernst effect and $I(t)\,R(t)$ is the Ohmic voltage. For the current scenario, we set a constant applied current, while the resistance and V_{ANE} vary in time. From section 3.3.2, we find the volt-

age at the mixer output is given by

$$V_{\text{Mixer}} = \frac{1}{V_0} \sum_{k=-K}^{K} c^{\text{r}}_{-k} \left[c^{\text{ANE}}_{k} + \int_0^T dt\, I_{\text{DC}}\, R(t)\, e^{-i\frac{2\pi kt}{T}} \right]. \tag{8.2}$$

By chopping laser power, the lock-in voltage from the mixer signal, as described by Eq. A.7, is given by

$$V_{\text{LI}} = \frac{1}{V_0} \sum_{n=-N_{\text{max}}}^{N_{\text{max}}} c^{\text{ref}}_{-n} \left[c^{\text{ANE}}_{n} + I_{\text{DC}}\, c^{\Delta R}_{n} \right], \tag{8.3}$$

where $c^{\Delta R}_{n} = \int_0^T dt\, \Delta R(t)\, e^{-i\frac{2\pi nt}{T}}$ is Fourier series component of the change in the resistance, ΔR, from room temperature. We show the results of these measurements in Fig. 8.1b, which displays the expected linear relationship between the collection signal and the applied DC current. We repeat the measurements at various laser powers and plot the slope as a function of laser power in Fig. 8.1c. These measurements were performed in the presence of a large saturating magnetic field, so that we can neglect current induced magnetization effects that may change the anomalous Nernst signal. Therefore, by relating the resistance change to a temperature increase, we can quantitatively determine the heating induced by the laser.

It is non-trivial to directly convert this data into a measure of resistance due to the non-linearity of the circuit components. Instead, we compare this data to numerical simulations and calculations. We numerically simulate the temperature profile to calculate its corresponding resistance change and the resulting collection signal. Due to the unknown absorption coefficient of the sample, there is an uncertainty in the absolute value of the temperature change. Therefore there will be an overall factor which is determined by comparing the simulation results with the measured collection signal. By comparing the slopes of the calculated and measured signals as a function of DC current, we obtain the total temperature change and the temperature gradient.

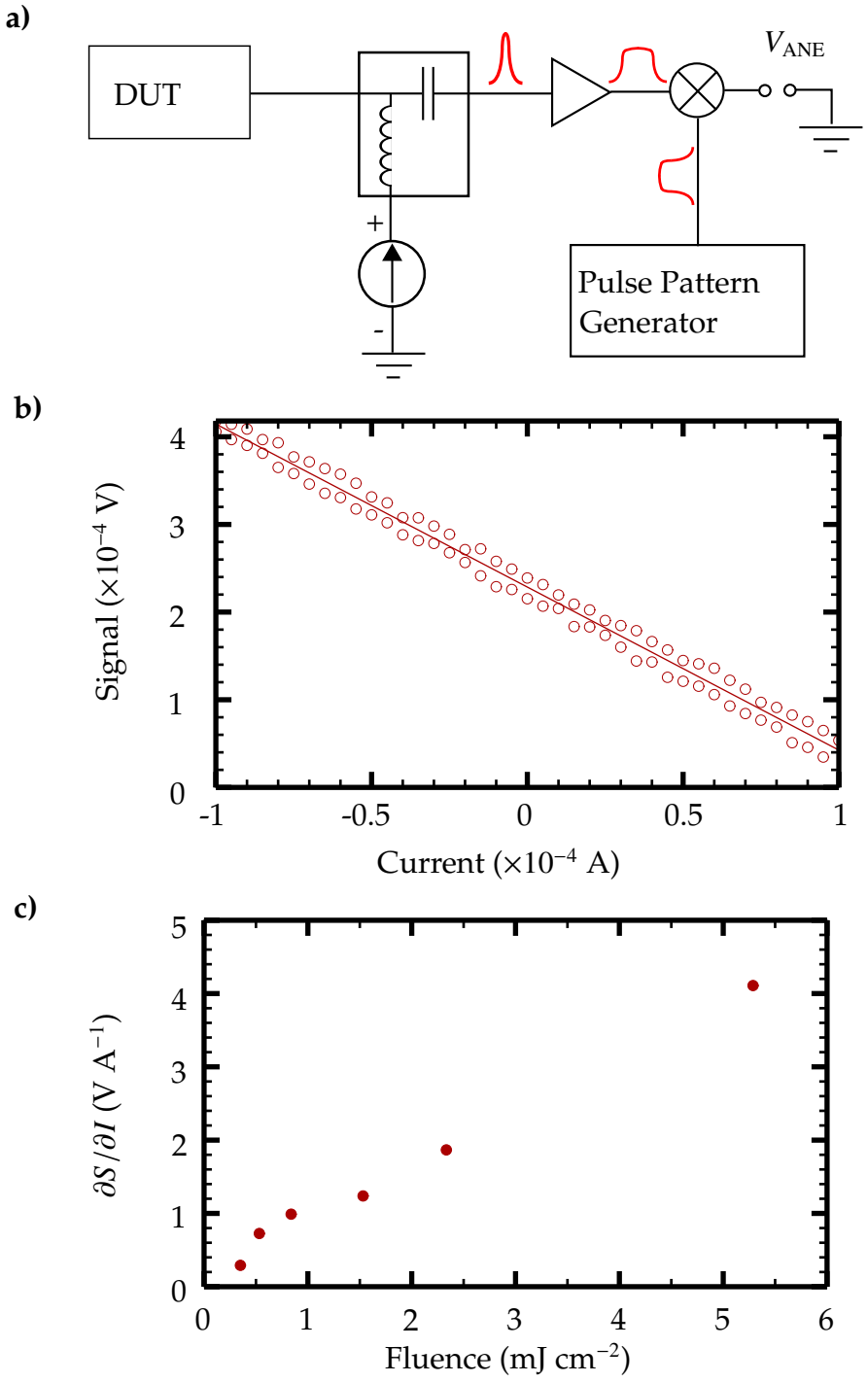

Figure 8.1: a) Circuit setup to measure the temperature induced resistance change. b) The collection signal as a function of the applied DC current to measure the resistance change due to heating from the laser pulse. c) The slope of the collection signal versus applied DC current for various laser powers.

8.3 Temperature Dependence of Resististivity

We measure the temperature dependence of resistivity to map the simulated temperature profile to a total resistance change. We consider the linear response regime of the resistivity dependence on temperature, such that

$$\rho(T) = \rho_0 \left[1 + \alpha(T - T_0)\right] = \rho_0 \left[1 + \alpha \Delta T\right] \tag{8.4}$$

where ρ_0 is the resistivity at the base temperature T_0, which we set as room temperature at 293 K, and α is the temperature coefficient of resistivity. To determine the temperature coefficient of resistivity, we measure the 4-point resistance as a function of temperature with a Physical Property Measurement System (PPMS), with the results shown in Fig. 8.2. With the 4-point resistance measurement, we remove contributions due to contact resistance, therefore the resistivity is related to the resistance, R, by

$$\rho = \frac{RA}{L} \tag{8.5}$$

where A is the cross-sectional area and L is the length between the measurement probes. By fitting the data in Fig. 8.2, we find the temperature coefficient of resistance in the 30 nm Permalloy to be $\alpha = 0.00243\ \Omega/K$, which is similar to literature values [122].

8.4 Resistance Temporal Profile

We calculate the total time-varying resistance induced from laser heating by mapping the numerically simulated temperature profile to a resistivity profile using the measured resistivity versus temperature. The total resistance of the

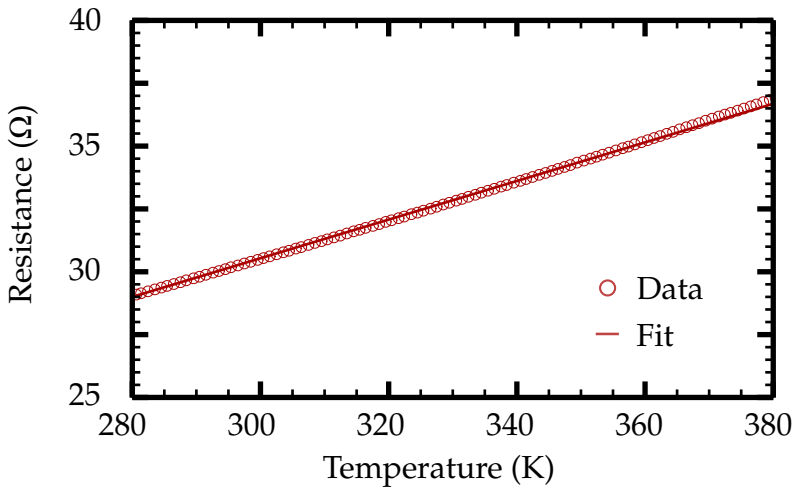

Figure 8.2: With the PPMS, we measure the temperature dependence of the resistance of a 30 nm thick permalloy sample.

sample in terms of the spatially dependent resistivity is given by

$$R(t) = \left[\int dxdy \left[\int dz\, \rho(T(\vec{x}), t) \right]^{-1} \right]^{-1}, \tag{8.6}$$

where $\rho(T(\vec{x}))$ is the temperature dependent resistivity. Applying the linear temperature dependence of the resistivity gives

$$R(t) = \left[\int dxdy \left[\int dz\, \rho_0(1 + \alpha\, \Delta T(\vec{x}, t)) \right]^{-1} \right]^{-1}. \tag{8.7}$$

From the measurements of the resistivity temperature dependence, it is safe to assume $\alpha\Delta T \ll R_0$, where R_0 is the resistance at T_0. Therefore, we find the total resistance change by performing a series expansion and taking the first order term to be

$$\Delta R(t) = R_0 \int^V \frac{d\vec{x}}{V}\, \alpha\, \Delta T(\vec{x}, t). \tag{8.8}$$

This shows that the total resistance change is proportional to the mean temperature change through the length of the wire. Fig. 8.3 shows the calculated total resistance change as a function of time for the simulated temporal profile from Fig. 5.6.

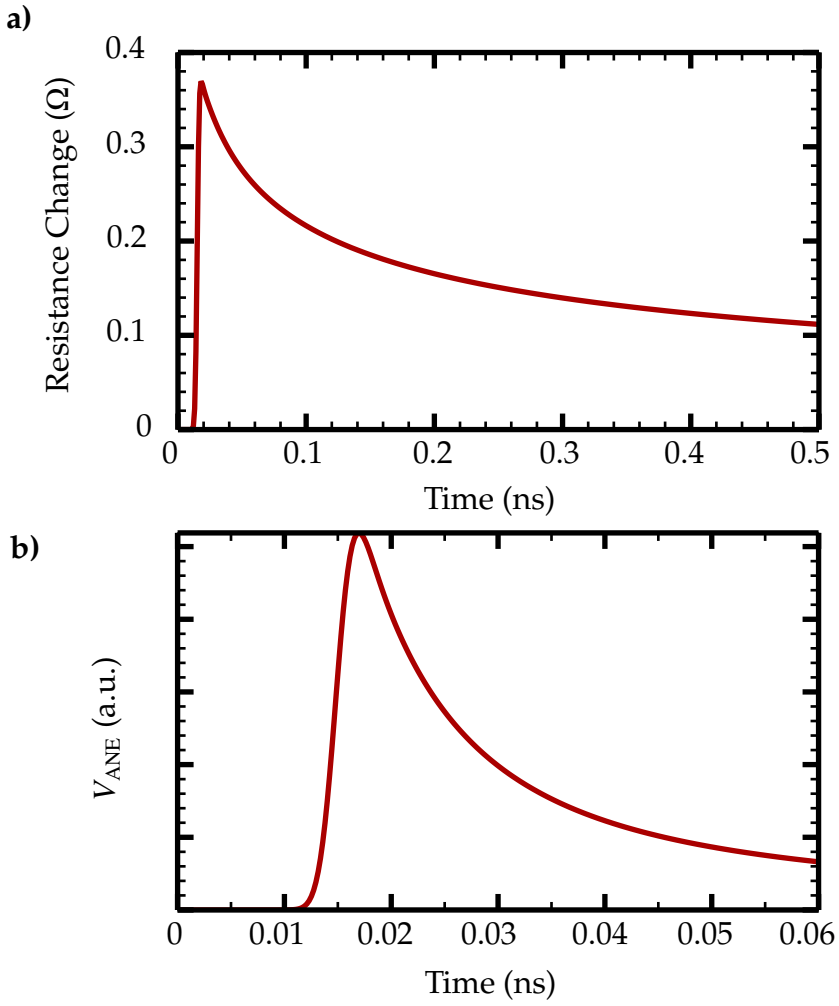

Figure 8.3: **a)** The time dependence of the resistance change due to laser heating. **b)** The time dependence of the anomalous Nernst voltage pulse, V_{ANE}.

We note from Fig. 8.3 that the decay time scale for resistance change is much larger than the TRANE signal. This is because the anomalous Nernst voltage is dependent on the vertical component of the temperature gradient while the resistance change is dependent on the overall mean temperature. Therefore, lateral thermal diffusion from the heat source into other regions of the ferromagnet will reduce the vertical thermal gradient, causing the decay in the anomalous

Nernst voltage. Conversely, lateral thermal diffusion has less influence on the overall mean temperature, and thus the total resistance changes more slowly.

8.5 Temperature Dependence on Laser Power

We determine the temperature profile by scaling the simulated temperature profile in Fig. 5.6 to match the measured signal slope in Fig. 8.4. This matching is done by taking into account the bandwidth and the collection circuit transfer coefficient as described in Sec. 3.3.3. For the typical laser fluence used of 2.3 mJ cm^{-2}, we determine a dimensionless scaling factor of 0.4. Physically, this scaling factor accounts for the unknown optical absorption coefficient. Using this factor we calculate a resulting maximum temperature increase of 60 K and a corresponding maximum gradient of 4.0×10^8 K m^{-1}. This is $\sim$ 100 times greater that the value of $\sim 1 \times 10^6$ K m^{-1} quoted for a CW laser [53]. This highlights the distinction between pulsed and CW laser measurements. We show the maximum temperature increase for various laser fluences in Fig. 8.4. The linearity of temperature increase as a function of laser fluence suggests that the heating from the laser is in the linear response regime.

8.6 Anomalous Nernst Coefficient

By comparing the measured hard-axis TRANE hysteresis with the simplified resistor model, we measure an anomalous Nernst coefficient of $2.7 \pm 0.3 \times 10^{-7}$ V K^{-1} T^{-1}. This value has the same order within an order of magnitude as reported in the literature [73, 53, 74]. There is no consensus value because the anomalous

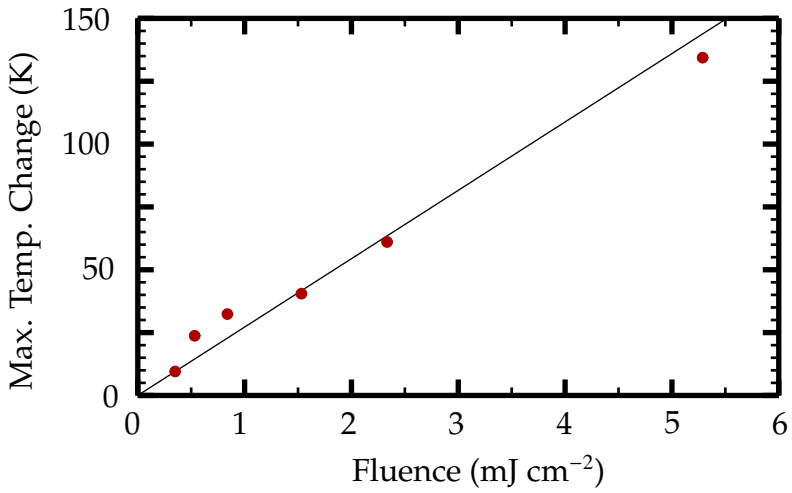

Figure 8.4: The maximum temperature increase at various laser fluences.

Hall coefficient for permalloy, which is related to the anomalous Nernst effect through the Seebeck coefficient, is highly dependent on the thickness and resistivity [123]. Rather than using the simplified resistor model, a more accurate calculation could be performed through finite element method simulations to predict the resulting current due to the anomalous Nernst effect as suggested in Sec. 2.4

This suggests that TRANE is a viable technique to measure the anomalous Nernst coefficient in materials without specialized thermal measurement apparatus. The error bars for this measuremente anomalous Nernst coefficient include accounts for errors from the experimental error in the transfer coefficient and the timing of the mixing pulse. It has ignored the uncertainty of values used in the numerical simulation, which include the laser pulse temporal profile and the material parameters. These errors would change the overall scaling factor used to predict the temperature and anomalous Nernst coefficients, but it does not influence the technique to measure possible variations within the sample.

APPENDIX A

VOLTAGE CALCULATION

A.1 Lock-in Voltage

Lock-in amplifiers are capable of measuring small signals in the presence of large background noise through homodyne detection. By modulating the signal, the signal is at a higher frequency, thus the $1/f$ noise is reduced. With homodyne detection, the collection bandwidth is be reduced to approximately the inverse of the time constant.

The voltage measured in the lock-in, $V_{\text{lock-in}}$, from a time varying signal, V_{signal}, is given by:

$$V_{\text{lock-in}} = 2f \int_0^{1/f} dt\ V_{\text{signal}}\ \sin(2\pi f t + \phi) \tag{A.1}$$

where the frequency, f, and phase shift, ϕ, are set by the user. Let us assume the signal voltage is dependent on a variable $a(t)$. By varying $a(t)$ at the lock-in frequency f will allow the signal to be measured with the lock-in homodyne detection. There are two common methods to vary $a(t)$, either by modulating it with a sine wave or chopping with square waves. We will discuss the resulting lock-in voltage due to the two methods.

A.1.1 Signal Modulation

By modulating the variable with a sine wave, we set

$$a(t) = a_0 + a_1 \sin(2\pi f t). \tag{A.2}$$

If we work in the linear response regime, the signal voltage can then be expressed as

$$V_{\text{signal}} = V(a(0)) + a_1 \cos(2\pi f t) \left.\frac{\partial V}{\partial a}\right|_{a_0}. \tag{A.3}$$

By applying this voltage into Eq. A.1, the measured lock-in voltage is

$$V_{\text{lock-in}} = a_1 \left.\frac{\partial V}{\partial a}\right|_{a_0}. \tag{A.4}$$

Therefore, by modulating in the linear regime, the lock-in voltage measures the derivative of the signal.

A.1.2 Signal Chopping

If we chop the variable with a square wave, we set

$$a(t) = a_0 + a_1 \left[\text{sgn}(\sin(2\pi f t)) + 1\right]/2. \tag{A.5}$$

The signal voltage can be expressed in terms the cases of

$$V_{\text{signal}} = \begin{cases} V(a_0 + a_1) & \text{if } \sin(2\pi f t) > 0 \\ V(a_0) & \text{if } \sin(2\pi f t) < 0. \end{cases} \tag{A.6}$$

By applying the chopped signal into Eq. A.1, the measured lock-in voltage is

$$V_{\text{lock-in}} = \frac{2}{\pi}\left[V(a_0 + a_1) - V(a_0)\right]. \tag{A.7}$$

A.1.3 Dual Demodulation

For situations where there are multiple contributions to the total voltage signal, where each contribution comes from a different effect, we can measure individual components by modulating multiple variables at different frequencies.

By modulating two variables at different frequencies and demodulating both frequencies, we can measure specific contributions to the total voltage. For example, let us say that there are three contributions to the total voltage, V_1, V_2, and V_3, which depend on variables A and B as such

$$V_{signal}(t) = V_1(A,t) + V_2(A,B,t) + V_3(B,t). \tag{A.8}$$

From $V(t)$, we can measure V_2 by modulating both A and B, where

$$A(t) = A_0 + A_1\cos(\omega_A t), \tag{A.9}$$

and similarly

$$B(t) = B_0 + B_1\cos(\omega_B t), \tag{A.10}$$

such that $\omega_A \gg \omega_B$. From Eqn. A.1, by first demodulating the higher frequency variable, A, we have

$$V_{LI1}(t) = \frac{2}{T_A}\int_{t-T_A}^{t} d\tau\ V_{signal}(\tau)\ \sin\left(\omega_A\tau + \phi_A\right), \tag{A.11}$$

where the period is $T_A = 1/(2\pi\omega_A)$. Since only V_1 and V_2 are dependent on A, as described in Eqn. A.4, the first demodulated signal is

$$V_{LI1}(t) = A_1\left(\left.\frac{\partial V_1}{\partial A}\right|_{A_0}(t) + \left.\frac{\partial V_2}{\partial A}\right|_{A_0}(B(t),t)\right). \tag{A.12}$$

Since $\omega_A \gg \omega_B$, it is safe to assume that B is constant over the period T_A. For the second demodulation, we take the first demodulated signal and demodulate with ω_B such that

$$V_{LI2} = \frac{2}{T_B}\int_{t-T_B}^{t} d\tau\ V_{LI1}(\tau)\ \sin\left(\omega_B\tau + \phi_B\right), \tag{A.13}$$

where similarly $T_B = 1/(2\pi\omega_B)$. The contribution of V_1 to V_{LI1} is independent of B thus we have the expression of

$$V_{LI2} = A_1 B_1\left.\frac{\partial^2 V_2}{\partial A\partial B}\right|_{A_0,B_0}. \tag{A.14}$$

By modulating both variables A and B, we can measure only contributions to the total signal that are dependent on both A and B.

Similarly, if instead of modulating A, we can chop it such that

$$A(t) = A_0 + A_1 \left[\mathrm{sgn}(\sin(\omega_A t)) + 1\right]/2. \tag{A.15}$$

Here, we assume each of the chopping of A causes the voltage contributions to the total signal turn on and off such that

$$V_1(A = A_0, t) = 0 \tag{A.16}$$

and

$$V_2(A = A_0, B(t), t) = 0. \tag{A.17}$$

With these assumptions, following the previous procedure, the demodulated singal is given by

$$V_{LI2} = \left(\frac{2}{\pi} B_1\right) \left.\frac{\partial V_2}{\partial B}\right|_{A=A_0+A_1, B=B_0}. \tag{A.18}$$

BIBLIOGRAPHY

[1] W. Heitler and F. London, "Wechselwirkung neutraler Atome und homopolare Bindung nach der Quantenmechanik," *Zeitschrift fr Physik*, vol. 44, pp. 455–472, June 1927.

[2] M. N. Baibich, J. M. Broto, A. Fert, F. N. Van Dau, and F. Petroff, "Giant Magnetoresistance of (001)Fe/(001)Cr Magnetic Superlattices," *Physical Review Letters*, vol. 61, pp. 2472–2475, Nov. 1988.

[3] G. Binasch, P. Grünberg, F. Saurenbach, and W. Zinn, "Enhanced magnetoresistance in layered magnetic structures with antiferromagnetic interlayer exchange," *Physical Review B*, vol. 39, pp. 4828–4830, Mar. 1989.

[4] I. Žutić and S. Das Sarma, "Spintronics: Fundamentals and applications," *Reviews of Modern Physics*, vol. 76, pp. 323–410, Apr. 2004.

[5] J. Katine, F. Albert, R. Buhrman, E. Myers, and D. Ralph, "Current-Driven Magnetization Reversal and Spin-Wave Excitations in Co /Cu /Co Pillars," *Physical Review Letters*, vol. 84, pp. 3149–3152, Apr. 2000.

[6] S. Mangin, D. Ravelosona, J. a. Katine, M. J. Carey, B. D. Terris, and E. E. Fullerton, "Current-induced magnetization reversal in nanopillars with perpendicular anisotropy," *Nature Materials*, vol. 5, pp. 210–215, Feb. 2006.

[7] S. I. I. Kiselev, J. C. C. Sankey, I. N. N. Krivorotov, N. C. Emley, R. J. Schoelkopf, R. A. Buhrman, and D. C. Ralph, "Microwave oscillations of a nanomagnet driven by a spin-polarized current," *Nature*, vol. 425, pp. 1207–1210, Sept. 2003.

[8] A. M. Deac, A. Fukushima, H. Kubota, H. Maehara, Y. Suzuki, S. Yuasa, Y. Nagamine, K. Tsunekawa, D. D. Djayaprawira, and N. Watanabe, "Bias-driven high-power microwave emission from MgO-based tunnel magnetoresistance devices," *Nature Physics*, vol. 4, pp. 803–809, Aug. 2008.

[9] Y. Kajiwara, K. Harii, S. Takahashi, J. Ohe, K. Uchida, M. Mizuguchi, H. Umezawa, H. Kawai, K. Ando, K. Takanashi, S. Maekawa, and E. Saitoh, "Transmission of electrical signals by spin-wave interconversion in a magnetic insulator.," *Nature*, vol. 464, pp. 262–266, Mar. 2010.

[10] Http://www.businesswire.com/news/home/20131118005368/en/Everspin-ST-MRAM-Incorporated-Cache-Memory-Buffalo-

Memory#.VcpxmCZViko, "Everspin ST-MRAM Incorporated for Cache Memory Into Buffalo Memory SSD — Business Wire."

[11] M. R. Freeman and B. C. Choi, "Advances in magnetic microscopy.," *Science (New York, N.Y.)*, vol. 294, pp. 1484–1488, Nov. 2001.

[12] S. S. P. Parkin, M. Hayashi, and L. Thomas, "Magnetic domain-wall racetrack memory.," *Science (New York, N.Y.)*, vol. 320, pp. 190–4, Apr. 2008.

[13] S. Mühlbauer, B. Binz, F. Jonietz, C. Pfleiderer, A. Rosch, A. Neubauer, R. Georgii, and P. Böni, "Skyrmion lattice in a chiral magnet.," *Science (New York, N.Y.)*, vol. 323, pp. 915–9, Feb. 2009.

[14] X. Z. Yu, Y. Onose, N. Kanazawa, J. H. Park, J. H. Han, Y. Matsui, N. Nagaosa, and Y. Tokura, "Real-space observation of a two-dimensional skyrmion crystal.," *Nature*, vol. 465, pp. 901–904, June 2010.

[15] K. Shibata, X. Z. Yu, T. Hara, D. Morikawa, N. Kanazawa, K. Kimoto, S. Ishiwata, Y. Matsui, and Y. Tokura, "Towards control of the size and helicity of skyrmions in helimagnetic alloys by spin-orbit coupling.," *Nature nanotechnology*, vol. 8, pp. 723–8, Oct. 2013.

[16] C. Kittel, "On the Theory of Ferromagnetic Resonance Absorption," *Physical Review*, vol. 73, pp. 155–161, Jan. 1948.

[17] C. Herring and C. Kittel, "On the Theory of Spin Waves in Ferromagnetic Media," *Physical Review*, vol. 81, pp. 869–880, Mar. 1951.

[18] J. VAN KRANENDONK and J. H. VAN VLECK, "Spin Waves," *Reviews of Modern Physics*, vol. 30, pp. 1–23, Jan. 1958.

[19] Y. Tserkovnyak, A. Brataas, and G. E. W. Bauer, "Spin pumping and magnetization dynamics in metallic multilayers," *Physical Review B*, vol. 66, p. 224403, Dec. 2002.

[20] M. V. Costache, M. Sladkov, S. M. Watts, C. H. Van Der Wal, and B. J. Van Wees, "Electrical detection of spin pumping due to the precessing magnetization of a single ferromagnet," *Physical Review Letters*, vol. 97, no. 21, pp. 1–4, 2006.

[21] H.-J. Chia, F. Guo, L. M. Belova, and R. D. McMichael, "Nanoscale Spin

Wave Localization Using Ferromagnetic Resonance Force Microscopy," *Physical Review Letters*, vol. 108, p. 087206, Feb. 2012.

[22] X. Yu, N. Kanazawa, W. Zhang, T. Nagai, T. Hara, K. Kimoto, Y. Matsui, Y. Onose, and Y. Tokura, "Skyrmion flow near room temperature in an ultralow current density," *Nature Communications*, vol. 3, p. 988, 2012.

[23] O. Takeuchi, R. Morita, M. Yamashita, and H. Shigekawa, "Development of time-resolved scanning tunneling microscopy in femtosecond range," *Japanese Journal of Applied Physics, Part 1: Regular Papers and Short Notes and Review Papers*, vol. 41, no. 7 B, pp. 4994–4997, 2002.

[24] M. Faraday, *On the magnetization of light and the illumination of magnetic lines of force*. Royal Society, 1846.

[25] J. Kerr, "XLIII. On rotation of the plane of polarization by reflection from the pole of a magnet," *Philosophical Magazine Series 5*, vol. 3, pp. 321–343, May 1877.

[26] E. D. Palik, "A brief survey of magnetooptics.," *Applied optics*, vol. 6, pp. 597–602, Apr. 1967.

[27] Z. Q. Qiu and S. D. Bader, "Surface magneto-optic Kerr effect," *Review of Scientific Instruments*, vol. 71, p. 1243, Mar. 2000.

[28] E. Beaurepaire, J.-C. Merle, A. Daunois, and J.-Y. Bigot, "Ultrafast Spin Dynamics in Ferromagnetic Nickel," *Physical Review Letters*, vol. 76, pp. 4250–4253, May 1996.

[29] E. Abbe, "Beiträge zur Theorie des Mikroskops und der mikroskopischen Wahrnehmung," *Archiv für Mikroskopische Anatomie*, vol. 9, pp. 413–418, Dec. 1873.

[30] G. Schütz, W. Wagner, W. Wilhelm, P. Kienle, R. Zeller, R. Frahm, and G. Materlik, "Absorption of circularly polarized x rays in iron," *Physical Review Letters*, vol. 58, pp. 737–740, Feb. 1987.

[31] Y. Acremann, J. Strachan, V. Chembrolu, S. Andrews, T. Tyliszczak, J. Katine, M. Carey, B. Clemens, H. Siegmann, and J. Stöhr, "Time-Resolved Imaging of Spin Transfer Switching: Beyond the Macrospin Concept," *Physical Review Letters*, vol. 96, p. 217202, May 2006.

[32] W. Chao, B. D. Harteneck, J. A. Liddle, E. H. Anderson, and D. T. Attwood, "Soft X-ray microscopy at a spatial resolution better than 15 nm.," *Nature*, vol. 435, pp. 1210–3, June 2005.

[33] D.-H. Kim, P. Fischer, W. Chao, E. Anderson, M.-Y. Im, S.-C. Shin, and S.-B. Choe, "Magnetic soft x-ray microscopy at 15 nm resolution probing nanoscale local magnetic hysteresis (invited)," *Journal of Applied Physics*, vol. 99, p. 08H303, Apr. 2006.

[34] A. Puzic, B. Van Waeyenberge, K. W. Chou, P. Fischer, H. Stoll, G. Schutz, T. Tyliszczak, K. Rott, H. Bruckl, G. Reiss, I. Neudecker, T. Haug, M. Buess, and C. H. Back, "Spatially resolved ferromagnetic resonance: Imaging of ferromagnetic eigenmodes," *Journal of Applied Physics*, vol. 97, p. 10E704, May 2005.

[35] L. Bocklage, B. Krüger, R. Eiselt, M. Bolte, P. Fischer, and G. Meier, "Time-resolved imaging of current-induced domain-wall oscillations," *Physical Review B*, vol. 78, p. 180405, Nov. 2008.

[36] T. Pangaribuan, K. Yamada, S. Jiang, H. Ohsawa, and M. Ohtsu, "Reproducible Fabrication Technique of Nanometric Tip Diameter Fiber Probe for Photon Scanning Tunneling Microscope," *Japanese Journal of Applied Physics*, vol. 31, pp. L1302–L1304, Sept. 1992.

[37] R. Stockle, C. Fokas, V. Deckert, R. Zenobi, B. Sick, B. Hecht, and U. P. Wild, "High-quality near-field optical probes by tube etching," *Applied Physics Letters*, vol. 75, p. 160, July 1999.

[38] E. Betzig, J. K. Trautman, R. Wolfe, E. M. Gyorgy, P. L. Finn, M. H. Kryder, and C.-H. Chang, "Near-field magneto-optics and high density data storage," *Applied Physics Letters*, vol. 61, p. 142, July 1992.

[39] C. Durkan, I. V. Shvets, and J. C. Lodder, "Observation of magnetic domains using a reflection-mode scanning near-field optical microscope," *Applied Physics Letters*, vol. 70, no. 10, p. 1323, 1997.

[40] P. Fumagalli, A. Rosenberger, G. Eggers, A. Munnemann, N. Held, and G. Guntherodt, "Quantitative determination of the local Kerr rotation by scanning near-field magneto-optic microscopy," *Applied Physics Letters*, vol. 72, p. 2803, June 1998.

[41] A. Bek, R. Vogelgesang, and K. Kern, "Apertureless scanning near field

optical microscope with sub-10nm resolution," *Review of Scientific Instruments*, vol. 77, p. 043703, Apr. 2006.

[42] J. Levy, V. Nikitin, J. M. Kikkawa, A. Cohen, N. Samarth, R. Garcia, and D. D. Awschalom, "Spatiotemporal Near-Field Spin Microscopy in Patterned Magnetic Heterostructures," *Physical Review Letters*, vol. 76, pp. 1948–1951, Mar. 1996.

[43] M. Johnson and R. H. Silsbee, "Thermodynamic analysis of interfacial transport and of the thermomagnetoelectric system," *Physical Review B*, vol. 35, pp. 4959–4972, Apr. 1987.

[44] J. Shi, K. Pettit, E. Kita, S. S. P. Parkin, R. Nakatani, and M. B. Salamon, "Field-dependent thermoelectric power and thermal conductivity in multilayered and granular giant magnetoresistive systems," *Physical Review B*, vol. 54, pp. 15273–15283, Dec. 1996.

[45] L. Gravier, S. Serrano-Guisan, F. Reuse, and J.-P. Ansermet, "Spin-dependent Peltier effect of perpendicular currents in multilayered nanowires," *Physical Review B*, vol. 73, p. 052410, Feb. 2006.

[46] K. Uchida, T. Ota, K. Harii, S. Takahashi, S. Maekawa, Y. Fujikawa, and E. Saitoh, "Spin-Seebeck effects in films," *Solid State Communications*, vol. 150, no. 11-12, pp. 524–528, 2010.

[47] K. Uchida, J. Xiao, H. Adachi, J. Ohe, S. Takahashi, J. Ieda, T. Ota, Y. Kajiwara, H. Umezawa, H. Kawai, G. E. W. Bauer, S. Maekawa, and E. Saitoh, "Spin Seebeck insulator.," *Nature materials*, vol. 9, pp. 894–7, Nov. 2010.

[48] D. Qu, S. Y. Huang, J. Hu, R. Wu, and C. L. Chien, "Intrinsic Spin Seebeck Effect in Au / YIG," *Physical Review Letters*, vol. 110, p. 067206, Feb. 2013.

[49] C. M. Jaworski, J. Yang, S. Mack, D. D. Awschalom, J. P. Heremans, and R. C. Myers, "Observation of the spin-Seebeck effect in a ferromagnetic semiconductor.," *Nature materials*, vol. 9, pp. 898–903, Nov. 2010.

[50] S. Y. Huang, W. G. Wang, S. F. Lee, J. Kwo, and C. L. Chien, "Intrinsic Spin-Dependent Thermal Transport," *Physical Review Letters*, vol. 107, p. 216604, Nov. 2011.

[51] G. E. W. Bauer, E. Saitoh, and B. J. van Wees, "Spin caloritronics.," *Nature materials*, vol. 11, pp. 391–9, May 2012.

[52] T. Kikkawa, K. Uchida, S. Daimon, Y. Shiomi, H. Adachi, Z. Qiu, D. Hou, X.-F. Jin, S. Maekawa, and E. Saitoh, "Separation of longitudinal spin Seebeck effect from anomalous Nernst effect: Determination of origin of transverse thermoelectric voltage in metal/insulator junctions," *Physical Review B*, vol. 88, p. 214403, Dec. 2013.

[53] M. Weiler, M. Althammer, F. D. Czeschka, H. Huebl, M. S. Wagner, M. Opel, I.-M. Imort, G. Reiss, A. Thomas, R. Gross, and S. T. B. Goennenwein, "Local Charge and Spin Currents in Magnetothermal Landscapes," *Physical Review Letters*, vol. 108, p. 106602, Mar. 2012.

[54] H. Schultheiss, J. E. Pearson, S. D. Bader, and a. Hoffmann, "Thermoelectric Detection of Spin Waves," *Physical Review Letters*, vol. 109, p. 237204, Dec. 2012.

[55] A. von Bieren, F. Brandl, D. Grundler, and J.-P. Ansermet, "Space- and time-resolved Seebeck and Nernst voltages in laser-heated permalloy/gold microstructures," *Applied Physics Letters*, vol. 102, no. 5, p. 52408, 2013.

[56] S. R. Boona, R. C. Myers, and J. P. Heremans, "Spin caloritronics," *Energy & Environmental Science*, vol. 7, no. 3, p. 885, 2014.

[57] E. H. Hall, "On a new Action of the Magnet on Electric Currents," *American Journal of Mathematics*, vol. 2, no. 3, pp. 287–292, 1879.

[58] E. H. Hall, "On the "Rotational Coefficient" in Nickel and Cobalt," *Proceedings of the Physical Society of London*, vol. 4, no. 1, pp. 325–342, 1880.

[59] A. W. Smith and R. W. Sears, "The Hall Effect in Permalloy," *Physical Review*, vol. 34, pp. 1466–1473, Dec. 1929.

[60] E. Pugh, "Hall Effect and the Magnetic Properties of Some Ferromagnetic Materials," *Physical Review*, vol. 36, no. 9, pp. 1503–1511, 1930.

[61] E. M. Pugh and T. W. Lippert, "Hall e.m.f. and intensity of magnetization," *Physical Review*, vol. 42, no. 5, pp. 709–713, 1932.

[62] R. Karplus and J. Luttinger, "Hall Effect in Ferromagnetics," *Physical Review*, vol. 95, pp. 1154–1160, Sept. 1954.

[63] T. Jungwirth, Q. Niu, and A. H. MacDonald, "Anomalous Hall Effect in

Ferromagnetic Semiconductors," *Physical Review Letters*, vol. 88, p. 207208, May 2002.

[64] M. Onoda and N. Nagaosa, "Topological Nature of Anomalous Hall Effect in Ferromagnets," *Journal of the Physical Society of Japan*, vol. 71, pp. 19–22, Jan. 2002.

[65] J. Smit, "The spontaneous hall effect in ferromagnetics I," *Physica*, vol. 21, pp. 877–887, Jan. 1955.

[66] J. Smit, "The spontaneous hall effect in ferromagnetics II," *Physica*, vol. 24, pp. 39–51, Jan. 1958.

[67] L. Berger, "Side-Jump Mechanism for the Hall Effect of Ferromagnets," *Physical Review B*, vol. 2, pp. 4559–4566, Dec. 1970.

[68] N. Nagaosa, J. Sinova, S. Onoda, A. H. MacDonald, and N. P. Ong, "Anomalous Hall effect," *Reviews of Modern Physics*, vol. 82, no. 2, pp. 1539–1592, 2010.

[69] T. J. Seebeck, "Ueber die magnetische Polarisation der Metalle und Erze durch Temperatur-Differenz," *Annalen der Physik*, vol. 82, no. 2, pp. 133–160, 1826.

[70] M. Mizuguchi, S. Ohata, K. I. Uchida, E. Saitoh, and K. Takanashi, "Anomalous Nernst effect in an L1 0-ordered epitaxial FePt thin film," *Applied Physics Express*, vol. 5, no. 9, p. 93002, 2012.

[71] J. Weischenberg, F. Freimuth, S. Blügel, and Y. Mokrousov, "Scattering-independent anomalous Nernst effect in ferromagnets," *Physical Review B*, vol. 87, p. 60406, Feb. 2013.

[72] G. Y. Guo, Q. Niu, and N. Nagaosa, "Anomalous Nernst and Hall effects in magnetized platinum and palladium," *Physical Review B*, vol. 89, p. 214406, June 2014.

[73] A. Slachter, F. L. Bakker, and B. J. van Wees, "Anomalous Nernst and anisotropic magnetoresistive heating in a lateral spin valve," *Physical Review B*, vol. 84, p. 020412, July 2011.

[74] F. Brandl and D. Grundler, "Fabrication and local laser heating of free-standing Ni80Fe20 bridges with Pt contacts displaying anisotropic mag-

netoresistance and anomalous Nernst effect," *Applied Physics Letters*, vol. 104, p. 172401, Apr. 2014.

[75] M. H. Kryder, E. C. Gage, T. W. Mcdaniel, W. A. Challener, R. E. Rottmayer, G. Ju, Y. T. Hsia, and M. F. Erden, "Heat assisted magnetic recording," *Proceedings of the IEEE*, vol. 96, no. 11, pp. 1810–1835, 2008.

[76] W. A. Challener and V. Amit, *Modern Aspects of Electrochemistry No. 44*, vol. 44 of *Modern Aspects of Electrochemistry*. New York, NY: Springer New York, 2009.

[77] P. G. Doyle and J. L. Snell, *Random Walks and Electric Networks*. The Carus mathematical monographs, Mathematical Association of America, 1984.

[78] J. Cserti, "Application of the lattice Green's function for calculating the resistance of an infinite networks of resistors," *American Journal of Physics*, vol. 896, no. 2000, pp. 896–906, 1999.

[79] S. Redner, *A Guide to First-Passage Processes*. Cambridge University Press, 2001.

[80] R. S. Hijjawi, J. H. Asad, A. J. Sakaji, M. Al-sabayleh, and J. M. Khalifeh, "Infinite simple 3D cubic lattice of identical resistors (two missing bonds)," *The European Physical Journal Applied Physics*, vol. 41, pp. 111–114, Feb. 2008.

[81] T. A. Maldonado, "Electro-optic modulators," *Handbook of optics*, vol. 2, pp. 11–13, 1995.

[82] T. Tachizaki, T. Muroya, O. Matsuda, Y. Sugawara, D. H. Hurley, and O. B. Wright, "Scanning ultrafast Sagnac interferometry for imaging two-dimensional surface wave propagation," *Review of Scientific Instruments*, vol. 77, no. 4, 2006.

[83] G. B. Airy, "On the Diffraction of an Object-glass with Circular Aperture," *Transactions of the Cambridge Philosophical Society*, vol. 5, p. 283, 1835.

[84] L. R. F.R.S., "XXXI. Investigations in optics, with special reference to the spectroscope," *Philosophical Magazine Series 5*, vol. 8, pp. 261–274, Oct. 1879.

[85] B. Zhang, J. Zerubia, and J.-C. Olivo-Marin, "Gaussian approximations of

fluorescence microscope point-spread function models," *Applied Optics*, vol. 46, p. 1819, Apr. 2007.

[86] I. Young, R. Zagers, and L. V. Vliet, "Depth-of-focus in microscopy," *Proceedings Of The . . .*, pp. 493–498, 1993.

[87] W. K. Hiebert, A. Stankiewicz, and M. R. Freeman, "Direct Observation of Magnetic Relaxation in a Small Permalloy Disk by Time-Resolved Scanning Kerr Microscopy," *Physical Review Letters*, vol. 79, pp. 1134–1137, Aug. 1997.

[88] H. Acremann, Y., Back, C. H., Buess, M., Portmann, O., Vaterlaus, A., Pescia, D., Melchior, "Imaging Precessional Motion of the Magnetization Vector," *Science*, vol. 290, pp. 492–495, Oct. 2000.

[89] C. Bayer, J. P. Park, H. Wang, M. Yan, C. E. Campbell, and P. a. Crowell, "Spin waves in an inhomogeneously magnetized stripe," *Physical Review B - Condensed Matter and Materials Physics*, vol. 69, no. 13, pp. 1–6, 2004.

[90] F. J. a. den Broeder, E. Janssen, W. Hoving, and W. B. Zeper, "Perpendicular magnetic anisotropy and coercivity of Co/Ni multilayers," *IEEE Transactions on Magnetics*, vol. 28, no. 5 pt 2, pp. 2760–2765, 1992.

[91] A. Barman, T. Kimura, Y. Otani, Y. Fukuma, K. Akahane, and S. Meguro, "Benchtop time-resolved magneto-optical Kerr magnetometer," *Review of Scientific Instruments*, vol. 79, no. 12, pp. 1–5, 2008.

[92] J. Olivier and R. Poirier, "Electronic structure of Al2O3 from electron energy loss spectroscopy," *Surface Science*, vol. 105, no. 1, pp. 347–356, 1981.

[93] V. P. Elena R. Dobrovinskaya, Leonid A. Lytvynov, *Sapphire: Material, Manufacturing, Applications*. Boston, MA: Springer US, 2009.

[94] V. Barnier, O. Heintz, D. E. Roberts, R. Oltra, and S. Costil, "XPS and SIMS study of aluminium native oxide modifications induced by Q-switched Nd : YAG laser treatment," *Surface and Interface Analysis*, vol. 38, no. 4, pp. 406–409, 2006.

[95] H.-w. Tseng, *Spin-torque effects in magnesium oxide-based magnetic tunnel junctions*. PhD thesis, Cornell University, Ithaca, NY, 2013.

[96] K. Vogt, P. Kohl, W. Carter, R. Bell, and L. Bottomley, "Characterization of

thin titanium oxide adhesion layers on gold: resistivity, morphology, and composition," *Surface Science*, vol. 301, no. 1-3, pp. 203–213, 1994.

[97] K. R. Williams, K. Gupta, and M. Wasilik, "Etch rates for micromachining processing - Part II," *Journal of Microelectromechanical Systems*, vol. 12, no. 6, pp. 761–778, 2003.

[98] J. R. Taylor, *An Introduction to Error Analysis: The Study of Uncertainties in Physical Measurements*. University Science Books, 2 sub ed., 1996.

[99] T. Suzuki, "Domain Wall Width Measurement in Cobalt Films by Lorentz Microscopy," *Journal of Applied Physics*, vol. 40, p. 1216, Nov. 1969.

[100] G. L. Eesley, "Generation of nonequilibrium electron and lattice temperatures in copper by picosecond laser pulses," *Physical Review B*, vol. 33, no. 4, pp. 2144–2151, 1986.

[101] C. Ho, M. Ackerman, K. Wu, S. Oh, and T. Havill, "Thermal conductivity of ten selected binary alloy systems," *Journal of Physical and Chemical Reference Data*, vol. 7, no. 3, p. 959, 1978.

[102] H. W. D. Bonnenberg, K.A. Hempel, "Thermomagnetic properties, thermal expansion coefficient, specific heat, Debye temperature, thermal conductivity," in *Magnetic Properties of Metals 3d, 4d and 5d Elements, Alloys and Compounds* (H. Wijn, ed.), ch. 1.2.1.2.10, Heidelberg: Springer-Verlag GmbH, 1986.

[103] E. A. Owen, E. L. Yates, and A. H. Sully, "An X-ray investigation of pure iron-nickel alloys. Part 5: the variation of thermal expansion with composition," *Proceedings of the Physical Society*, vol. 49, pp. 323–325, 2002.

[104] A. Q. Wu, Y. Kubota, T. Klemmer, T. Rausch, C. Peng, Y. Peng, D. Karns, X. Zhu, Y. Ding, E. K. C. Chang, Y. Zhao, H. Zhou, K. Gao, J.-U. Thiele, M. Seigler, G. Ju, and E. Gage, "HAMR Areal Density Demonstration of 1+ Tbpsi on Spinstand," *IEEE Transactions on Magnetics*, vol. 49, pp. 779–782, Feb. 2013.

[105] L. Landau and E. Lifshits, "on the Theory of the Dispersion of Magnetic Permeability in Ferromagnetic Bodies," *Phys. Zeitsch. der Sow.*, vol. 169, no. 14, pp. 14–22, 1935.

[106] M. Lakshmanan, "The fascinating world of the Landau-Lifshitz-Gilbert

equation: an overview.," *Philosophical transactions. Series A, Mathematical, physical, and engineering sciences*, vol. 369, no. 1939, pp. 1280–1300, 2011.

[107] J. a. Osborn, "Demagnetizing factors of the general ellipsoid," *Physical Review*, vol. 67, no. 11-12, pp. 351–357, 1945.

[108] J. Qin, Z. Huang, Y. Ge, Y. Hou, and J. Chu, "Tandem demodulation lock-in amplifier based on digital signal processor for dual-modulated spectroscopy," *Review of Scientific Instruments*, vol. 80, no. 3, pp. 1–8, 2009.

[109] N. Mecking, Y. S. Gui, and C. M. Hu, "Microwave photovoltage and photoresistance effects in ferromagnetic microstrips," *Physical Review B - Condensed Matter and Materials Physics*, vol. 76, p. 224430, Dec. 2007.

[110] A. Yamaguchi, K. Motoi, A. Hirohata, H. Miyajima, Y. Miyashita, and Y. Sanada, "Broadband ferromagnetic resonance of Ni81Fe19 wires using a rectifying effect," *Physical Review B*, vol. 78, p. 104401, Sept. 2008.

[111] J. Fassbender, "Magnetization Dynamics Investigated by Time-Resolved Kerr Effect Magnetometry," in *Spin Dynamics in Confined Magnetic Structures II* (B. Hillebrands and K. Ounadjela, eds.), pp. 59–92, 2003.

[112] M. J. Donahue and D. G. Porter, *OOMMF User's guide*. US Department of Commerce, Technology Administration, National Institute of Standards and Technology, 1999.

[113] C. Kittel, *Introduction to solid state physics*. Hoboken NJ: Wiley, 2005.

[114] J. C. Sankey, P. M. Braganca, a. G. F. Garcia, I. N. Krivorotov, R. a. Buhrman, and D. C. Ralph, "Spin-transfer-driven ferromagnetic resonance of individual nanomagnets," *Physical Review Letters*, vol. 96, no. 22, pp. 50–53, 2006.

[115] A. A. Tulapurkar, Y. Suzuki, A. Fukushima, H. Kubota, H. Maehara, K. Tsunekawa, D. D. Djayaprawira, N. Watanabe, and S. Yuasa, "Spin-torque diode effect in magnetic tunnel junctions.," *Nature*, vol. 438, no. 7066, pp. 339–342, 2005.

[116] M. Harder, Z. X. Cao, Y. S. Gui, X. L. Fan, and C. M. Hu, "Analysis of the line shape of electrically detected ferromagnetic resonance," *Physical Review B - Condensed Matter and Materials Physics*, vol. 84, pp. 1–12, 2011.

[117] T. McGuire and R. Potter, "Anisotropic magnetoresistance in ferromagnetic 3d alloys," *IEEE Transactions on Magnetics*, vol. 11, pp. 1018–1038, July 1975.

[118] J. Smit, "Magnetoresistance of ferromagnetic metals and alloys at low temperatures," *Physica*, vol. 17, no. 6, pp. 612–627, 1951.

[119] A. Fert, R. Asomoza, D. H. Sanchez, D. Spanjaard, and A. Friederich, "Magnetotransport properties of noble metals containing rare-earth impurities. I. Quadrupole scattering by rare-earth impurities in gold," *Physical Review B*, vol. 16, pp. 5040–5051, Dec. 1977.

[120] S. D. Brorson, J. G. Fujimoto, and E. P. Ippen, "Femtosecond electronic heat-transport dynamics in thin gold films," *Physical Review Letters*, vol. 59, no. 17, pp. 1962–1965, 1987.

[121] M. Battiato, K. Carva, and P. M. Oppeneer, "Theory of laser-induced ultrafast superdiffusive spin transport in layered heterostructures," *Physical Review B - Condensed Matter and Materials Physics*, vol. 86, no. 2, pp. 1–16, 2012.

[122] M. V. Belous, V. G. Permyakov, and V. I. Popov, "The electrical properties of thin permalloy films," *Soviet Physics Journal*, vol. 10, pp. 23–24, Mar. 1967.

[123] Y. Q. Zhang, N. Y. Sun, R. Shan, J. W. Zhang, S. M. Zhou, Z. Shi, and G. Y. Guo, "Anomalous Hall effect in epitaxial permalloy thin films," *Journal of Applied Physics*, vol. 114, p. 163714, Oct. 2013.